THE UNIVERSITY *of* EDINBURGH

The effect of pressure on metal-organic frameworks (MOFs)

Alexander J. Graham

A Thesis submitted in fulfilment of the requirements for the degree of Doctor of Philosophy to the School of Chemistry, University of Edinburgh

2013

Declaration

I declare that this Thesis has been written by me and that the work carried out is my own, or I have made a substantial contribution towards it except where specific reference is made to another. This work has not been submitted for another degree or professional qualification.

Alexander J. Graham

Abstract

A growing field of research has evolved around the design and synthesis of a variety of porous metal-organic framework (MOF) materials. Some of the most promising areas for which these materials are potentially useful candidates include gas-separation, heterogeneous catalysis, and gas-storage, and all of these applications involve placing the MOF under pressure. There is clearly a need to understand the structural response of MOFs to applied pressure. Nevertheless, hitherto there are very few published investigations dedicated to determining the behaviour of porous hybrid materials under pressure. Through the use of high-pressure single-crystal X-ray diffraction studies, a series of MOF materials have been studied.

Here we present the effect of pressure on a series of MOFs. In chapter 2, the effect of pressure on the prototypical MOF called MOF-5 was studied experimentally from ambient pressure to 3.2 GPa. Here, application of pressure was driven by the hydrostatic medium being forced into the pores of the MOF, which altered the mechanical properties of MOF-5, in particular, medium inclusion delayed the onset of amorphization. Complementary computational analysis was also performed to elucidate further the effect of medium inclusion on compressive behaviour.

Detailed structural data was also collected as a function of pressure on the MOF Cu-btc. Application of pressure caused solvent to be squeezed into the pores (like MOF-5) until a phase transition occurred, driven by the sudden compression and expansion of equatorial and axial Cu–O bonds.

High-pressure post-synthetic modification of a MOF is reported for the first time. On application of pressure of 0.2 GPa to the Cu-based MOF called STAM-1, a ligand exchange reaction takes place resulting in a change in pore size, shape, and hydrophilicity of the resulting pores. Here, we also demonstrate the ability to force hydrophilic molecules into hydrophobic pores using pressure, counteracting the hydrophobic effect.

A high-pressure combined experimental and computational study has been carried to probe the effect of pressure on 'breathing' mechanisms in a zeolitic imidazolate framework (or ZIF) called ZIF-8. The penetration of guest molecules and the accommodation of pressure are shown to be inextricably linked to the rotation of methylimidazolate groups in the structure.

Finally, the application of pressure to the MOF Sc_2BDC_3 and the nitro functionalized derivative $Sc_2(NO_2\text{-}BDC)_3$ was also studied. Here, the effect of chemical modification of the organic ligand, whilst maintaining framework topology, has been investigated as it pertains to compressibility. Directionality of compression is observed and this is rationalized with respect to the framework topology and medium inclusion/exclusion.

Publications

A. J. Graham, D. R. Allan, A. Muszkiewicz, C. A. Morrison, and S. A. Moggach, *Angwewandte Chemie, Int. Ed.*, 2011, **50(47)**, 11138-41

A. J. Graham, J-C Tan, D. R. Allan, and S. A. Moggach, *Chemical Communications*, 2012, **48(10)**, 1535-1537

S. A. Moggach, A. J. Graham, A. Muszkiewicz, C. A. Morrison, *International Journal of Nanotechnology*, 2012, **9(1/2)**, 18-22

Acknowledgements

I would not be writing this Thesis if it weren't for the patient help and belief of Dr Stephen Moggach. Thank you so much for everything you have done for me. I know it was a big gamble to take on a student who had never even done small molecule X-ray crystallography, based solely on his ability to quote Mitchell and Webb sketches under pressure (no pun intended). I realise that I am your first PhD student and we all know there's nothing quite like your first time. I hope you feel like I haven't embarrassed you too much even with inappropriate questions at national conferences.

I know it is the accepted thing to thank your second supervisor for his/her help regardless of actually how much they were involved. I am one of the lucky ones to not only have day to day interaction with my second supervisor but also to thoroughly enjoy it. Thank you to Prof Simon Parsons for all the help, advice and ruler prodding that you have dolled out. It's not often that you can cry with laughter during a group meeting and learn some rather eye watering facts about royalty at the same time. I also never knew cod could be so interesting!

Thank you to Dr Carole Morrison, for very patiently teaching me about computational chemistry and then very patiently re-teaching it to me when I forgot bits. I know how busy you are and I hope you realise how appreciative everyone is of your time and your sense of humour.

There are so many members of the chemistry department who I want to thank for having added to the enjoyment of my time at Edinburgh. The "Sex and the City" girls for listening to me rant and for sharing gossip. The Love/Arnold group for some great nights out and the Brechin's for general banter and beers. The greatest thanks must go to the guys from the office both past and present. Nick, Pete and Pat you were there from the start and I can't thank you enough for being friendly, welcoming, insulting and hilarious. Special thanks to Nick for being the Encyclopaedia Crystallographica even when you were on the home straight of your own Thesis writing. In no particular order, thanks also to Fraser, Paul, Chris, Gary, and Russell for help, chats and generally good times. To Jorge and Jack thank you for accepting me barging you're your office as someone you didn't know and making my last days of writing up so enjoyable. Lastly, to Scott and Andy, for making the last few months infinitely less stressful and tremendously enjoyable. I'll pure miss you guys.

To my parents, I don't think thank you covers it really. I know this isn't quite the doctor I had planned to be at school but you have backed me all the way. I know you don't quite understand what I do, but that has never stopped you encouraging me and asking me how it is going.

Claire, for a girlfriend to wait through the final year of an undergraduate degree when you are a graduate with a job is one thing. To then wait through three years of a PhD with all the associated stresses and strains is something else entirely. For all of your support, love, hugs and kisses, thank you. Hopefully you can now say you're marrying a doctor.

Contents

Chapter 1

Introduction

1.1 Porous materials

Most materials are porous, at least to some extent, and in fact it is quite difficult to obtain a truly non-porous material. Most solid materials contain cavities, channels or interstices and may be regarded as porous.[1] One can further categorize the pores themselves in order to classify these materials. Two ways to apply such restrictions are based on pore size and availability to an external fluid. Both of these attributes are discussed in detail throughout this Thesis.

Size-dependent classification has been outlined by IUPAC with the following nomenclature:

(i) pores with widths exceeding about 50 nm are called *macropores*;
(ii) pores of widths between 2 nm and 50 nm are called *mesopores*;
(iii) pores with widths not exceeding about 2 nm are called *micropores*.[2]

The availability of pores to an external fluid can be characterised using a number of different terms. Totally isolated pores, without any connections to the outside surface of the body of the material are termed *closed*. *Open* pores have continuous access to the external surface but can be *blind* pores (do not pass through to another side of the material) or *through* pores (open at two ends). These pore types can have varying shapes and sizes (as well as differing chemical natures) resulting in a huge library of differing porous materials including zeolites, zeotypes, porous carbons, metal organic frameworks (MOFs), and covalent organic frameworks (COFs).

Porous materials have attracted considerable attention in recent years primarily for applications in catalysis, gas storage and separation technologies.[3] All of these technologies exist because the pore structure of materials can have a large effect on the resulting physical properties including density, thermal and electrical conductivity,[4] magnetism,[5] and luminescence.[6] It is in part this link between pore structure and mechanical properties that has led to the investigation of the effect of physical stresses on porous materials, and we aim to describe some of the work carried out on microporous materials as a function of pressure to date.

1.2 Inorganic porous materials

1.2.1 Zeolites

The name zeolite, derived from the greek words ‘zeo’ and ‘lithos’, translates as ‘boiling stones’ and was discovered as a result of the work by the Swedish mineralogist Axel Fredrick Cronstedt.[7] He observed that a naturally occurring mineral, stilbite, visibly lost water upon heating. Zeolites are microporous, aluminosilicate minerals formed by the complete corner-sharing of SiO_4 and AlO_4 tetrahedra. These tetrahedra form complex porous arrangements of rings, channels and cages, with 201 unique zeolite framework topologies having been identified at time of writing.[8]

Due to the charges on the cations, Si^{4+} and the Al^{3+}, when aluminium replaces silicon, additional cations must also be present to maintain the overall charge balance with the chemical formula $(M^{n+})_{x/n}(AlO_2)_x(SiO_2)_{y.}Z(H_2O)$. The pores of zeolites as a consequence are occupied by cations, but usually also contain water molecules. In the majority of zeolites, variation of the Si/Al ratio can be achieved through the alteration of synthesis conditions or, less frequently, by post-synthetic dealumination treatment.[9] Typically, the cations and water are only loosely bound to the framework and are therefore mobile and can be exchanged without causing the collapse of the framework.

An example of a typical zeolite is zeolite A (e.g. Na-A, Figure 1). The composition of Na-A is $Na_{12}[Al_{12}\ Si_{12}O_{48}].\sim 27H_2O$ at ambient conditions. All forms of zeolite A, regardless of Si/Al ratio, cation nature or water content, are considered to be of the LTA structure type. This nomenclature is based on the categorization scheme of the International Zeolite Association, whereby each unique topology is given a three-letter code.

The structural properties of zeolites have made them a hugely valuable industrial resource in areas such as adsorption, ion exchange and catalysis.[10] In part due to their industrial applicability, the physical properties of zeolites have been studied with numerous examples of variable temperature behaviour published. However, studies as a function of pressure are much less numerous. Here we present some of the pressure-dependent studies that have been carried out and try to highlight some conserved high-pressure phenomena that emerge.

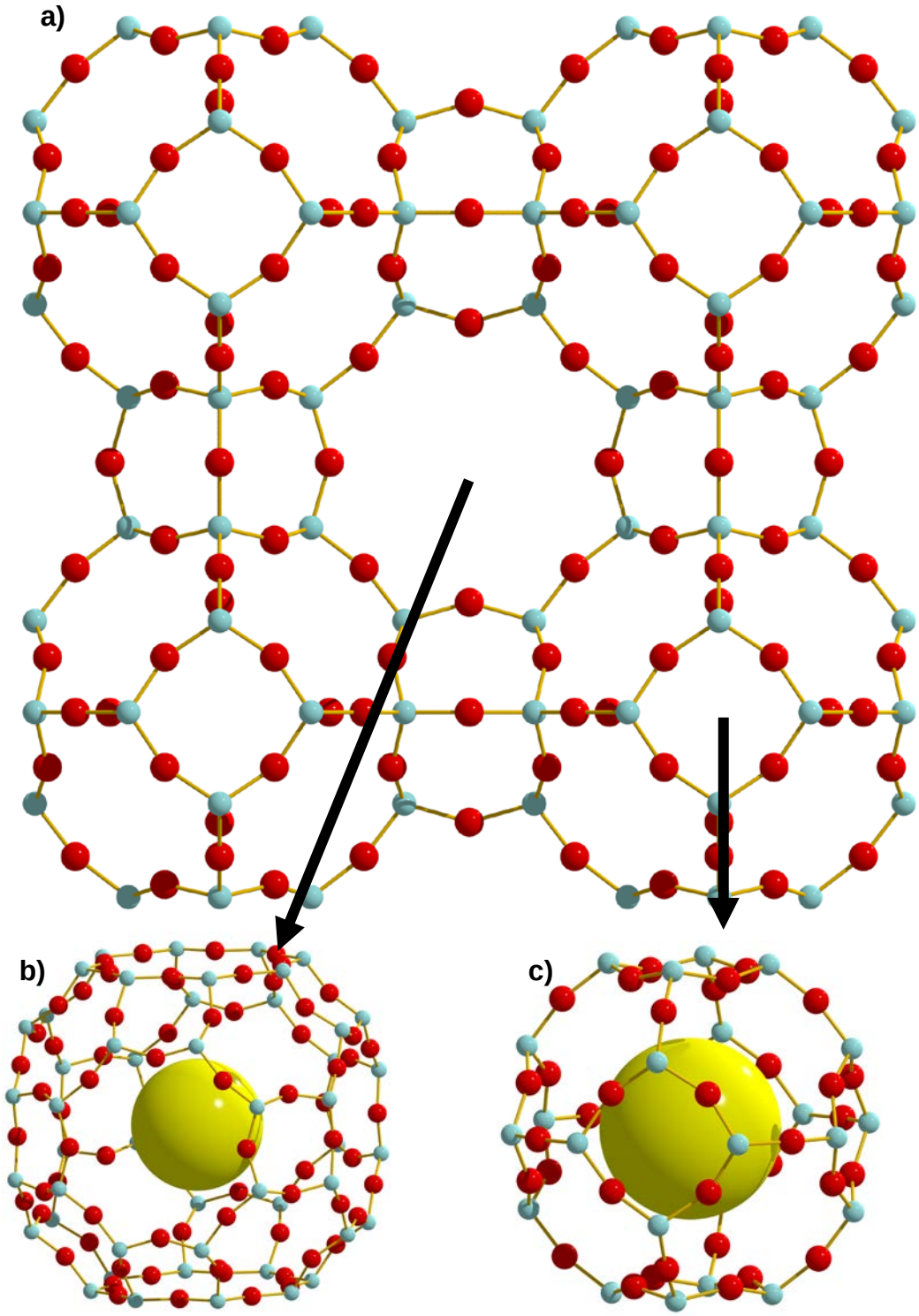

Figure 1. a) Structure of zeolite Na-A with water and cations removed for clarity. b) α-cage (supercage) with yellow sphere of 2.5 Å for illustration of porosity only. c) Smaller β-cage (sodalite cage) with yellow sphere of same size to highlight difference in cage volume. Key: Si/Al, light blue; O, red.

1.2.2 Aluminophosphates

In addition to aluminosilicates, another form of zeolites exist called aluminophosphates (AlPOs). These molecular sieves are generally built from $(AlO_4)^-$ and $(PO_4)^+$ tetrahedral subunits to form a neutral framework. Framework neutrality avoids the need for charge-balancing ions, offering up the possibility of pore evacuation for industrial applications. An example of this class of material is $AlPO_4$-5 (AFI) (Figure 2).[11]

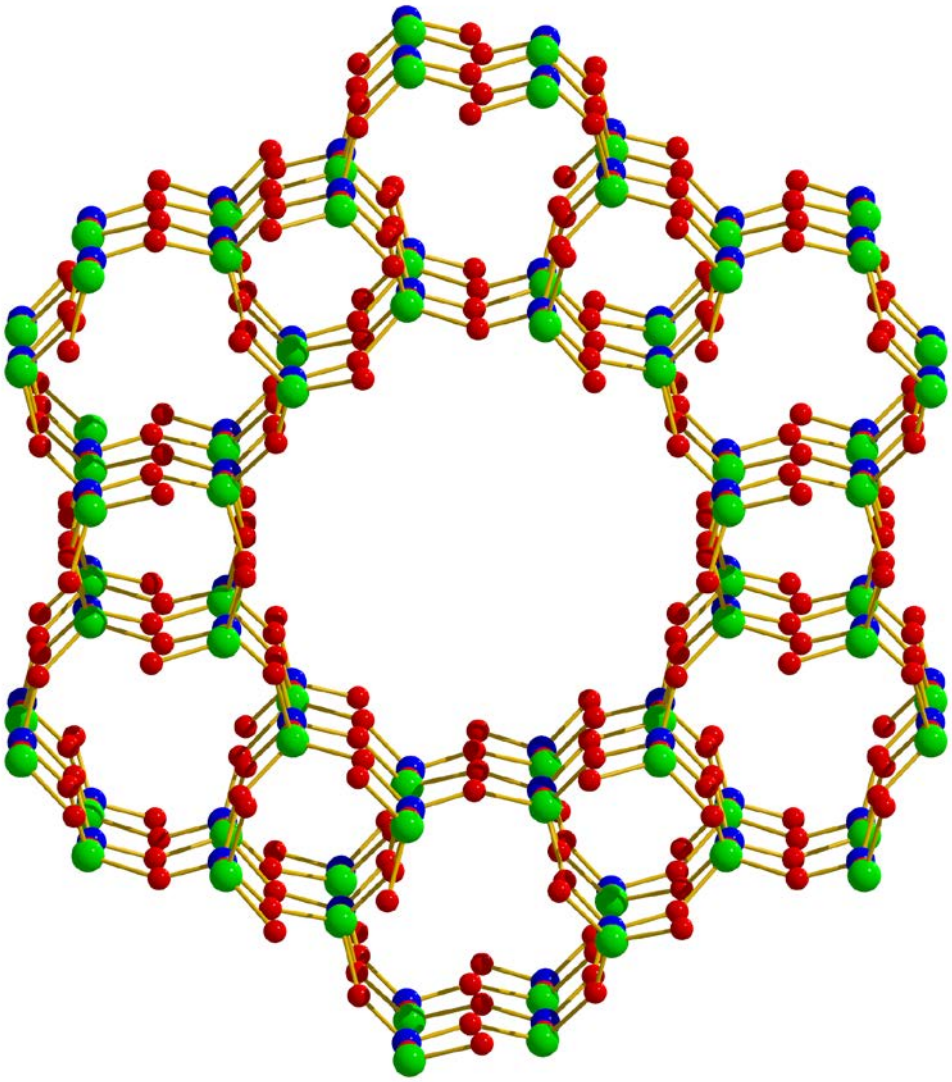

Figure 2. Structure of $AlPO_4$-5 zeolite (AFI) viewed along the crystallographic *a*-axis. Key: Al, green; P, blue; O, red. (Adapted from ref. 11)

This class of microporous materials has structural and chemical properties analogous to zeolites and has therefore been studied extensively in the search for improved performance levels in adsorption and catalysis processes.[12] $AlPO_4$-5 has even been used as a nanoscale container for the synthesis of the smallest single-walled carbon nanotubes.[13] Many $AlPO_4$ molecular sieves are isostructural with zeolites, while others possess unique framework topologies exclusive to aluminophosphates.

1.3 High-pressure phenomena in porous materials

1.3.1 The effect of guest inclusion at high pressure

One of the first *in situ* high-pressure X-ray diffraction studies of a zeolite was that of zeolite Na-A (Figure 1) by Hazen.[14] In this study, single crystals of Na-A (space group *Fm*3*c*, a = 24.55 Å) were separately loaded into a diamond anvil cell (DAC) (Figure 3) with different pressure transmitting liquids (or media) and the unit cell volumes were measured up to 4.0 GPa. The media chosen for this study were distilled water and a 4:1 mixture by volume of methanol and ethanol (MeOH:EtOH). These media are used to apply pressure evenly to the crystal as the diamond anvils apply pressure to the sample chamber.

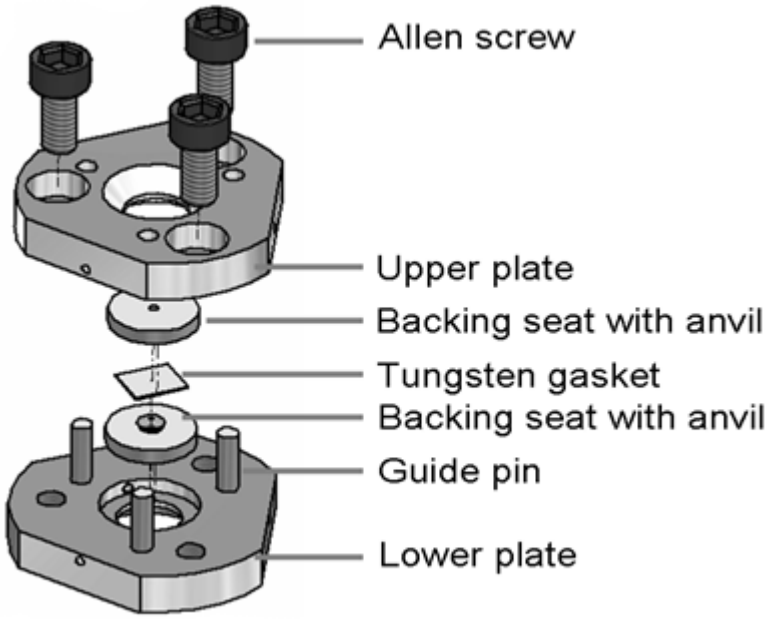

Figure 3. Schematic of a modified Merrill-Bassett DAC.

The effect of pressure on a material can be measured using the bulk modulus (*K)*, which characterises the variation of the volume of a solid with increasing pressure at constant temperature, and can be defined as:

$$K = -V \frac{\partial P}{\partial V} T$$

where V = volume, P = pressure and T = temperature. Some representative values include that of diamond (440 GPa), NaCl (25 GPa) and quartz (37 GPa). In contrast, discrete molecular solids typically have $K < 30$ GPa.[15]

In the study by Hazen, the value of K was dependant on the pressure-transmitting fluid used (Figure 4). In water, the K value remained constant and was determined to be 143 GPa up to 3.9 GPa of applied pressure. In MeOH:EtOH, four phases (phases I-IV) were observed as a result of pressure-induced transitions between each phase. After each discontinuity in the compressibility of the unit cell volume, the material became more compressible. The K values calculated for phases I-IV of zeolite Na-A in MeOH:EtOH were found to be 70, 60, 50 and 35 GPa, respectively. The transitions between each phase occurred above 1.9, 2.5 and 3.2 GPa, respectively. The compressibility of phase I in alcohols is twice as great as in water, with the compressibility increasing with successive pressure-induced phase transitions. The difference in compressibility was assigned to the different size of the medium molecules in MeOH:EtOH having different permeabilities within the framework. Ethanol is too large to enter the porous network while methanol can. In water alone, no discontinuities in the unit cell volume were observed on applying pressure to 4.0 GPa, indicating that continuous inclusion of water molecules into the framework occurs to 4.0 GPa. In alcohols, the difference in measured K values is attributed to the different diffusion rates of water to alcohols. An explanation proffered by the author for the discontinuities in the compressibility of the cell volume was that methanol absorbed into specific positions in the framework are squeezed out resulting in stepwise reductions in volume (Figure 4).

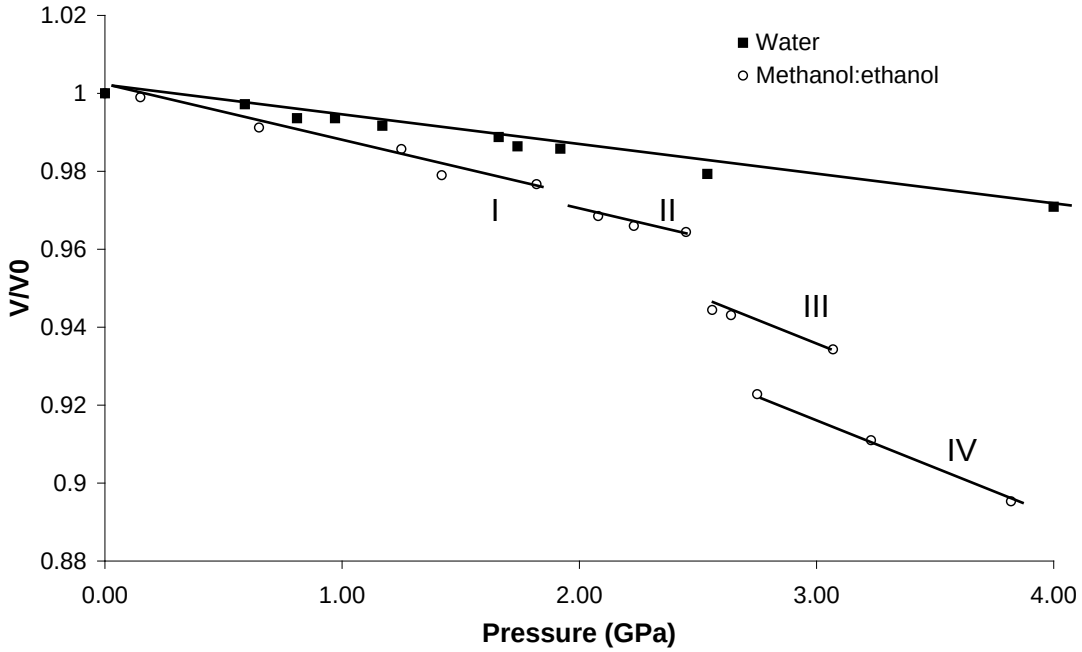

Figure 4. The change in normalised unit cell volume for zeolite Na-A samples in water and 4:1 methanol:ethanol. (Adapted from ref. 23)

This work was continued and expanded to include a further four pressure media: ethanol, methanol, glycerol, and an organofluorine compound, $C_8F_{16}O$ (FC-75).[16] The two large non-penetrating media, glycerol and FC-75, gave the largest compressibility (K = 22 GPa). Use of homogenous ethanol or methanol resulted in similar compression to that observed for the MeOH:EtOH mixture used previously, including the volume discontinuities outlined above. No explanation was offered for these postulated phase transitions. These studies and others show that inclusion/exclusion of guest molecules in otherwise identical frameworks can greatly affect the compressibility.[17, 18] They also highlight the differences between compression based on the molecular size of the molecules encompassing the liquid medium and therefore the rate at which they penetrate the pores.

A more recent study by Hriljac *et al*.,[19] repeated the MeOH:EtOH experiment using high-pressure synchrotron X-ray powder diffraction. The data from the two studies agree very well up to *ca.* 2.5 GPa, but then deviate very near to the point where the first phase transition was reported by Hazen et *et al*. In the powder study, a continuous decrease in volume was observed up to 6 GPa. At higher pressures, peak broadening and a reduction of intensity indicated the deterioration of long-range

crystalline order and the onset of amorphization. This variation in compressive behaviour has not been explained, but the authors suggested that the alternative behaviour may be due to differences in medium diffusion rates through the single-crystal samples of Hazen *et al*. as compared with the high-surface area powder samples used in this study.

The chemical nature of the pressure-transmitting medium can alter the high pressure behaviour of frameworks[20] and was seen to greatly affect the structural stability of $AlPO_4$-5 zeolite.[11] Powder samples of $AlPO_4$-5 were loaded in silicone oil and separately with a silicone oil/N_2 mixture. The inclusion of liquid N_2 in the silicone oil provided greater stability to compression compared with silicone oil on its own, delaying amorphization from 8.5 to 15.9 GPa. The authors postulate that nitrogen inserts into the channels of $AlPO_4$-5 as a penetrating medium and interacts with the framework, causing the inter-planar distance to increase and exerting a supporting effect against the structural collapse of the framework. Delayed pressure-induced amorphization was studied in silicalite-1-OH, in which the penetration of guest species resulted in crystallinity retention to 25 GPa as compared to 9.6 GPa for a non-penetrating medium.[21]

A study was carried out on the high-pressure structures of $AlPO_4$-5 and its pure-silica counterpart SSZ-24 ($Si_{24}O_{48}$) which have the same AFI framework topology.[22] Contrasting high-pressure compression behaviours were observed with a pore-penetrating pressure medium. $AlPO_4$-5 showed an initial expansion of the unit cell volume upon application of pressure in the penetrating medium (16:3:1 MeOH:EtOH:H_2O). This was followed by a continuous contraction with a derived bulk modulus of 50.5(7) GPa. In contrast, the isostructural pure-silica SSZ-24, showed no volume expansion in the same medium and was found to be more than twice as compressible with a bulk modulus of 21.7(3) GPa. An identical bulk modulus was obtained when SSZ-24 was compressed in the non-penetrating medium, silicone oil. The native hydrophobicity of SSZ-24 was thought to have altered the water distribution in the channels that run along the *c*-axis, therefore altering the guest inclusion on pressure application.

1.3.2 Initial framework content and its effect on high-pressure behaviour

The initial pore composition of the framework can affect the compressibility of the material.[23] An example of this phenomenon was observed when comparing the compressibility of zeolite Na-A and zeolite Zn-A ($Zn_6[Al_{12}Si_{12}O_{48}]$~$29H_2O$ (in which sodium was ion-exchanged for zinc).[19] This difference in framework composition brought about a dramatic change in behaviour. Zn-A showed a large (reversible) increase in unit cell volume under application of pressure to ~0.6 GPa in a 16:3:1 by volume mixture of methanol:ethanol:water (MEW), while zeolite Na-A only increased with pressure up to ~0.2 GPa. Interestingly, this only occurred with water-containing media, while pressure application in anhydrous MeOH:EtOH resulted in direct compression of the Zn-A framework. It was therefore suggested that both frameworks were undergoing a pressure-induced hydration. Unfortunately, the changes that occur that underlay this difference in behaviour have not been determined.

The hydration level of zeolite Na-A has also been shown to change the pressure at which the framework loses crystallographic order *i.e.* becomes amorphous. Dehydrated, hydrated and superhydrated samples of Na-A were treated up to 4.5 GPa and X-ray diffraction patterns were collected after 3 hours at ambient pressure.[24] Of these samples, only the superhydrated (above the saturated level of 27 H_2O molecules per unit cell) remained crystalline.

The process of superhydration and its effects on compressibility were explored in the zeolite, natrolite[25] (Figure 5). The framework is constructed from T_5O_{10} tetrahedral building blocks (where T is Al or Si), which form natrolite chains along the *c*-axis. High-pressure X-ray powder diffraction experiments were carried out on samples of natrolite up to 5 GPa in MEW and on a separate sample in silicone oil.

In MEW, there are two distinct regions in the plot of unit cell volume as a function of pressure. A discontinuity was observed between 0.8 and 1.5 GPa, with the pressure-induced incorporation of water causing an expansion of the unit cell volume. The pressure-induced swelling is caused by the expansion of the unit cell along the *a*- and *b*-axes whereas the *c*-axis showed a contraction during this volume expansion period. This 2-dimensional swelling suggests that the rotation of the

chains that along the *c*-axis and subsequent expansion of the channels in the (001) plane is responsible for the observed volume increase.

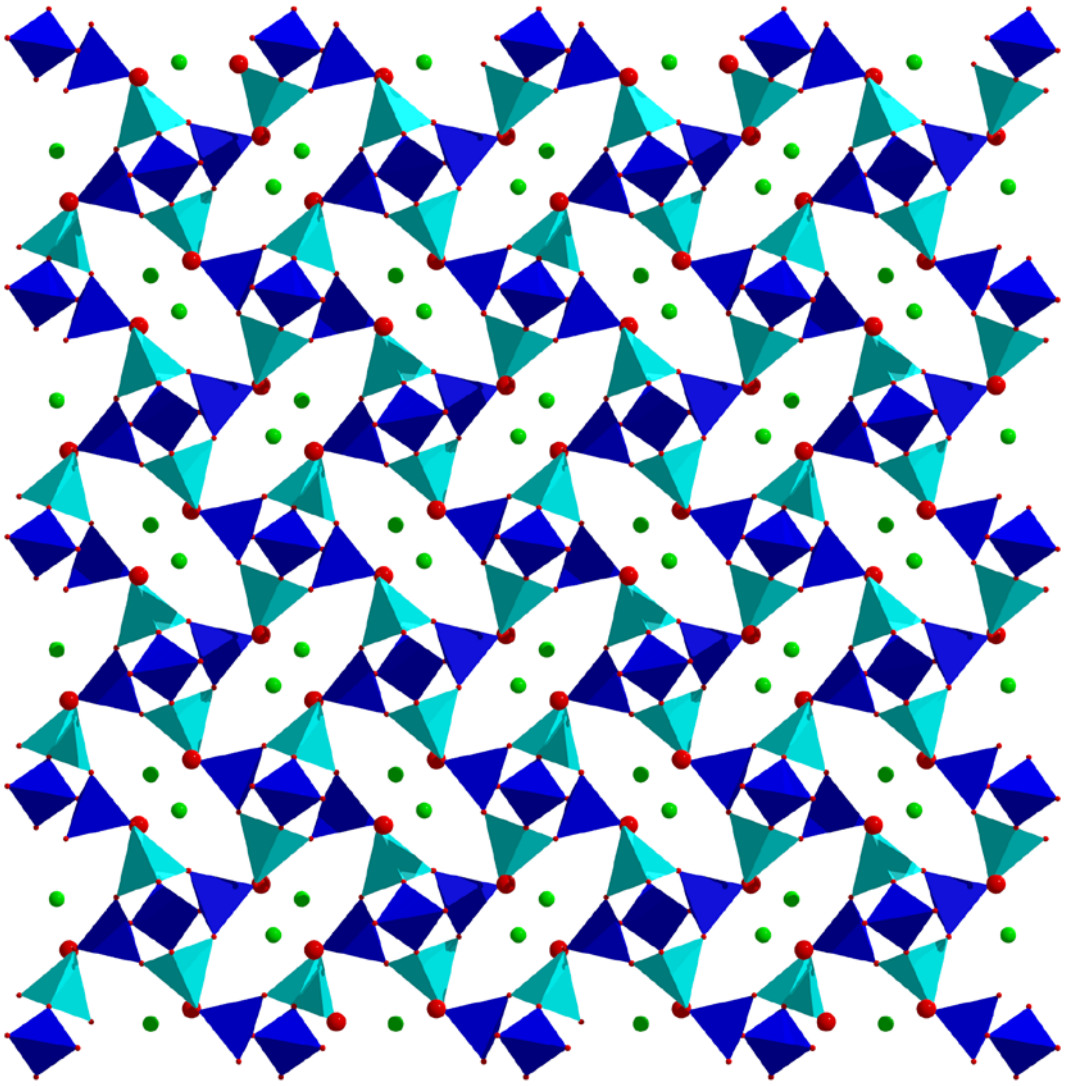

Figure 5. Polyhedral representation of natrolite $Na_{16}[Al_{16}Si_{24}O_{80}]16H_2O$ viewed along the crystallographic *c*-axis. The pore opening diameter is 2.5 Å. Key: SiO_4 tetrahedra, royal blue; AlO_4, turquoise tetrahedra; O, red; Na, green. (Adapted from ref. 37)

After the volume expansion at 1.5 GPa, an additional fully occupied water site was observed along the channel, resulting in a superhydration of natrolite with an increase in water content from 16 to 32 molecules per unit cell (Figure 6). The experiment was repeated using silicone oil as a hydrostatic medium, and showed no such increase in unit cell volume as the medium was too large to penetrate the pore volume. As a consequence, direct compression of the native natrolite occured.

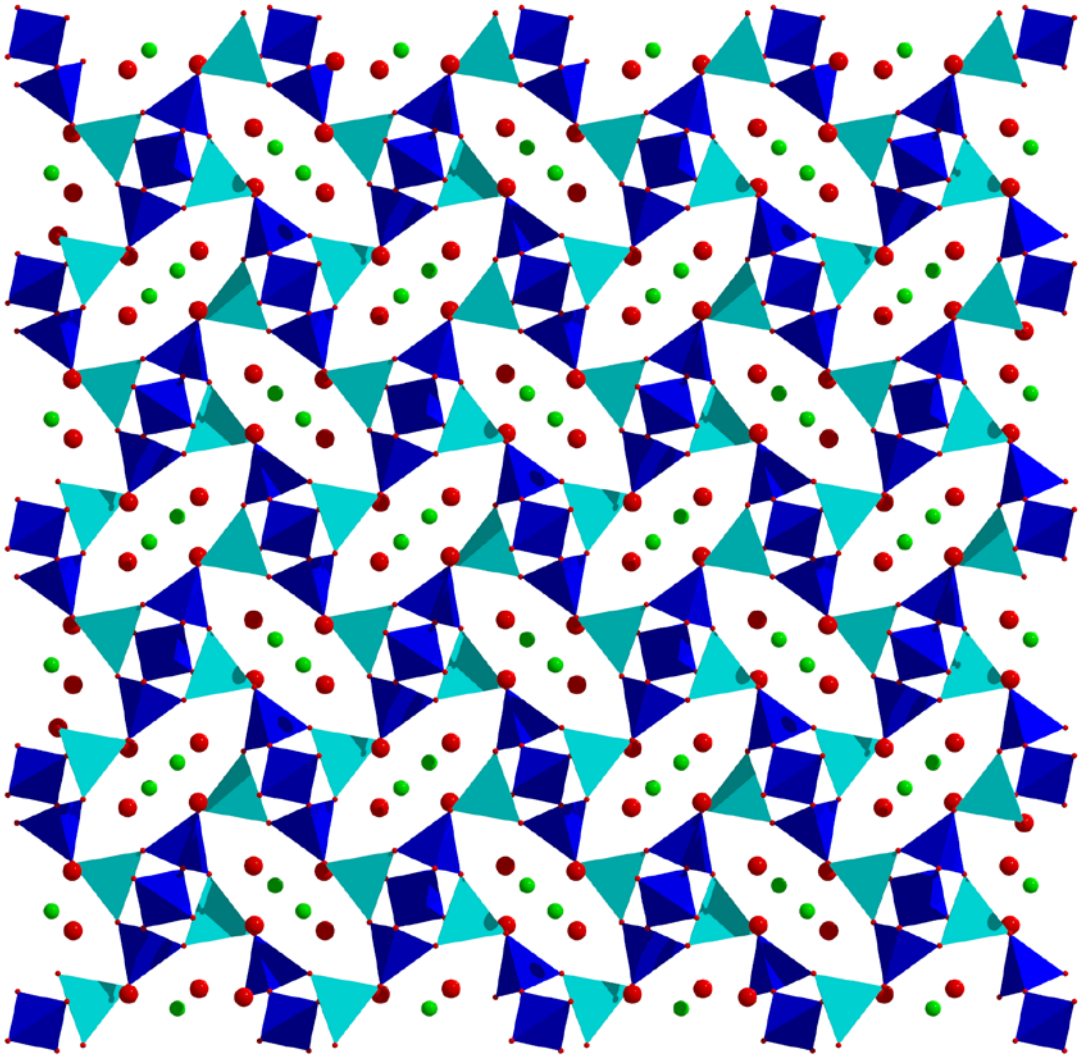

Figure 6. Polyhedral representations of superhydrated natrolite $Na_{16}[Al_{16}Si_{24}O_{80}]32H_2O$ at 1.5 GPa viewed along crystallographic *c*-axis. Key: as for Fig 3. (Adapted from ref. 37)

The transition at 1.5 GPa to superhydrated natrolite not only doubled the water content but also changed the compressibility of the material. The measured bulk modulus of the superhydrated natrolite (K = 49(1) GPa) is slightly smaller than that of the native natrolite (K = 53(1) GPa), illustrating that the superhydrated form is more compressible.

Following on from this work, high pressure was used to investigate an intermediate hydration form of natrolite, namely paranatrolite $Na_{16}[Al_{16}Si_{24}O_{80}]\cdot 24H_2O$,[26] the existence of which had, until this study, been postulated but disputed.[27] This intermediate phase was identified as an ordered form

of paranatrolite, which is stable near 1.0 GPa. Interestingly, despite the elevated pressure at which paranatrolite was observed, the density was found to be 2.21 g/cm³ at 0.99 GPa, smaller than that measured at 0.84 GPa (2.26 g/cm³). This suggests that application of pressure drives a rearrangement of the extra framework water molecules and sodium cations in the intermediate phase, which then exhibits less efficient packing of the water molecules inside the natrolite channel. The pressure-induced migration of zeolitic water was also observed in laumontite ($Ca_4Al_8Si_{16}O_{48}.nH_2O$).[28] Above 3 GPa, the reordering of the water molecules and/or Ca cations inside the channels was used to explain a tripling of the *b*-axis.

As well as being able to alter the water content of zeolite frameworks, high pressure can also bring about large changes in the framework structure. Such structural changes have been observed in the flexible zeolite RHO. In a study by Lee *et al.*, Na-, Cs-, Cd-, and Li-forms of zeolite RHO were loaded into a DAC with MEW as the pressure transmission medium.[29] Pressure-induced phase transitions were observed for all forms of the framework, from large-volume centric to small-volume acentric structures. This transition appears analogous to that driven by dehydration on heating,[30] and involves the elliptical distortion of the double 8-ring (D8R) opening in the structure (Figure 7).

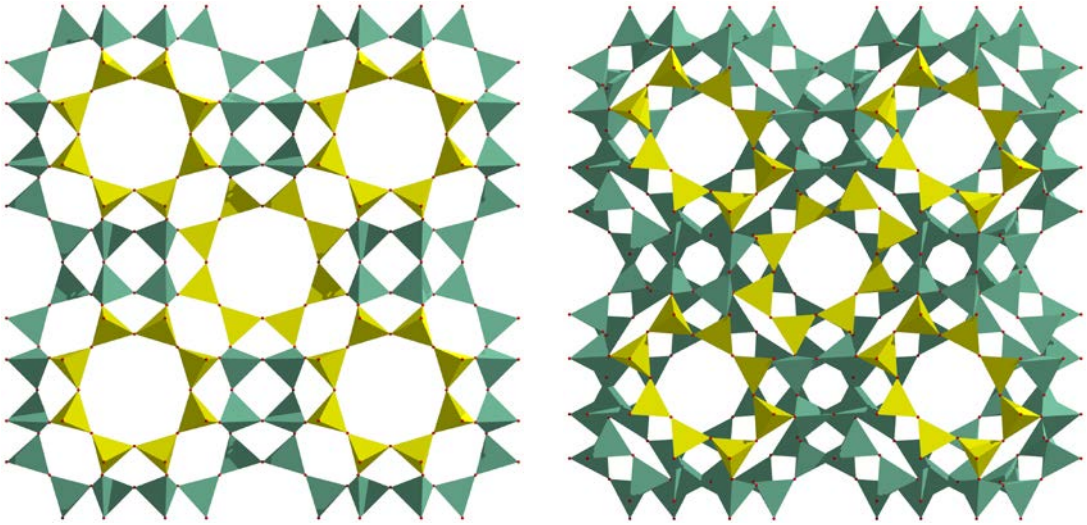

Figure 7. Polyhedral representation of zeolite RHO in the ambient-pressure and temperature centric C-form (*Im*(-3)*m*), left, and high-pressure acentric A-form (*I*(-4)3*m*), right. Yellow tetrahedra illustrate the D8R pore openings, which become elliptical upon the phase transition.

Similarly to the examples above, the initial extra-framework content was seen to affect the compressibility of the material, though the transition from centric to acentric forms occurred irrespective of the initial extra-framework cation distribution. The initial cation composition dictated the compressibility and also the pressure at which the material underwent the high-pressure transition which in all cases occurred between 0.2 and 0.5 GPa. It was seen that Li-RHO was more compressible at high-pressure than either NaCs- or Cd-RHO. The authors proposed that the initial cation distribution around the D8R building unit in NaCs- and Cd-RHO made these frameworks more resistant to collapse. Under ambient conditions the cations in Li-RHO are distributed at the single 6-ring site, which does not afford the same robustness. After undergoing the transition, which is associated with some form of desorption or dehydration, the high-pressure acentric form is consistently more compressible than the centric form of the framework.

The transition from the ambient pressure and temperature centric (C-form) to high-pressure acentric (A-form) is fully reversible on decreasing pressure. The rate at which the reverse transition took place is thought to be diffusion controlled and directly related to the degree of distortion of the pore-opening of the high-pressure phase. Li-RHO returns to the centric structure over a period of weeks whereas NaCs-RHO and Cd-RHO show signs of back-transformation immediately after return to ambient pressure.

1.3.3 Pressure-induced amorphization in inorganic materials

On applying high-hydrostatic (or non-hydrostatic) pressures to a microporous material, the strain on the framework can cause the complete loss of crystallinity and the onset of an amorphous phase.[31] An example of pressure-induced amorphization studied by X-ray diffraction is that of zeolite Li-A and Na-A.[32] Energy dispersive X-ray diffraction (EDXRD) was used to probe the onset of amorphization from ambient pressure to 4.0 GPa. Interestingly, this is the same pressure range used in the studies carried out by Hazen *et al*. (*vide supra*), in which no amorphization was reported for Na-A (Li-A was not studied in this work). In this study the mineral pyrophyllite ($Al_2Si_4O_{10}(OH)_2$) was used as a solid pressure-transmitting medium and boron nitride (BN) was used as the gasket material. On increasing pressure, a gradual

reduction in diffraction intensity was observed for both Li-A and Na-A, with the most prominent decrease occurring up to approximately 2.2 GPa. On increasing pressure to 4.0 GPa, a complete loss of long-range crystalline order was observed, as shown in Figure 8.

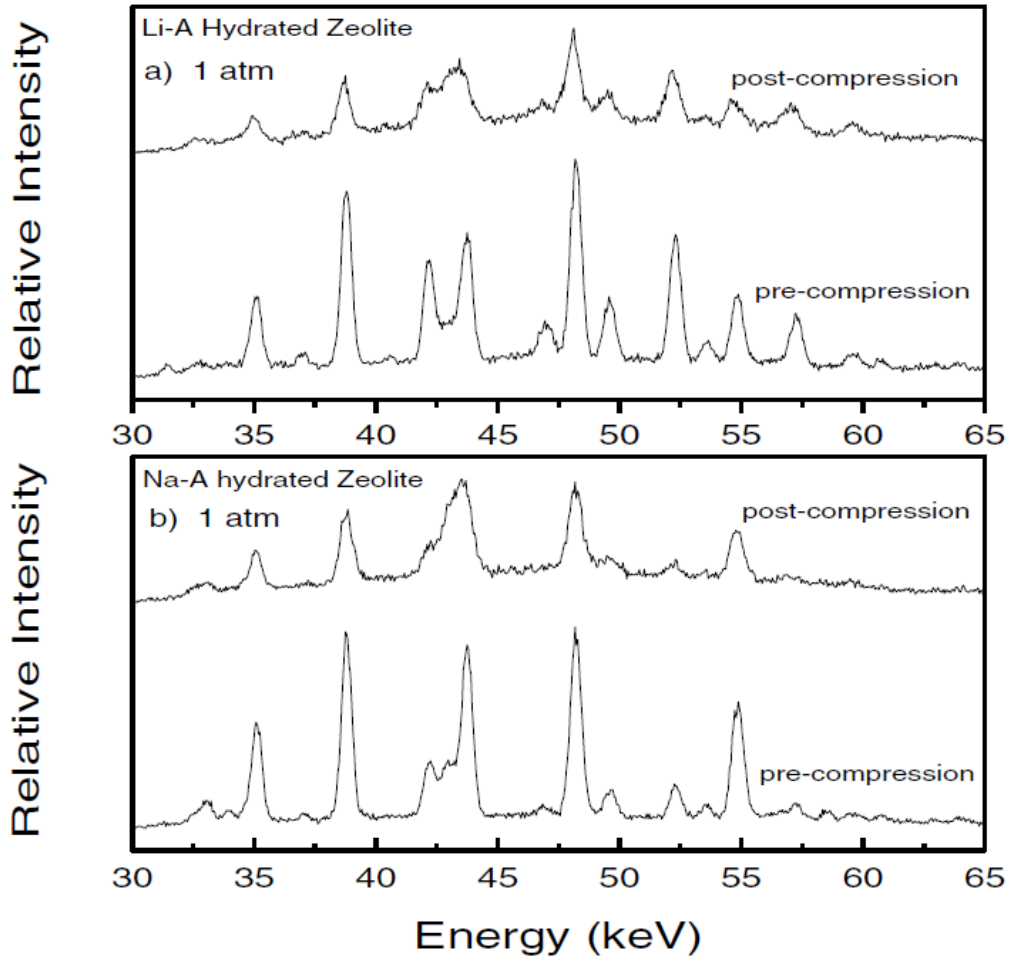

Figure 8. (a) Powder diffraction patterns for Li-A zeolite at 1 atm for pre- and post-compression to 4.1 GPa. (b) Diffraction patterns for Na-A zeolite at 1 atm for pre- and post-compression to 4.1 GPa. Intensities are plotted on the same scale as the 1 atm patterns. (Taken from ref. 46)

On decreasing pressure, the transition from a crystalline to amorphous phase was found to be reversible for both Li-A and Na-A (Figure 8), behaviour often referred to as structural memory. Although a reduction in peak intensity was observed on releasing the pressure, this was attributed to the possibility of X-ray absorption by the extruded BN gaskets. Under quasi-hydrostatic pressure application, it can be expected that the crystal would degrade to an amorphous material, as the

crystal is effectively being subjected to mechanical grinding. In this case, however, the reappearance of a strong diffraction signal upon decompression would preclude such degradation. Peak broadening and intensity reduction are characteristic of the onset of crystalline amorphization, with short-range order often retained. Pair distribution function (PDF) analysis can be used to analyse this short range order and this has been carried out on the zeolite Na-A by Readman *et al.*[33] PDF analysis uses both the Bragg and diffuse scattering in a diffraction pattern to allow examination of semi-crystalline materials and microporous materials where there is a lack of long range order beyond ~10 nm.

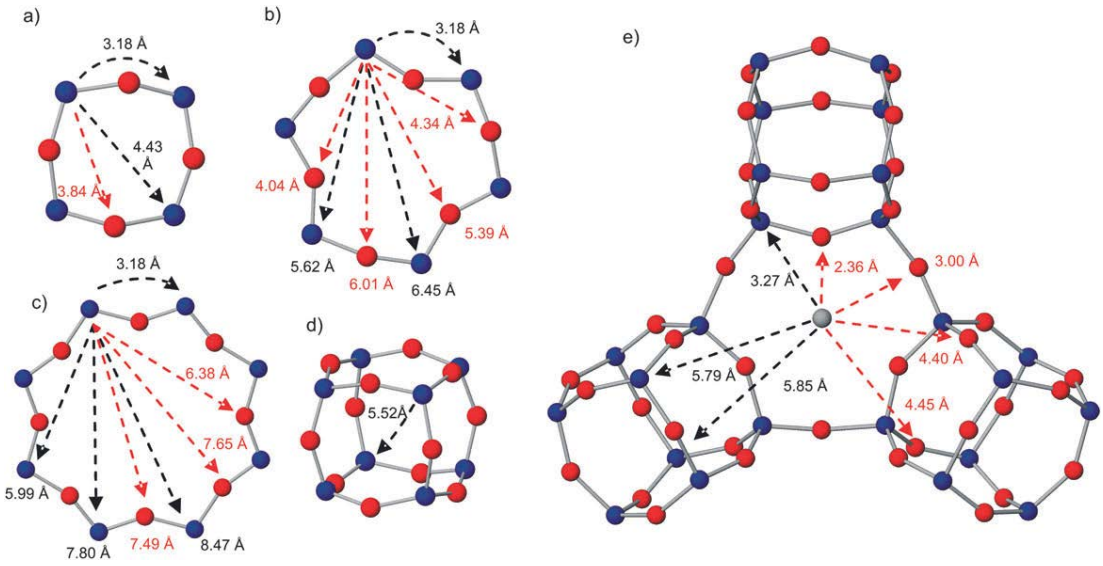

Figure 9. The main structural units of the LTA framework with interatomic distances derived from PDF analysis shown: (a) 4-ring, (b) 6-ring, (c) 8-ring and (d) double 4-ring. In (e) distances are shown from Na positioned at site I to both T and O atoms. Key: Si/Al, blue; O, red. (Taken from ref. 33)

PDF analysis gives information about the distances between pairs of atoms, allowing evolutions in local structure as a function of pressure to be traced. In this study, PDF analysis showed that the basic SiO_4/AlO_4 tetrahedral units are retained during amorphization, and the peaks associated with the Na-O vectors are also unchanged, which is consistent with conservation of the environment surrounding the sodium atoms. However, large changes were observed for peaks associated with the distortion of the double 4-ring (D4R) four-membered ring system (Figure 9d) and the relaxation of the surrounding framework. This D4R breakdown involved the distortion of the smallest inorganic section of the framework known as a secondary

building unit, (SBU) (Figure 9). Distortion of the D4R had a knock-on effect for the rest of the framework and caused the deformation of central sodalite cages.

The process by which the porous zeolite faujasite 13X accommodates pressure up to and including amorphization has also been thoroughly investigated using both X-ray diffraction and Raman spectroscopy.[34] Faujasite has on one of the largest channel diameters (7.4 Å) of all natural zeolites. Due to the large aperture size, and the associated expectation of guest inclusion, the Raman spectroscopy experiment was carried out in the absence of hydrostatic medium in order to avoid interactions between the sample and the medium itself. The X-ray diffraction experiments were carried out in the absence of medium and also with silicone oil as a non-penetrating hydrostatic medium.

These studies revealed that there were three phases of compression (Regions I to III) and crucially there was evidence to explain this compression and the onset of the amorphous phase. Region I (between ambient and 2 GPa) was characterized by linear compression with a bulk modulus K = 36.3(1.2) GPa. This value is in good agreement with the isostructural faujasite-type, siliceous zeolite Y (sil-FAU) which has a bulk modulus of 38(2) GPa.[18] Interestingly, sil-FAU differs in that it does not contain aluminium or extra-framework species (Na^+, H_2O). This shows that in the initial high-pressure phase, the Si/Al ratio and the presence of extra-framework species do not play a role in compression.

From 2 to ~3 GPa (Region II), there was an increase in bulk modulus (K = 56(6) GPa) and a corresponding decrease in pressure dependence of the Raman modes. When using silicone oil as a PTM, the Region II phase was also accompanied by a reduction in diffraction intensity signalling the onset of an amorphous phase. The authors postulated that the increase in bulk modulus was caused by the microstructure of faujasite, which gives rise to local depressurization effects due to the coexistence of low-density amorphous (LDA), high-density amorphous (HDA) and crystalline faujasite phases; a phenomenon also observed in zeolite-A.[31, 35]

Region III, above 3.5 GPa, showed a return to compressibility similar to that of Region I. In this pressure range the Raman signal associated with framework ring structures weaken, indicating that such structural features undergo significant

distortion. Most of the partially-amorphized faujasite or locally ordered LDA phase was expected to have transformed to a more distorted HDA phase. Complete amorphization was observed close to 12 GPa.

1.4 Metal Organic Frameworks

Over the last two decades or so the class of porous coordination polymers known collectively as metal organic frameworks has emerged as a worldwide area of interest in a diverse range of research disciplines. As the name suggest, MOFs are a classified by their robust bonding of metal nodes with organic linkers to produce a myriad of crystalline porous frameworks that have been designed for a number of different applications, including molecular sensing,[36] gas separation and storage,[37] drug transport and as high surface area catalysts.[38]

Whatever the intended application, the primary factor that makes MOFs so appealing, is the ability to tune their pore size, shape and therefore selectivity especially towards gas uptake. To date, there is a large body of literature where these properties have been altered via 'chemical' means, modifying the rigid organic unit, metal linker or both, in order to investigate the structure of the resulting frameworks. In particular, structural studies using single-crystal and powder X-ray and neutron diffraction have helped determine the binding sites within MOFs where the uptake of gases and other guest molecules takes place.[39] More recently, the ability to tune the pore size and shape of MOFs including guest content has been achieved by applying high pressures (410 000 atmospheres). Studies have utilized a number of techniques to probe the mechanical properties of MOFs including nanoindentation, computation and high-pressure crystallographic techniques.[40] At the commencement of this PhD, only two porous framework materials have been investigated at high pressure, namely ZIF-8 ($Zn(MIm)_2$, MIm = 2-methylimidazole)[41] and Cu-btc ($[Cu_3(TMA)_2(H_2O)_3]n$, TMA = benzene-1,3,5-tricarboxylate).[42] In both ZIF-8 and Cu-btc, some of the pressure-transmitting medium entered the pores, resulting in guest-dependent pressure behaviour for Cu-btc, while guest induced-pore size and content modification (including a guest-driven phase transition) was observed for ZIF-8.

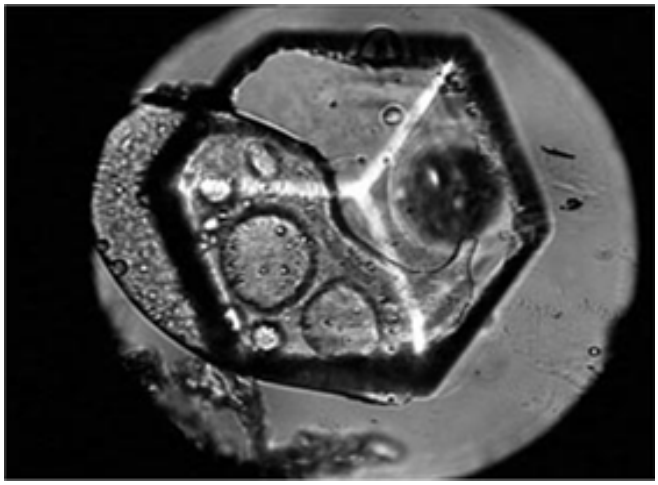

Figure 10. Optical image of a single crystal of ZIF-8 at ambient pressure in a DAC.

Zeolitic imidazolate frameworks form a family bearing topological resemblance to silicates and zeolites, but incorporating organic fragments which promote cavity formation. In a recent high-pressure single-crystal diffraction study, it was shown that application of GPa pressures could be used to modify both the pore size and shape of ZIF-8, which has a large accessible central nanopore (> 2000 Å^3). For this pressure study a single-crystal of ZIF-8 was surrounded with a 4:1 by volume mixture of methanol:ethanol as a liquid hydrostatic medium inside a diamond anvil cell (Figure 10).

Ambient pressure ZIF-8 has shown unusual N_2 adsorption behaviour, by having a step in its isotherm (Figure 11). This indicates that at a certain partial pressure of N_2 the framework expands enabling it to adsorb more N_2. This phenomenon, referred to as 'breathing' cause frameworks (otherwise known as 'hosts'), to reversibly modulate their pore size and shape according to which molecules (or 'guests') are adsorbed into the pores. Recent modelling results have demonstrated that the high pressure ZIF-8-HP phase can be used to model the breathing mode responsible for the increased uptake of gas (Figures 11 & 12),[43] a result confirmed by an *in situ* X-ray powder diffraction study of ZIF-8 collected at partial pressure in N_2.[44]

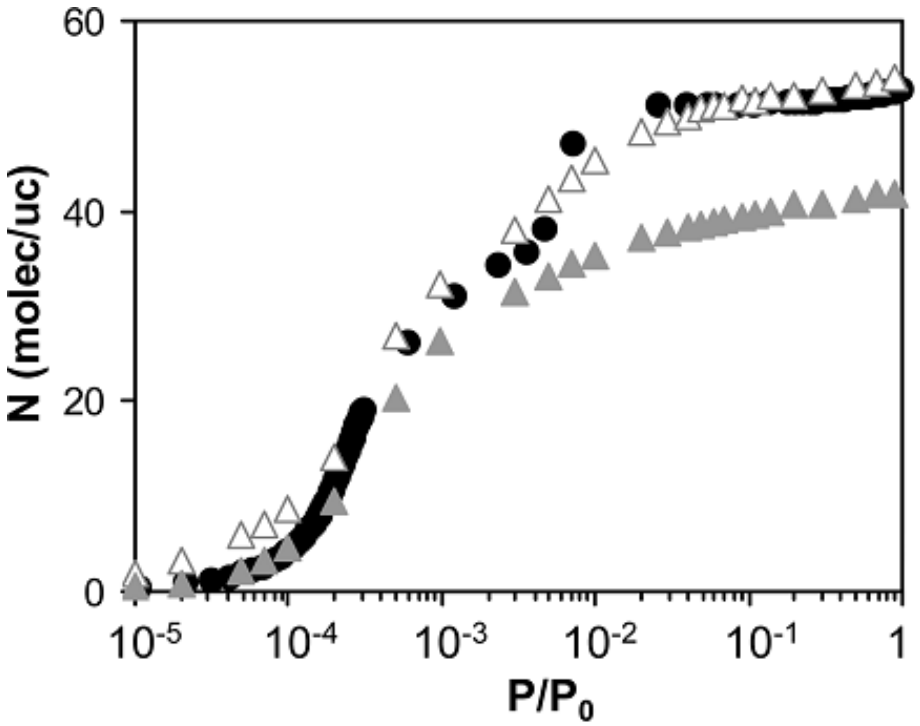

Figure 11. Semilog plot of N_2 adsorption on ZIF-8 at 77 K: experimental, circles; and simulated data on ambient pressure structure, ZIF-8, closed triangles and high-pressure structure, ZIF-8 HP, open triangles. (Taken from reference 43)

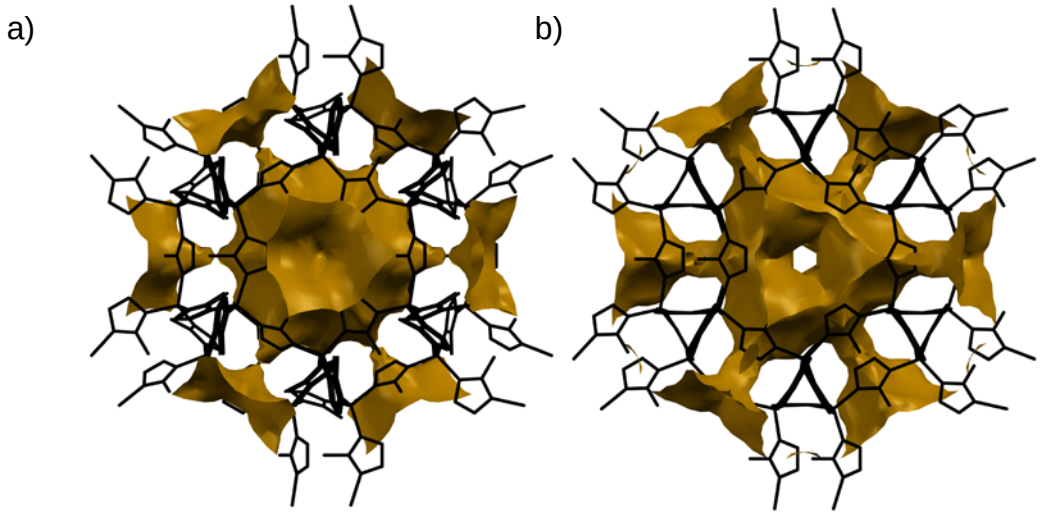

Figure 12. Void analysis, as carried out in the program MERCURY, of a) ZIF-8 at ambient pressure and b) ZIF-8-II at 1.47 GPa as viewed along the [111] direction. (image adapted from ref. 41)

Breathing mechanisms have been known for numerous metal organic framework materials, the most common example being that of the MIL (Material Institute Lavoisier) class of material. MILs are composed of Fe, Cr, Al, V, Zn or Ga

metal ions linked with a variety of substituted carboxylates, including terepthalic (BDC) and trimesic acid (BTC).[45] On adsorption of guest species, these materials have been shown to undergo colossal changes in volume (up to 40% or more) upon guest inclusion (Figure 13).[46] ZIFs, and in particular ZIF-8 is usually considered to be a rather rigid framework, previously thought to be incapable of undergoing the transition observed at 1.47 GPa and at partial pressure in N_2 gas.

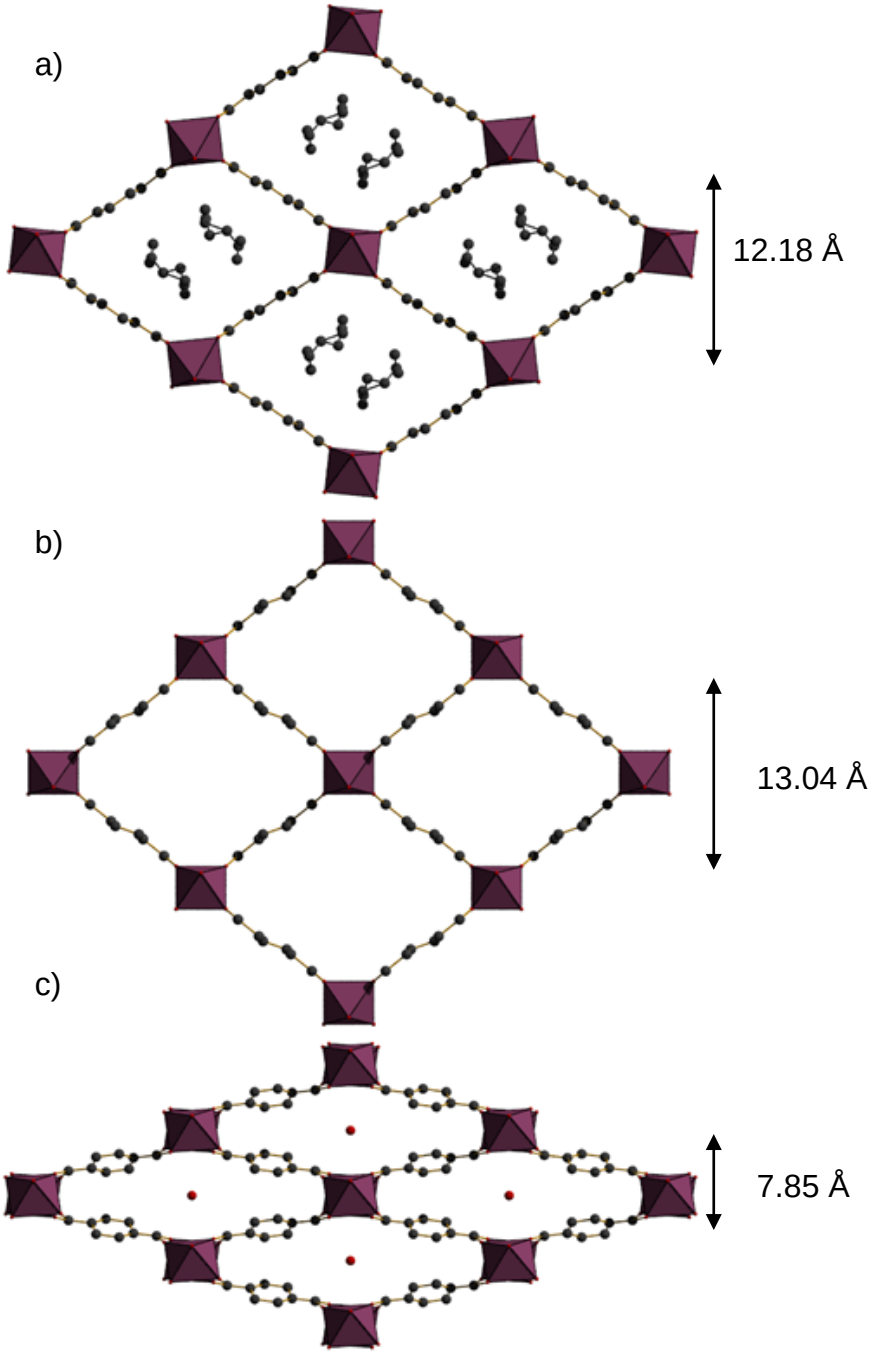

Figure 13. View of the pore systems of a) MIL-53 as synthesised, b) MIL-53 high temperature and c) MIL-53 low temperature. (Adapted from ref. 46)

In the high-pressure powder diffraction study on Cu-btc, high-pressure experiments were carried out in the presence of methanol-ethanol-water (MEW, 16 : 3 : 1 by volume), isopropyl alcohol and Flourinert (FC-70, perfluorotri-N-pentylamine) as the hydrostatic liquids. In this study, Chapman *et al*. illustrated that with MEW and IPA, the Cu-btc framework exhibits a clear transition between two distinct regions of near linear compressibility (Figure 13). The change in compressibility here was ascribed to a change from a pore filling, to a pore emptying transition, where the transition pressure was affected by the size of the hydrostatic liquid entering the pores (molecules in MEW are smaller than IPA, and therefore delaying the onset of the transition from ~0.8 to ~ 2.2 GPa). When a non-penetrating hydrostatic liquid was used (Fluorinert), direct compression of the framework occurred. The pore filling mechanism observed on initially applying pressure made Cu-btc much more resilient to compression; however, no detailed structural data was reported.

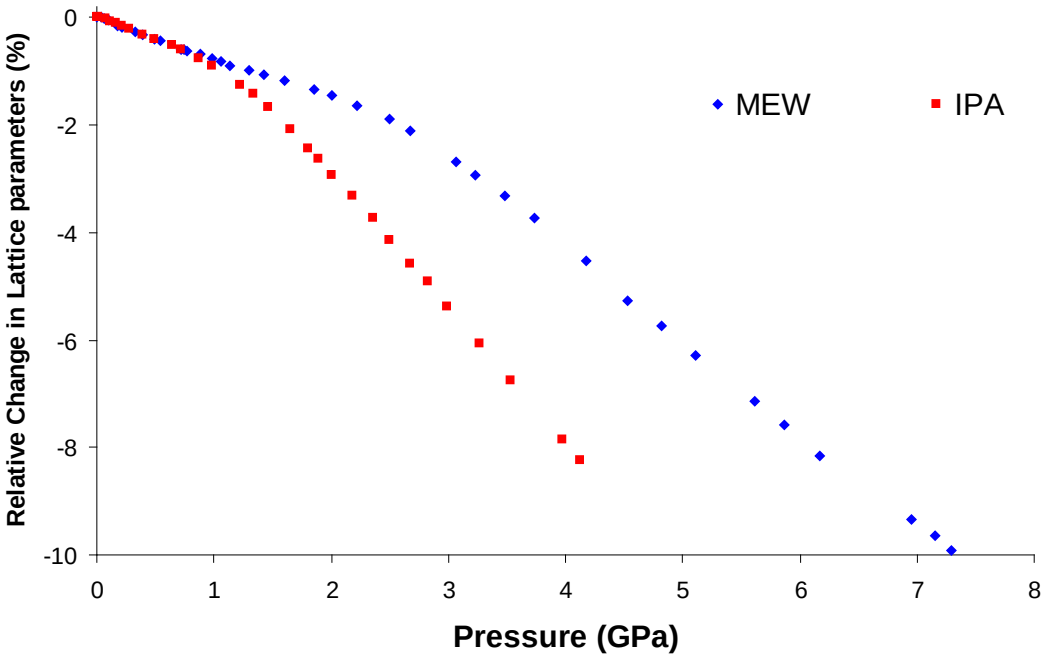

Figure 14. Relative change in lattice parameters for Cu-btc compressed in MEW and isopropyl alcohol (IPA), showing two linear regions of compression (adapted from ref. 42).

1.5 Summary of high-pressure behaviour

To date, a number of important phenomena have been discovered in porous inorganic compounds, including MOFs;

- Pressure induced 'super-filling' of the pores at GPa pressure (the initial content of the framework can interact or be exchanged with penetrating guest molecules at high pressure, including examples of pressure-induced hydration).
- Hydrostatic media dependant compression (the medium in which the sample is compressed plays a pivotal role in how the framework material responds to high pressure, dramatically changing the compressibility).
- Framework and hydrostatic medium dependent amorphization (sufficient applied pressure can **cause** the framework to lose crystallinity and become amorphous; a process that is also affected by medium choice and initial framework content).

In this Thesis, we explore these phenomena further by studying a series of porous metal organic framework (or MOF) materials under high hydrostatic pressure conditions, including **MOF-5** ($[Zn_4O(BDC)_3]$, BDC=1,4-benzenedicarboxylate); **Cu-btc** ($[Cu_3(btc)_2(H_2O)_3]n$, btc=benzene-1,3,5-tricarboxylate); **STAM-1** ($(Cu_3O_{21}C_{30}H_{24})n.5n(H_2O)$); **ZIF-8** ($[Zn(MeIM)_2]$, MeIM = 2-methylimidazolate); **Sc_2BDC_3** and **$Sc_2(NO_2\text{-}BDC)_3$**. As outlined above, MOFs contain much larger pores than any of the porous zeolites and aluminophosphates, and are composed of inherently much more flexible building blocks, and as such are amenable to much more drastic changes in pore size and shape at elevated pressures. The studies of porous MOFs at pressure presented here represent all but two of the published studies which examined Cu-btc and ZIF-8.

1.6 References

1 J. Rouquerol, D. Avnir, C. W. Fairbridge, D. H. Everett, J. H. Haynes, N. Pernicone, J. D. F. Ramsay, K. S. W. Sing and K. K. Unger, *Pure Appl. Chem.*, 1994, **66**, 1739.

2 K. S. W. Sing, D. H. Everett, R. A. W. Haul, L. Moscou, R. A. Pierotti, J. Rouquerol and T. Siemieniewska, *Pure Appl. Chem.*, 1985, **57**, 603.

3 H. Furukawa, M. A. Miller and O. M. Yaghi, *J. Mater. Chem.*, 2007, **17**, 3197; X. Lin, J. Jia, X. Zhao, K. M. Thomas, A. J. Blake, G. S. Walker, N. R. Champness, P. Hubberstey and M. Schroeder, *Angew. Chem., Int. Ed.*, 2006, **45**, 7358; T. Dueren, L. Sarkisov, O. M. Yaghi and R. Q. Snurr, *Langmuir*, 2004, **20**, 2683; L. T. L. Nguyen, K. K. A. Le, H. X. Truong and N. T. S. Phan, *Catal. Sci. Technol.*, 2012, **2**, 521; J.-H. Kim, T. Kunieda and M. Niwa, *J. Catal.*, 1998, **173**, 433; J. Lee, O. K. Farha, J. Roberts, K. A. Scheidt, S. T. Nguyen and J. T. Hupp, *Chemical Society Reviews*, 2009, **38**, 1450.

4 U. Vietze, O. Krauss, F. Laeri, G. Ihlein, F. Schuth, B. Limburg and M. Abraham, *Phys. Rev. Lett.*, 1998, **81**, 4628.

5 Y. Nozue, T. Kodaira and T. Goto, *Phys. Rev. Lett.*, 1992, **68**, 3789; M. Kurmoo, *Chemical Society Reviews*, 2009, **38**, 1353.

6 M. D. Allendorf, C. A. Bauer, R. K. Bhakta and R. J. T. Houk, *Chemical Society Reviews*, 2009, **38**, 1330.

7 A. F. Cronstedt, *Akad Handl*, 1756, **18**, 120.

8 C. Baerlocher and L. B. McCusker, Database of Zeolite Structures, http://www.iza-structure.org/databases/.

9 J. Scherzer, in *Catalytic Materials: Relationship Between Structure and Reactivity*, American Chemical Society, 1984, pp. 157-200.

10 A. P. Wight and M. E. Davis, *Chem. Rev. (Washington, DC, U. S.)*, 2002, **102**, 3589.

11 H. Lv, M. Yao, Q. Li, R. Liu, B. Liu, S. Lu, L. Jiang, W. Cui, Z. Liu, J. Liu, Z. Chen, B. Zou, T. Cui and B. Liu, *J. Appl. Phys.*, 2012, **111**, 112615/1.

12 S. E. Dapurkar, H. Kawanami, T. Yokoyama and Y. Ikushima, *New J. Chem.*, 2009, **33**, 538; E. Lehmann, S. Vasenkov, J. Karger, G. Zadrozna, J.

Kornatowski, O. Weiss and F. Schuth, *J. Phys. Chem. B*, 2003, **107**, 4685; S. H. Jhung, H.-K. Kim, J. W. Yoon and J.-S. Chang, *J. Phys. Chem. B*, 2006, **110**, 9371; M. Tiemann and M. Froeba, *Chem. Mater.*, 2001, **13**, 3211.

13 N. Wang, Z. K. Tang, G. D. Li and J. S. Chen, *Nature*, 2000, **408**, 50.

14 R. M. Hazen, *Science*, 1983, **219**, 1065.

15 R. J. Angel, *NATO Sci. Ser., II*, 2004, **140**, 21.

16 R. M. Hazen and L. W. Finger, *J. Appl. Phys.*, 1984, **56**, 1838.

17 I. A. Belitsky, B. A. Fursenko, S. P. Gabuda, O. V. Kholdeev and Y. V. Seryotkin, *Phys. Chem. Miner.*, 1992, **18**, 497; R. Arletti, G. Vezzalini, A. Morsli, R. F. Di, V. Dmitriev and S. Quartieri, *Microporous Mesoporous Mater.*, 2011, **142**, 696.

18 M. Colligan, P. M. Forster, A. K. Cheetham, Y. Lee, T. Vogt and J. A. Hriljac, *J. Am. Chem. Soc.*, 2004, **126**, 12015.

19 J. A. Hriljac, *Crystallogr. Rev.*, 2006, **12**, 181.

20 D. Liu, W. Lei, Z. Liu and Y. Lee, *J. Phys. Chem. C*, 2010, **114**, 18819.

21 J. Haines, O. Cambon, C. Levelut, M. Santoro, F. Gorelli and G. Garbarino, *J. Am. Chem. Soc.*, 2010, **132**, 8860.

22 T. Kim, Y. Lee, Y. N. Jang, J. Shin and S. B. Hong, *Microporous Mesoporous Mater.*, 2013, **169**, 42.

23 J. A. Hriljac, M. M. Eddy, A. K. Cheetham, J. A. Donohue and G. J. Ray, *J. Solid State Chem.*, 1993, **106**, 66; Y. Lee, H.-H. Lee, D. R. Lee, S. J. Kim and C.-c. Kao, *J. Solid State Chem.*, 2008, **181**, 730; S. V. Rashchenko, Y. V. Seryotkin and V. V. Bakakin, *Microporous Mesoporous Mater.*, 2012, **159**, 126.

24 R. A. Secco, S. V. Goryainov and Y. Huang, *physica status solidi (b)*, 2005, **242**, R73.

25 Y. Lee, T. Vogt, J. A. Hriljac, J. B. Parise and G. Artioli, *J. Am. Chem. Soc.*, 2002, **124**, 5466.

26 Y. Lee, J. A. Hriljac, J. B. Parise and T. Vogt, *Am. Mineral.*, 2005, **90**, 252.

27 W. H. Baur, *Cryst. Res. Technol.*, 1991, **26**, K169; F. Pechar, *Cryst. Res. Tech.*, 1988, **23**, 647.

28 Y. Lee, J. A. Hriljac and T. Vogt, *Phys. Chem. Miner.*, 2004, **31**, 421.

29 Y. Lee, J. A. Hriljac, T. Vogt, J. B. Parise, M. J. Edmondson, P. A. Anderson, D. R. Corbin and T. Nagai, *J. Am. Chem. Soc.*, 2001, **123**, 8418.

30 B. A. Reisner, B. H. Toby, Y. Lee, J. B. Parise, J. Z. Larese, V. Kahlenberg, J. C. Hanson, A. Freitag, G. A. Jones and D. R. Corbin, *Chem. Commun.*, 2000, 2221.

31 G. N. Greaves, F. Meneau, A. Sapelkin, L. M. Colyer, G. I. ap, S. Wade and G. Sankar, *Nat. Mater.*, 2003, **2**, 622; N. Greaves and F. Meneau, *J. Phys.: Condens. Matter*, 2004, **16**, S3459.

32 M. D. Rutter, T. Uchida, R. A. Secco, Y. Huang and Y. Wang, *J. Phys. Chem. Solids*, 2001, **62**, 599.

33 J. E. Readman, P. M. Forster, K. W. Chapman, P. J. Chupas, J. B. Parise and J. A. Hriljac, *Chem. Commun.*, 2009, 3383.

34 A. Isambert, E. Angot, P. Hebert, J. Haines, C. Levelut, R. Le Parc, Y. Ohishi, S. Kohara and D. A. Keen, *J. Mater. Chem.*, 2008, **18**, 5746.

35 G. N. Greaves, F. Meneau, F. Kargl, D. Ward, P. Holliman and F. Albergamo, *J. Phys.: Condens. Matter*, 2007, **19**, 415102/1.

36 S. A. Sapchenko, D. G. Samsonenko, D. N. Dybtsev, M. S. Melgunov and V. P. Fedin, *Dalton Trans.*, 2011, **40**, 2196; B. Chen, S. Xiang and G. Qian, *Acc. Chem. Res.*, 2010, **43**, 1115; Z.-Z. Lu, R. Zhang, Y.-Z. Li, Z.-J. Guo and H.-G. Zheng, *J. Am. Chem. Soc.*, 2011, **133**, 4172; T. Lee, Z. X. Liu and H. L. Lee, *Cryst. Growth Des.*, 2011, **11**, 4146.

37 A. Huang, W. Dou and J. Caro, *J. Am. Chem. Soc.*, 2010, **132**, 15562; G. Lu and J. T. Hupp, *J. Am. Chem. Soc.*, 2010, **132**, 7832; W. Morris, B. Leung, H. Furukawa, O. K. Yaghi, N. He, H. Hayashi, Y. Houndonougbo, M. Asta, B. B. Laird and O. M. Yaghi, *J. Am. Chem. Soc.*, 2010, **132**, 11006; F. Salles, G. Maurin, C. Serre, P. L. Llewellyn, C. Knofel, H. J. Choi, Y. Filinchuk, L. Oliviero, A. Vimont, J. R. Long and G. Ferey, *J. Am. Chem. Soc.*, 2010, **132**, 13782.

38 J. Y. Lee, O. K. Farha, J. Roberts, K. A. Scheidt, S. B. T. Nguyen and J. T. Hupp, *Chem. Soc. Rev.*, 2009, **38**, 1450.

39 V. K. Peterson, C. M. Brown, Y. Liu and C. J. Kepert, *J. Phys. Chem. C*, 2011, **115**, 8851; W. L. Queen, C. M. Brown, D. K. Britt, P. Zajdel, M. R.

Hudson and O. M. Yaghi, *J. Phys. Chem. C*, 2011, **115**, 24915; J. L. C. Rowsell, E. C. Spencer, J. Eckert, J. A. K. Howard and O. M. Yaghi, *Science*, 2005, **309**, 1350; J.-P. Zhang, A.-X. Zhu and X.-M. Chen, *Chem. Comm.*, 2012, **48**, 11395.

40 T. D. Bennett, J.-C. Tan, S. A. Moggach, R. Galvelis, C. Mellot-Draznieks, B. A. Reisner, A. Thirumurugan, D. R. Allan and A. K. Cheetham, *Chem.Eur. J.*, 2010, **16**, 10684; L. Marleny Rodriguez-Albelo, A. R. Ruiz-Salvador, A. Sampieri, D. W. Lewis, A. Gomez, B. Nohra, P. Mialane, J. Marrot, F. Secheresse, C. Mellot-Draznieks, R. Ngo Biboum, B. Keita, L. Nadjo and A. Dolbecq, *J. Am. Chem. Soc.*, 2009, **131**, 16078; A. M. Walker, B. Civalleri, B. Slater, C. Mellot-Draznieks, F. Cora, C. M. Zicovich-Wilson, G. Roman-Perez, J. M. Soler and J. D. Gale, *Angew. Chem., Int. Ed.* , 2010, **49**, 7501.

41 S. A. Moggach, T. D. Bennett and A. K. Cheetham, *Angew. Chem., Int. Ed.* , 2009, **48**, 7087.

42 K. W. Chapman, G. J. Halder and P. J. Chupas, *J. Am. Chem. Soc.*, 2008, **130**, 10524.

43 D. Fairen-Jimenez, S. A. Moggach, M. T. Wharmby, P. A. Wright, S. Parsons and T. Düren, *J. Am. Chem. Soc.*, 2011, **133**, 8900.

44 J. P. S. Mowat, S. R. Miller, J. M. Griffin, V. R. Seymour, S. E. Ashbrook, S. P. Thompson, D. Fairen-Jimenez, A.-M. Banu, T. Düren and P. A. Wright, *Inorg. Chem.*, 2011, **50**, 10844.

45 R. Vaidhyanathan, D. Bradshaw, J.-N. Rebilly, J. P. Barrio, J. A. Gould, N. G. Berry and M. J. Rosseinsky, *Angew. Chem., Int. Ed.*, 2006, **45**, 6495.

46 C. Serre, F. Millange, C. Thouvenot, M. Nogues, G. Marsolier, D. Louer and G. Ferey, *J. Am. Chem. Soc.*, 2002, **124**, 13519; C. Volkringer, T. Loiseau, N. Guillou, G. Ferey, E. Elkaim and A. Vimont, *Dalton Trans.*, 2009, 2241; F. Millange, N. Guillou, I. Walton Richard, J.-M. Greneche, I. Margiolaki and G. Ferey, *Chem. Commun.*, 2008, 4732.

Chapter 2

The effect of pressure on MOF-5: guest induced modification of pore size and content at high pressure*

*Alexander J. Graham, David R. Allan, Anna Muszkiewicz, Carole Morrison and Stephen A. Moggach, *Angew. Chem. Int. Ed.*, (2011), 50(47), 11138-11141

2.1 Introduction

Recent interest in gas storage materials has led to the accumulation of a large volume of work on the physical properties and possible applications of metal organic framework materials. Herein we present the first high-pressure study on the prototypical MOF, MOF-5 ($[Zn_4O(BDC)_3]$, BDC=1,4-benzenedicarboxylate) to 3.2 GPa. MOF-5 crystallizes in the cubic space group $Fm\bar{3}m$. The structure is composed of an oxide-centred Zn_4O tetrahedron edge-bridged by six carboxylate groups which create an octahedral secondary building unit (SBU). These SBUs build up to give a three-dimensional porous network with each pore having a volume of approximately 1600 $Å^3$ (Figure 1).

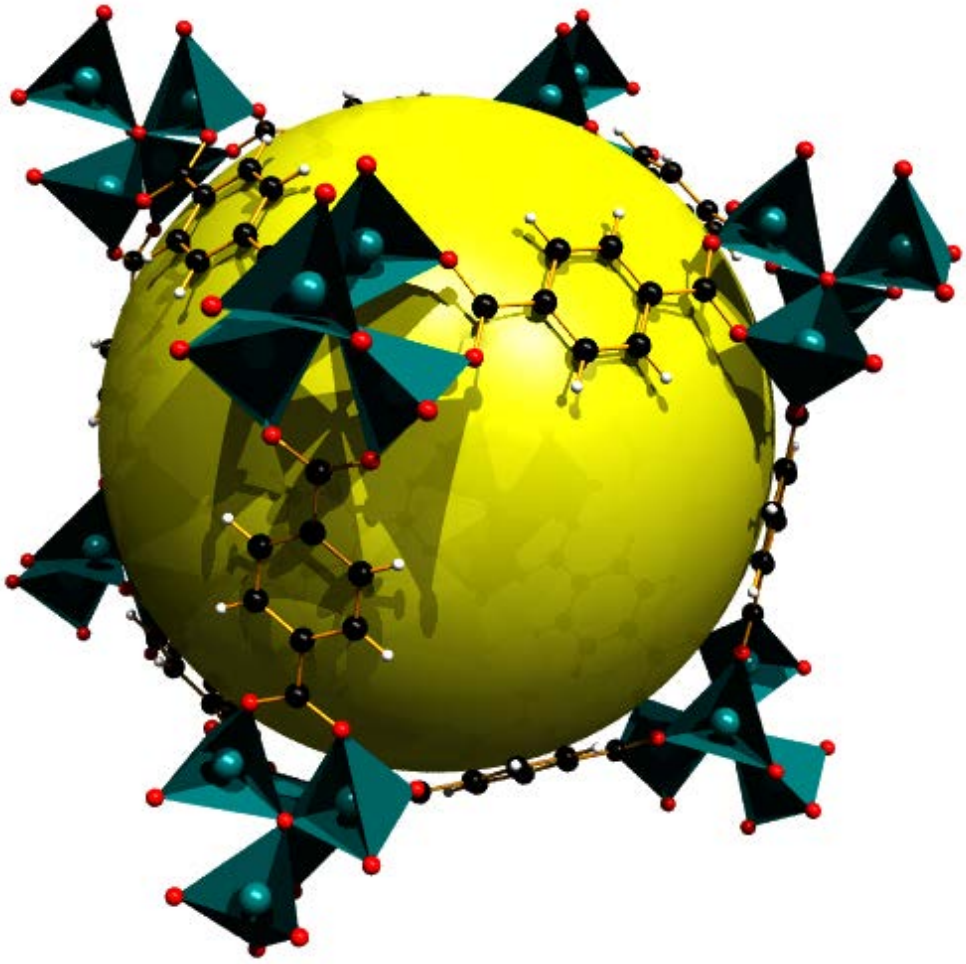

Figure 1. Packing arrangement demonstrating the pore structure of MOF-5. ZnO_4 units are drawn as rigid polyhedra. The large yellow sphere represents the largest van der Waals sphere that would fit in the cavity without touching the framework. There are eight of these units per unit cell. Key: Zn, teal; O, red; C, black; H, grey.

2.2 Experimental

2.2.1 Sample preparation

Suitably sized single crystals of MOF-5 for X-ray structural analysis were synthesized by heating a solution of zinc nitrate hexahydrate (5g, Aldrich) and terephthalic acid (25.9 g, Aldrich) in *N*,*N*-diethylformamide (800 cm^3, Aldrich). Reactants were completely dissolved by mixing continuously for 30 minutes. 5 x 20 cm^3 of this solution was then decanted into five separate 150 cm^3 jars fitted with Teflon gasketed lids and placed into Parr acid digestion bombs. These samples were then placed in an oven for 16 h at 100 $^{\circ}$C. A dark yellow liquid was removed using a syringe from each vile, which contained colourless crystals of MOF-5. The yellow liquid was then decanted and replaced with fresh *N*,*N*-diethylformamide twice.

2.2.2 Synchrotron high-pressure single-crystal X-ray measurements

A single crystal of MOF-5 was loaded into a Merrill-Bassett diamond anvil cell (half opening angle 40°), equipped with Boehlar Almax diamonds with 600 μm culets (Figure 2), a tungsten gasket and tungsten carbide backing plates.[1] Diethylformamide was used as the pressure-transmitting medium. A small ruby chip was used as a pressure calibrant, using the ruby fluorescence method to measure the pressure.[2] Diffraction data were collected on a Rigaku Saturn 724 CCD detector using synchrotron radiation (λ = 0.5159 Å) on station I19 at the DIAMOND Light Source, Rutherford Appleton Laboratory from 0.34 to 3.24 GPa. Data collection and processing procedures followed a modified version of the Dawson *et al*.,[3] using an a step size and exposure time of 1° and 1 s respectively. Data were integrated using dynamic masking of regions of the detector shaded by the pressure cell using the programme SAINT.[4] Absorption corrections were carried out with the program SADABS.[5] Data were merged using SORTAV.[6]

Figure 2. Optical image of a single crystal of MOF-5 at 0.3 GPa in a diamond-anvil cell.

2.2.3 Laboratory single-crystal X-ray measurements

A sphere of data was collected on a crystal of MOF5 at ambient temperature and pressure using a MiTeGen Microloops™ mount with the DEF solvent (used as the solvent system during synthesis) supported above the crystal in a capillary in order to provide data for comparison with the high pressure studies, which were also performed at ambient temperature. Diffraction data were collected on a single crystal on a Bruker SMART APEX II diffractometer with graphite-monochromated Mo Kα radiation (λ = 0.71073 Å). These data were integrated using the program SAINT, while the absorption correction was carried out using the program SADABS.

High pressure diffraction data were collected on the same crystal on a Bruker APEX II diffractometer with graphite-monochromated Mo Kα radiation (λ = 0.71073 Å). Data were collected in ω-scans in eight settings of 2θ and φ with a frame time

and step size of sixty seconds and 0.3° respectively. This data collection strategy was based on that described by Dawson *et al*. The data were integrated using the program SAINT using 'dynamic masks' to avoid integration of regions of the detector shaded by the body of the pressure cell. Absorption corrections for the DAC and sample were carried out with the programs SHADE[7] and SADABS respectively. Data were collected from 0.14 GPa up to a final pressure of 3.21 GPa.

2.2.3 Structure refinements

Structure refinements were carried out in CRYSTALS[8] using the starting coordinates for MOF-5 determined at ambient pressure and 258 K by Eddaoudi *et al.*, 2002[9] (CSD refcode EDUSIF). All structures were refined anisotropically against $|F|^2$. 1,2 and 1,3 restraints were used on the terephthalate ligand, all Zn-ligand distances were allowed to refine freely. H-atom positions were placed geometrically and constrained to ride on their host atoms. The pore volume and solvent content were calculated using the *SQUEEZE* algorithm within PLATON.

On increasing pressure, a gradual reduction in resolution of the data is observed. In order to establish the effect this has on the calculated electron density in the pore we have artificially reduced the resolution of all data sets to 1.46 Å (the resolution limit of the data collected at 2.3 GPa) and tabulated these results below in comparison to the electron density calculated to the resolution limit of each pressure.

2.2.2 TLS analysis

In order to evaluate the effect libration could have on the measured Zn-O bond lengths, we have performed TLS (translation/libration/screw) analysis on the $Zn_4O(CO_2)_6$ unit and subsequently recalculated the Zn-O bonds corrected for libration[10] by a least-squares fit to the individual anisotropic temperature factor components of the unit. Calculations were performed in the program CRYSTALS.

TLS determines 20 variables from the individual U_{ij} of the nominated atoms. There are only six non-hydrogen atoms in the asymmetric unit, giving 36 U_{ij} values (observations), just 16 more observations than variables. In order to increase the number of observations, we expanded the structure to include the whole $Zn_4O(CO_2)_6$ unit.

The resulting tensors for MOF-5 at 0.3 GPa were:

$$\mathbf{L}\begin{pmatrix} -2.9714 & 0.0000 & 6.2552 \\ 0.0000 & 119.3732 & 0.0000 \\ 6.2552 & 0.0000 & -2.9714 \end{pmatrix} \quad \mathbf{T}\begin{pmatrix} 0.1382 & 0.0000 & 0.0222 \\ 0.0000 & 0.0711 & 0.0000 \\ 0.0222 & 0.0000 & 0.1382 \end{pmatrix} \quad \mathbf{S}\begin{pmatrix} 0.0000 & 0.0000 & 0.0000 \\ -0.0001 & 0.0000 & 0.0001 \\ 0.0000 & 0.0000 & 0.0000 \end{pmatrix}$$

These values show that libration, L, has some slightly negative values due to the included symmetry equivalent atoms in the $Zn_4O(CO_2)_6$ unit. The translational, T, values confirm that the molecule is translationally vibrating and the screw component, S, is Null. Overall there were no significant changes observed in the measured bond distances due to limited libration.

2.2.3 Computational work

All calculations were performed using the CASTEP (version 5.0) simulation package.[11] Starting coordinates were taken from the ambient pressure, 30 K, X-ray diffraction structure of MOF-5 by Rowsell *et al*. (CSD refcode SAHYOQ02).[12] The Hamiltonian operator was approximated using the Perdew-Burke-Ernzerhof (PBE) exchange-correlation functional,[13] with the molecular wavefunction description provided by 'on-the-fly' pseudopotentials and a plane wave basis set operating at 550 eV, which gave convergence to within 4 meV per atom. The electronic structure was sampled at the gamma position only in the Brillouin zone due to the large size of the primitive unit cell; since MOF-5 is an electronic insulator, no problems were anticipated with under sampling of the electronic band structure.

The geometry optimisation calculations were run without any symmetry constraints, thus allowing for an independent variation of both the atomic positions and the primitive cell parameters. The potential energy surface was searched for energy minima by means of the Broyden-Fletcher-Goldfarb-Shanno (BFGS) algorithm. Structures were considered to be optimised when the energy per atom, maximum force, maximum stress, and maximum atomic displacement converged to the values of 0.02 meV/atom, 0.05 eV/Å, 0.1 GPa, and 0.002 Å, respectively. Once the first, ambient pressure, model was optimised, an external hydrostatic pressure of 0.3 GPa was applied and the system re-optimised. The resultant structure was then

used as the starting point for the next pressure measurement, which continued in approximate 0.3 GPa increments up to 3.2 GPa.

2.3 Results and discussion

2.3.1 The effect of pressure on MOF-5 in diethyl formamide

Our first measurement at 0.33(8) GPa showed that the pores contained on average 119 DEF molecules per unit cell. On initial application of pressure to 0.78(5) GPa, a rather counterintuitive unit cell volume *increase* of 144 $Å^3$ was observed and coincided with a moderate solvent content increase (9 DEF molecules, Table 1). Initial application of pressure therefore resulted in solvent being squeezed into the pores, making the framework resilient to compression. Although this action does result in a slight increase in pore volume, the change here is very modest (ca. 0.8%) but still statistically significant.

On further increasing the pressure to 1.35(7) GPa the volume finally began to decrease, although we note that the volume here at *ca.* 13000 atmospheres is almost identical to that at 0.33(8) GPa. What is not immediately obvious on the basis of the unit cell volume alone is that a marked and sudden *decrease* in solvent content (42 %) occurs as the DEF is now squeezed out of the pores. Increasing pressure further to 3.24(1) GPa resulted in behavior atypical to molecular materials under pressure, with a gradual and steady reduction in volume. Three regions could therefore be identified, the first (0.33(8)-0.78(5) GPa) involves inclusion of DEF into the pores, the second (0.78(5)-2.01(4) GPa) resulted in compression and evacuation of the framework, rather than the uptake of more solvent, while the region above 2.01(4) GPa and beyond to 3.24(1) GPa resulted in a sharper drop in unit cell volume, and compression of the framework.

Table 1. Crystallographic and pore data for MOF-5_{DEF} as a function of pressure.

Pressure (GPa)	*a* (Å)	Total Pore Volume (Å³)	Electron Count	No. DEF Molecules
0.33(8)	25.761(6)	13020	6667	119
0.78(5)	25.832(8)	13221	7175	128
1.35(7)	25.732(6)	12962	4163	74
1.53(12)	25.656(11)	12893	4217	75
1.70(6)	25.626(8)	12825	4053	72
2.01(4)	25.587(15)	12936	3947	70
2.35(8)	25.40(3)	12415	3739	67

During the pressure experiment, the single crystal began to shatter, becoming polycrystalline, while a gradual reduction in resolution of the data was observed, reducing from 0.9 to 1.7 Å. Owing to the decrease in resolution, atomic coordinates could only be refined reliably to 2.35(8) GPa, although unit cell dimensions could be determined up to 3.24(1) GPa. At pressures above 3.24(1) GPa the sample became completely amorphous, making extraction of structural data by these techniques impossible. In order to follow the progression of amorphization the intensity of the (022) reflection was mapped as a function of pressure (Figure 3). The reversibility of this process is currently unknown.

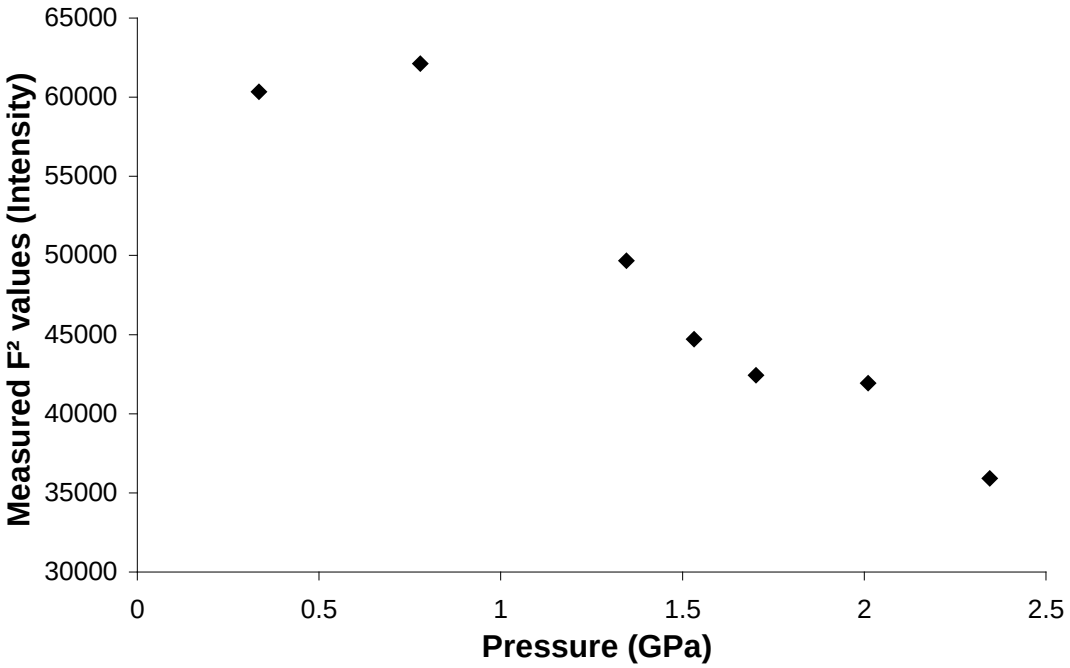

Figure 3. Measured intensity for the 022 reflection as a function of pressure. Note the sudden decrease in intensity above 0.779 GPa.

Amorphization at pressure has been observed in the porous framework ZIF-8 using a pressure-transmitting media which was non-penetrating into the pore,[14] and has also been reported for MOF-5 during grinding experiments by Hu *et al*.[15] In this latter work, samples were ground for 30 minutes and then subjected to (ambient pressure) powder X-ray diffraction measurements. Although amorphization of MOF-5_{DEF} is eventually observed in our study, it is at pressures several orders of magnitude higher than that observed by Hu and co-workers. Although the hydrostatic limit of DEF is currently unknown, and the onset of amorphization could be caused by applying pressures above this limit, it does appear that applying pressure using a hydrostatic fluid that can penetrate into the framework stabilizes MOF-5 to external pressure thereby delaying the onset of amorphization of the sample.

The fact that we observed unit cell volume expansion under modest conditions of pressure in the presence of a small-molecule solvent requires further investigation. Nevertheless, de-convoluting the effect of pressure and solvent inclusion/exclusion as a function of pressure is extremely difficult to achieve. In a

previous high-pressure study of HKUST-1 this was achieved by surrounding the sample with a pressure transmitting medium that was too large to enter the pores.[16] Direct compression of the framework was then observed, although no detailed structural data was obtained. Similar experiments cannot be performed on MOF-5 because of the size of the cavities. The diameter of the channels at 0.3 GPa measures around 7.6 Å,[17] and have previously been shown to be large enough to encapsulate (and separate) organic dyes.[18] In order to establish the effect of solvent inclusion, we therefore turned to density functional theory (DFT) calculations to simulate the effect of pressure on the unit cell volume of MOF-5 in the absence of the pressure-transmitting medium, hereafter referred to as MOF-5_{Evac}. Our starting model for the computational study was the ambient pressure, 30 K X-ray diffraction structure of MOF-5 by Rowsell *et al*..[12] Our optimized structure returned Zn-O bond lengths that were slightly longer (approximately 0.02 Å) at ambient pressure than those in the experimental study, which in turn leads to a slightly larger calculated lattice parameter. MOF-5 is unusual in that it shows quite a large variation in volume under ambient-pressure conditions, ranging from 16 913.2(3) $Å^3$ (for a completely desolvated sample at 213 K) to 17 369.9(1) $Å^3$ (for an N_2-containing material at 30 K).[12, 19] In fact, MOF-5 has previously demonstrated negative thermal expansion behavior.[20] It is therefore unsurprising that the calculated values at ambient pressure determined here are larger than the experimental data recorded at 30 K. Nevertheless, the calculated geometrical data are within 2.6% of the experimental values and correlate closely with the results of a previous *ab initio* study by Civalleri *et al*.,[21] which helps to validate the computational approach.

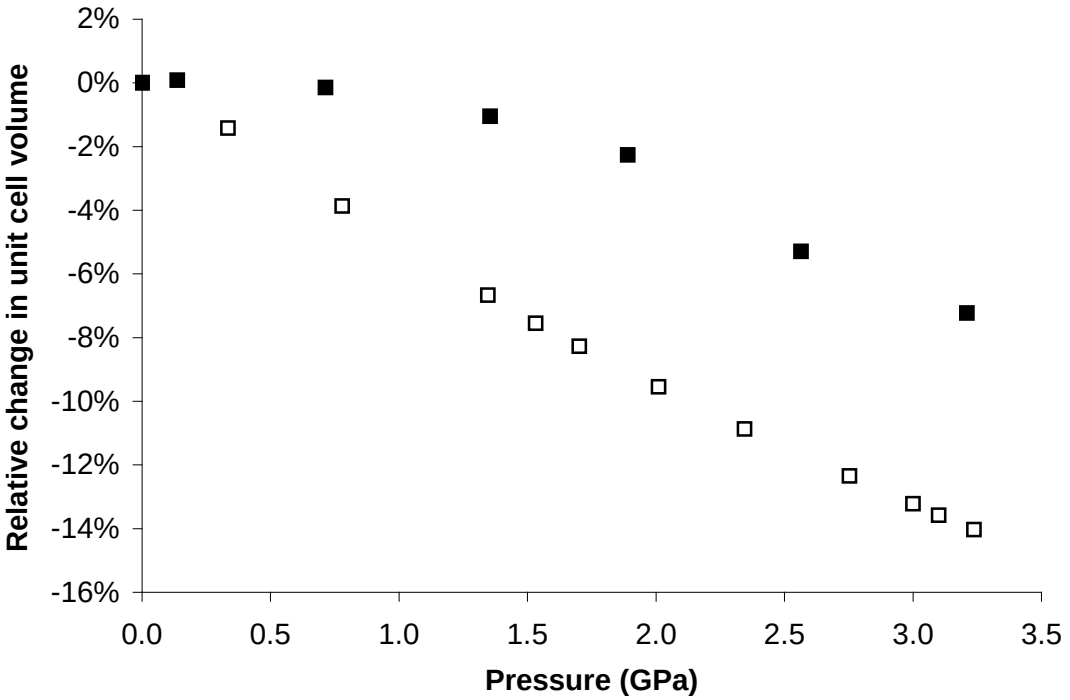

Figure 4. Percentage change in volume for laboratory MOF-5_{DEF} data (filled squares) and MOF-5_{Evac} derived from the computational analysis (empty squares) as a function of pressure.

2.3.2 Comparing compressibility of MOF-5_{DEF} and MOF-5_{Evac}

In previous computational studies of MOF-5, the bulk moduli (*K*), which is a measure of the compressibility of the material was calculated, and found in the range 16.3-18.5 GPa. Reassuringly, we calculate a *K* value of 16.52 GPa for our computational study, which corresponds well with these previous studies. To date, our study on MOF-5_{DEF} is the only experimental data available on the effect of high pressure on MOF-5. The bulk modulus for MOF-5_{DEF}, however is much harder to estimate as pore filling and evacuation of solvent from the framework is a pressure-dependent process. In order to compare our experimental results to the calculated compression (and value of *K*) of the evacuated framework, an ambient temperature and pressure data set was required of a DEF-containing MOF-5 crystal prior to collecting data (on the same sample) at high-pressure. This was achieved by mounting another single-crystal of MOF-5 using a MiTeGen Microloops™ mount with DEF solvent supported above the crystal in a capillary. The same crystal was then loaded into a Merrill-Bassett DAC (as above) and pressure data were collected

to 3.21(7) GPa on a Bruker ApexII 3-circle goniometer with MoKα radiation. Only unit cell parameters could be extracted from these data (Figure 4). Comparisons of laboratory and synchrotron data were also carried out (Figure 5).

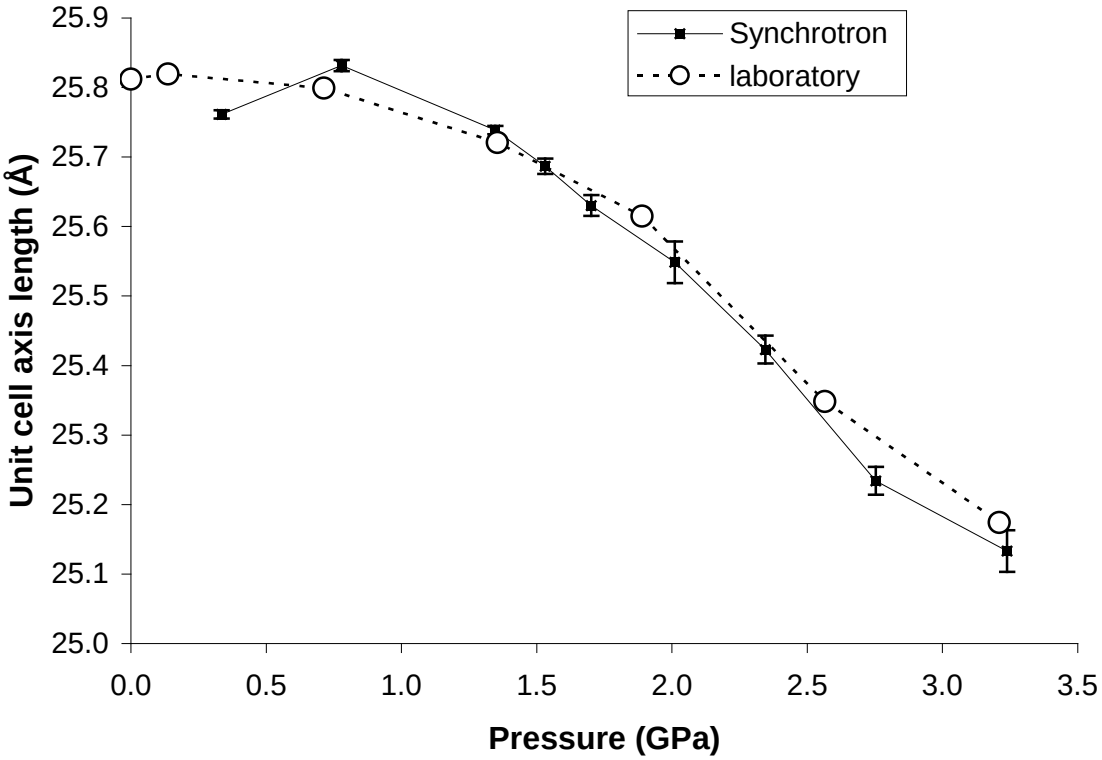

Figure 5. Laboratory and synchrotron unit cell dimensions as a function of pressure.

As the pressure is increased, the difference between MOF-5_{DEF} and MOF-5_{Evac} is obvious: the absence of solvent results in the framework contracting by around 3% (Figure 4). Increasing the pressure further shows a significantly greater reduction in volume on compression of the evacuated framework. Quantifying the rate of change of the experimental data, however, proved impossible using universal Vinet or Birch–Murnaghan equation of states, without giving very large uncertainties on the parameters, and physically unrealistic values for both *K* and its first derivative, *K*' (the pressure dependence of *K*) resulted. This is unsurprising because of both the initial expansion and subsequent contraction of the framework. The best that could be achieved was to estimate the bulk modulus by finite difference, which drops

rapidly from 242 GPa (0.1 to 0.7 GPa) to values between 20–40 GPa at higher pressure. The bulk modulus as a function of pressure is shown in Table 1.

Table 2. The bulk modulus calculated as a function of pressure (finite difference).

Pressure range (GPa)	Bulk Modulus, *K* (GPa)
0.00-0.14	-156.1
0.14-0.71	242.5
0.71-1.36	71.4
1.36-1.89	43.8
1.89-2.57	22.3
2.57-3.21	33.3

This is a remarkable difference in compressibility. To put this into perspective, some examples of *K* include 25 GPa for NaCl, 37 GPa for quartz (a soft mineral), and 440 GPa for diamond. Clearly these much higher values can be attributed to the pore-filling mechanism recognized in the lower pressure regime which significantly decreases the compressibility of the material.

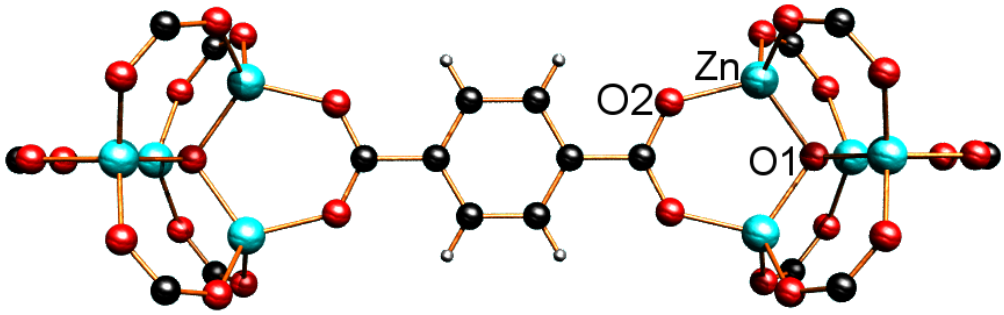

Figure 6. Axial component of MOF-5 comprising a terephthalic acid moiety bordered by Zn_4O_{13} fragments. The two symmetry independent Zn-O bonds, Zn-O1 and Zn-O2, are shown.

Previous high-pressure work on amino acids has shown that covalent bonds do not compress within this pressure regime.[22] Metal-ligand bond distances are however much more amenable to pressure modification, including pressure-induced co-ordination changes.[23] Here, we observe that the compression of MOF-5 is mediated

through the Zn-O bonds. Because of the high-symmetry of the complex, there are only two symmetry independent Zn-O bond distances, labeled Zn-O1 and Zn-O2. These bonding interactions are to a μ^4-oxygen atom (O1) which sits at the centre of the Zn_4O_{13} cluster, and a carboxyl oxygen atom, (O2).

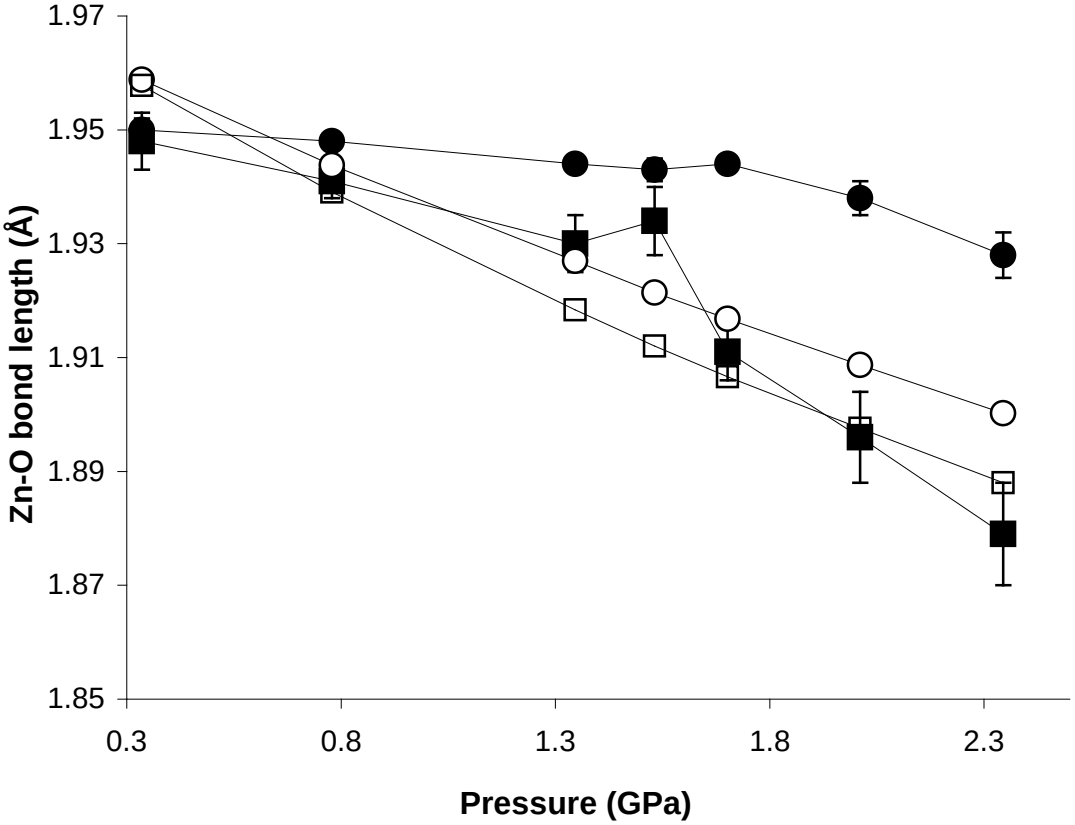

Figure 7. Variation in Zn-O1 (circles) and Zn-O2 (squares) bond lengths in MOF-5_{DEF} and MOF-5_{Evac} as a function of pressure. Filled and empty data points refer to MOF-5_{DEF} and MOF5-5_{Evac} (derived from the computational analysis) respectively.

On increasing pressure the displacement parameters of all the atoms increased in size. In previous studies of MOF-5 as a function of temperature, thermal motion of the BDC ligand gave rise to negative thermal expansion of the framework. The increase in the anisotropic displacement parameters here however, is a consequence of the reduction in resolution of the data. Nevertheless, in order to remove the possibility of any libration effects on measured Zn-O bond lengths we performed TLS analysis on the $ZnO(CO_2)_{12}$ unit and correspondingly corrected all Zn-O bond lengths (Figure 7). The effect on calculated bond lengths here was small.

On comparing the variation in length of Zn-O1 and Zn-O2 over the entire pressure regime in MOF-5_{DEF} and MOF-5_{Evac}, it becomes clear that these bonding interactions do not have the same compressibility. The low pressure region (0.3 to 0.8 GPa) corresponds to solvent inclusion in MOF-5_{DEF} and contraction in MOF-5_{Evac}, with a cross-over point at around 0.8 GPa where the two Zn-O bond lengths are measured, and calculated, to fall within a narrow range. Across the whole experimental data set Zn-O1 shows little variation with pressure. Most of the structural variation is found for Zn-O2. Thus it would appear that it is the Zn-O2 distance that accommodates most of the compression in MOF-5 during the higher pressure region as the pores contract. The Zn-O bonding interaction (Zn-O1) to the μ4-oxygen atom is therefore significantly stiffer than the Zn-carboxylate bond (Zn-O2). EXAFS and total scattering studies would be useful here for tracking bond compression. These techniques are however still being developed at high-pressure and we plan to try these in the future.

In a previous *ab initio* study of MOF-5, Born effective charges showed that the μ^4-oxygen atom O1 had a greater negative charge than the carboxyl oxygen atom O2 by around -0.4 e,[24] a finding that was matched by calculated Mulliken charges in this study. The different nature of the two atoms was also highlighted in the same study by a deformation electron density map, which clearly showed that the O1 atom was similar to the oxygen atom in ZnO wurtzite, while the Zn-O2 bond was clearly formed by charge donation from the oxygen atom. It is therefore not surprising that the Zn-O2 bond is the more compressible of the two bonds, with the high-pressure study here providing an effective proof for this observation. In the simulation, both Zn-O1 and Zn-O2 bonds display a steady compression (of the order of 0.05 and 0.06 Å, respectively). Interestingly, the greater compressibility of Zn-O2 is still observed in the evacuated framework, though not to the same extent. This would indicate that solvent inclusion in MOF-5_{DEF} makes the Zn-O1 (μ^4-oxygen) bond even stiffer. At the moment, it is unclear as to why this would be the case and we are currently investigating this phenomenon.

2.4 Conclusions

In conclusion, we have observed the effect of pressure on the metal organic framework MOF-5 from ambient to 3.2 GPa, and subsequently explored what drives the framework's behavior. Initial compression to 0.8 GPa represents a pressure region where solvent is 'squeezed' into the pores. This is highlighted by comparison with computational results which show direct compression of the evacuated framework. Increasing the pressure further to 1.3 GPa results in a decrease in volume and a sudden marked decrease in solvent content as the solvent is evacuated from the pores. Increasing the pressure to 3.2 GPa resulted in a gradual and steady reduction in volume and resolution of the data as the sample became amorphous. Increasing pressure above 3.2 GPa resulted in complete amorphization of the sample.

When compared with a previous high-pressure study it appears that hydrostatic compression delays the onset of amorphization. This indicates that pressure-induced solvent inclusion makes the framework more resilient to pressure. Compressibility of the framework is mediated through Zn-O bonds. In particular, the Zn-O2 bond (to the carboxyl oxygen atom) shows significantly greater compression than the Zn-O1 bond (to the μ^4-oxygen atom). This is also observed in the computational results on the evacuated framework, though interestingly the Zn-O1 bond here compresses significantly more. How the presence of solvent effects the compressibility of Zn-O bonds is still under investigation.

2.5 References

1 S. A. Moggach, D. R. Allan, S. Parsons and J. E. Warren, *J. Appl. Crystallogr.*, 2008, **41**, 249.

2 G. J. Piermarini, S. Block, J. D. Barnett and R. A. Forman, *J. Appl. Physics*, 1975, **46**, 2774.

3 A. Dawson, D. R. Allan, S. Parsons and M. Ruf, *J. Appl. Crystallogr.*, 2004, **37**, 410.

4 Bruker-Nonius, Bruker-AXS, Madison, Wisconsin, USA, 2006.

5 G. M. Sheldrick, *SADABS Version 2008-1*, 2008.

6 R. H. Blessing, *J. Appl. Crystallogr.*, 1997, **30**, 421.

7 S. Parsons, The University of Edinburgh, Edinburgh, United Kingdom, 2004.

8 P. W. Betteridge, J. R. Carruthers, R. I. Cooper, K. Prout and D. J. Watkin, *J. Appl. Crystallogr.*, 2003, **36**, 1487.

9 M. Eddaoudi, J. Kim, N. Rosi, D. Vodak, J. Wachter, M. O'Keeffe and O. M. Yaghi, *Science*, 2002, **295**, 469.

10 V. Schomaker and K. N. Trueblood, *Acta Crystallogr., Sect. B* 1968, **24**, 63.

11 S. J. Clark, M. D. Segall, C. J. Pickard, P. J. Hasnip, M. J. Probert, K. Refson and M. C. Payne, *Zeitschrift Fur Kristallographie*, 2005, **220**, 567.

12 J. L. C. Rowsell, E. C. Spencer, J. Eckert, J. A. K. Howard and O. M. Yaghi, *Science*, 2005, **309**, 1350.

13 J. P. Perdew, K. Burke and M. Ernzerhof, *Phys. Rev. Lett.*, 1996, **77**, 3865.

14 K. W. Chapman, G. J. Halder and P. J. Chupas, *J. Am. Chem. Soc.*, 2009, **131**, 17546.

15 Y. H. Hu and L. Zhang, *Phys. Rev. B: Condens. Matter Mater. Phys.*, 2010, **81**, 174103/1.

16 K. W. Chapman, G. J. Halder and P. J. Chupas, *J. Am. Chem. Soc.*, 2008, **130**, 10524.

17 O. V. Dolomanov, L. J. Bourhis, R. J. Gildea, J. A. K. Howard and H. Puschmann, *J. Appl. Crystallogr.*, 2009, **42**, 339.

18 S. Han, Y. Wei, C. Valente, I. Lagzi, J. Gassensmith Jeremiah, A. Coskun, J. F. Stoddart and A. Grzybowski Bartosz, *J. Am. Chem. Soc.*, 2010, **132**, 16358.

19 H. Li, M. Eddaoudi, M. O'Keeffe and M. Yaghi, *Nature*, 1999, **402**, 276.

20 N. Lock, Y. Wu, M. Christensen, L. J. Cameron, V. K. Peterson, A. J. Bridgeman, C. J. Kepert and B. B. Iversen, *J. Phys. Chem. C.*, 2010, **114**, 16181.

21 B. Civalleri, F. Napoli, Y. Noel, C. Roetti and R. Dovesi, *CrystEngComm*, 2006, **8**, 364.

22 S. A. Moggach, S. Parsons and P. A. Wood, *Crystallogr. Rev.*, 2008, **14**, 143.

23 S. A. Moggach, K. W. Galloway, A. R. Lennie, P. Parois, N. Rowantree, E. K. Brechin, J. E. Warren, M. Murrie and S. Parsons, *CrystEngComm*, 2009, **11**, 2601.

24 A. Samanta, T. Furuta and J. Li, *J. Chem. Phys.*, 2006, **125**, 084714/1.

Chapter 3

The effect of pressure on Cu-btc: framework compression *vs*. guest inclusion*

* Alexander J. Graham, Jin-Chong Tan, David R. Allan and Stephen A. Moggach, *Chem. Commun*., 2012, **48**, 1535-1537

3.1 Introduction

To date, only three porous framework materials have been exposed to high-pressure, including ZIF-8,[1] MOF-5[2] and Cu-btc.[3] In the previous high-pressure powder diffraction study on the Cu-framework Cu-btc, high-pressure experiments were carried out in the presence of methanol-ethanol-water (MEW, 16 : 3 : 1 by volume), isopropyl alcohol (IPA) and Flourinert (FC-70, perfluorotri-N-pentylamine) as the hydrostatic liquids. In this study, Chapman *et al*. illustrated that with MEW and IPA, the Cu-btc framework exhibits a clear transition between two distinct regions of near linear compressibility. The change in compressibility here was ascribed to a change from a pore filling, to a pore emptying transition, where the transition pressure was affected by the size of the hydrostatic liquid entering the pores (molecules in MEW are smaller than IPA, and therefore delaying the onset of the transition from ~0.8 to ~ 2.2 GPa). When a non-penetrating hydrostatic liquid was used (Fluorinert), direct compression of the framework occurred.

The pore filling mechanism observed on initially applying pressure made Cu-btc much more resilient to compression, and corresponds well with our previous studies of MOF-5 (Chapter 2). However, no detailed structural data was reported. Guest content and framework flexibility was hypothesized from a detailed analysis of the unit cell volume as a function of pressure alone. Herein we present the first single crystal X-ray diffraction study of Cu-btc to 4.96 GPa in MEW.

3.2 Experimental

3.2.1 Sample preparation

An aqueous solution of $Cu(NO_3)_2.3H_2O$ (0.436 g, 6 cm^3, 1.8 mmol) was added to a suspension of 1,3,5- benzenetricarboxylic acid in ethanol (0.21 g, 6 cm^3, 1 mmol). The mixture was placed into the Teflon-lined Parr acid-digestion bomb of 23 cm^3 capacity and heated at 95 °C for 8 h. The crystalline blue product, Cu-btc, was collected by filtration and washed with ethanol.[4]

3.2.2 High-pressure single-crystal X-ray measurements

Prior to our pressure experiment, an ambient pressure and temperature X-ray data set was collected on a crystal of Cu-btc in order to provide data for comparison with the high pressure studies (which were also performed at ambient temperature). The same crystal was then loaded into a Merrill-Bassett Diamond Anvil Cell (DAC; half opening angle 40°) equipped with 600 μm culets and a tungsten gasket[5] using MEW as the hydrostatic liquid. A small ruby chip was used as a pressure calibrant, using the ruby fluorescence method to measure the pressure.[6] Diffraction data were collected on a Rigaku Saturn 724 CCD detector using synchrotron radiation (λ = 0.4859 Å) on station I19 at the DIAMOND Light Source, Rutherford Appleton Laboratory from 0.51 to 4.96 GPa. Data collection and processing procedures followed a modified version of the Dawson *et al.*,2004[7] using an a step size and exposure time of 0.5° and 1 s respectively. Data were integrated using dynamic masking of regions of the detector shaded by the pressure cell using the programme SAINT.[8] Absorption corrections were carried out with the program SADABS.[9] Data were merged using SORTAV.[10]

3.2.3 Structure refinements

Structure refinements were carried out in CRYSTALS[11] using the starting coordinates for Cu-btc determined at ambient pressure and temperature by Chui *et al.*, 1999[12] (CSD refcode FIQCEN). All structures were refined anisotropically against $|F|^2$. 1,2 and 1,3 restraints were used on the terephthalate ligand, all Zn-ligand distances were allowed to refine freely. H-atom positions were placed

geometrically and constrained to ride on their host atoms. The pore volume and solvent content were calculated using the *SQUEEZE* algorithm within PLATON.[13]

3.3 Results and discussion

Cu-btc crystallises in the cubic space group *Fm*-3*m* (*a* = 26.434(6) Å, Vol. = 18471(12) Å^3). Pairs of Cu(II) ions, bridged by four carboxylate (μ_2-OCO) groups on discrete 1,3,5-benzenetricarboxylate (btc) ligands, form Cu(II) dimers (square planar connectivity) which are linked via the trigonal btc molecules to form an extended three-dimensional network. The Cu(II) dimers coordinate to water molecules to form a Jahn–Teller distorted axis creating a distorted octahedral environment around the Cu(II) centres, forming the well known Cu-paddlewheel building unit (Figure 2).

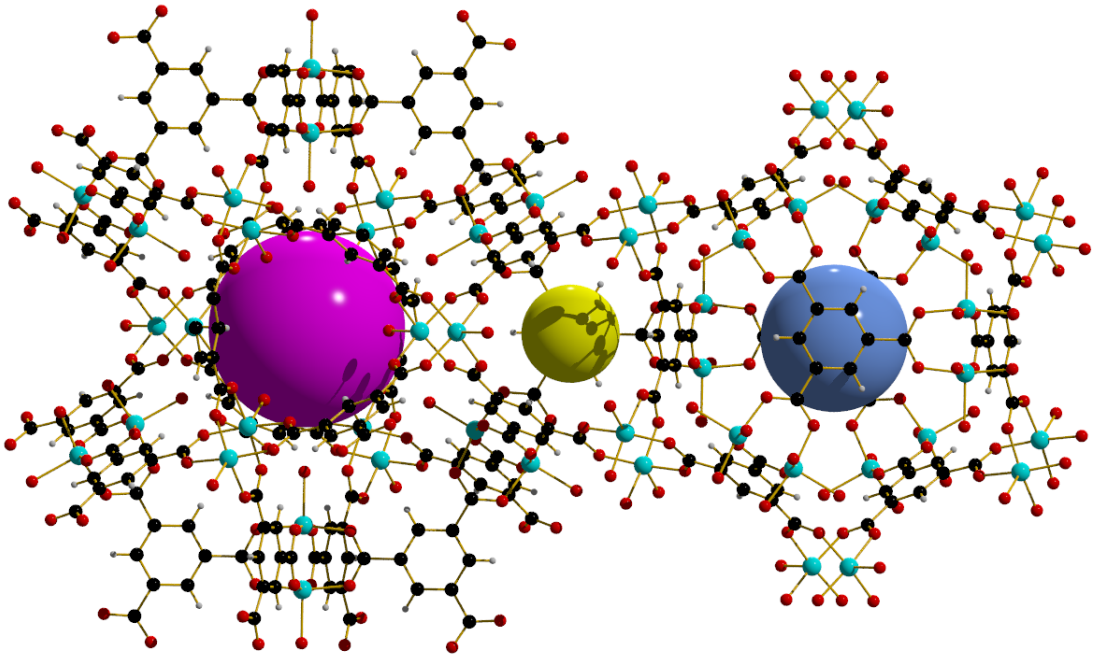

Figure 1. A representation of the three distinct but interconnected pore volumes in Cu-btc. Guest accessible cavities at (0,0,0) (pink), (¼,¼,¼) (yellow) and (½,½,½) (blue) are shown. Key: Cu, turquoise; O, red; C, black; H, white.

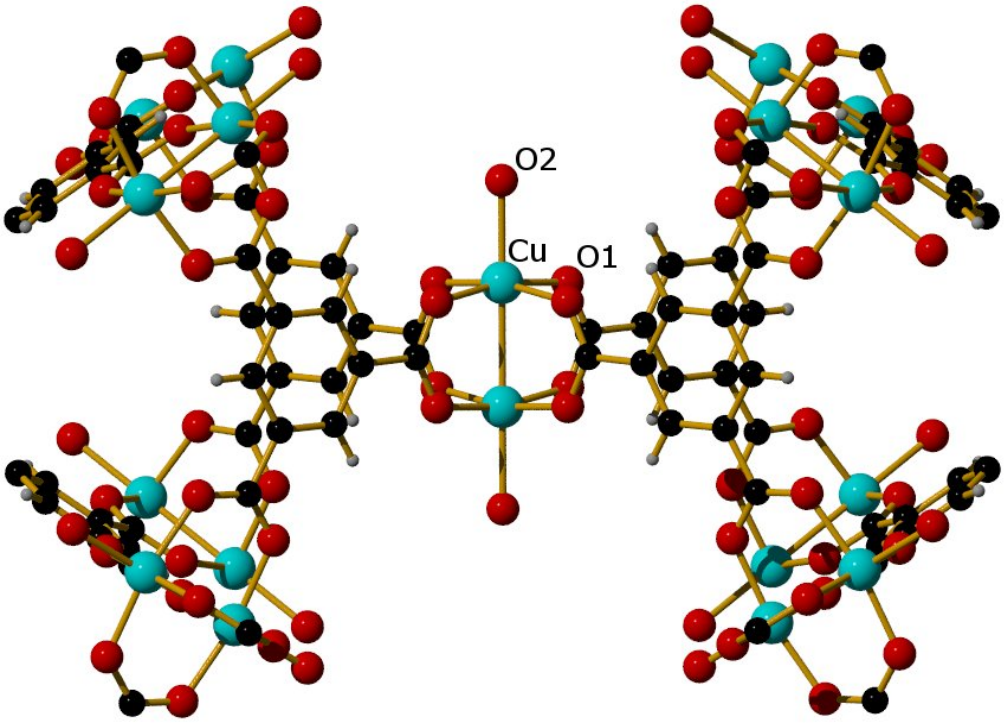

Figure 2. Representation of the Cu paddlewheel units present in Cu-btc showing the equatorial and axial Cu-O bonds, Cu-O1 and Cu-O2, respectively. Key: Cu, turquoise; O, red; C, black; H, white

Cu-btc contains three distinct guest accessible pores which are linked together along the body diagonal ([111] direction) of the cubic structure with a total pore volume of ≈11 500 $Å^3$ (Figure 1). From our ambient pressure single crystal data, it was clear that there were some residual water molecules in the pores equating to 186 water molecules per unit cell. On initially increasing pressure to 0.5 GPa, a sudden and marked increase in pore content was observed, equating to a volume increase on increasing pressure. This coincides well with our previous studies on MOF-5 and ZIF-8 and equates to the uptake of the hydrostatic media within the pores. On increasing pressure further to 3.9 GPa, a gradual and steady increase in pore content was observed, while the volume decreased continuously. The data collected here quite nicely coincides with the previous powder diffraction study by Chapman *et al*., and confirms their hypothesis of a pore filling mechanism within this pressure regime. On increasing pressure further to 5.0 GPa, a sudden and marked decrease in volume occurs, and corresponds to the pore emptying mechanism described previously. However, although a decrease in pore content is observed on increasing pressure from 3.9 to 5.0 GPa, the pore content is not reduced substantially

(≈16% decrease), and equates to approximately the same pore content as observed at 3.0 GPa on increasing pressure (Table 1). Pore volume and solvent content were calculated using the *SQUEEZE* algorithm within the program PLATON.[13] The unit cell volume difference between data collected at 3.0 and 5.0 GPa, however, amounts to only 632 Å^3. It would therefore appear that some other effect, rather than just pore content is responsible for the sudden unit cell volume decrease above 3.9 GPa.

Table 1. Crystallographic and pore data for Cu-btc as a function of pressure. Pore volume and electron count are calculated per unit cell.

Pressure (GPa)	*a* (Å)	Cell volume (Å^3)	Total pore volume (Å^3)	Pore content (electron count)
0.00	26.3015(4)	18194.6(5)	11597	1858
0.51	26.3867(12)	18371.9(14)	11741	2441
1.29	26.3368(12)	18267.9(14)	11656	2689
1.81	26.3081(12)	18208.3(14)	11586	2897
2.21	26.2896(15)	18169.9(18)	11575	3035
2.95	26.2564(15)	18101.1(18)	11519	3337
3.87	26.1823(18)	17948.3(30)	11445	3897
4.96	25.9467(17)	17468.1(20)	10996	3278

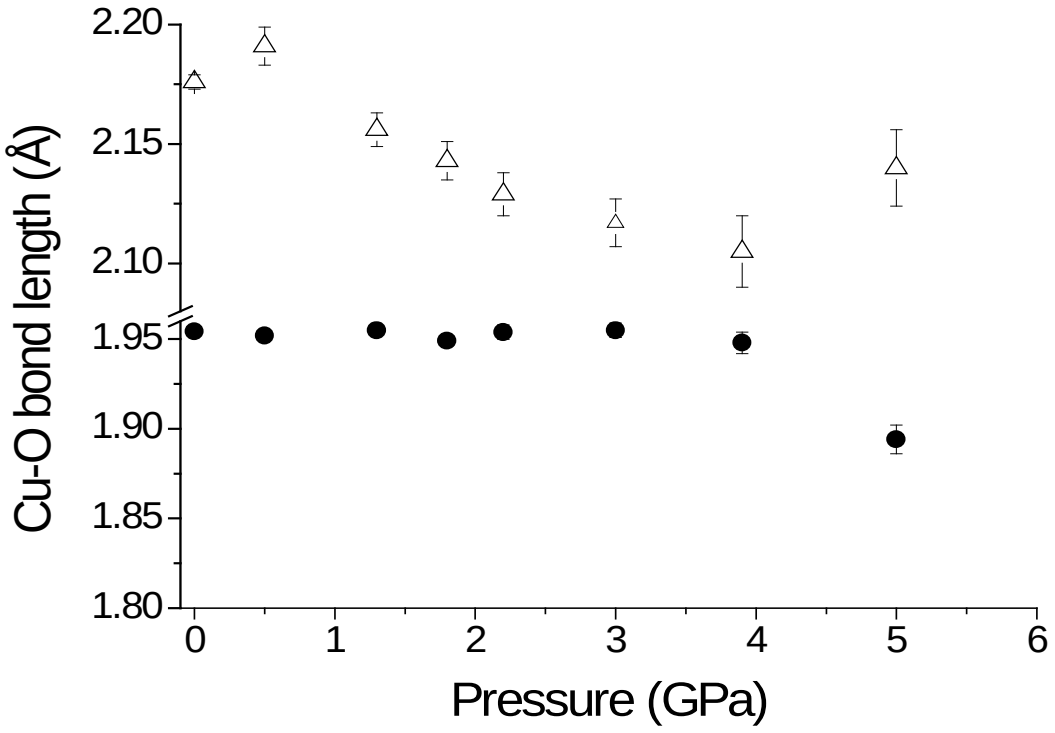

Figure 3. Cu-O1 (closed circles) and Cu-O2 (open triangle) bond lengths of Cu-btc in MEW as a function of pressure.

In our previous work on amino acids, compression of covalent bond lengths is not expected within this pressure regime, rather compression of much weaker intermolecular interactions takes place.[14] This effect has also been modelled computationally by Brand, where a study on pentaerythritol tetranitrate (PETN) showed no significant compression of covalent bond lengths to 6.54 GPa.[15] In contrast metal–ligand bond distances are relatively more flexible and compliant in nature,[16] for example, pressure induced co-ordination changes have been observed.[17] The unit cell compression of Cu-btc is therefore likely to be mediated through the Cu–O bonding interactions within the Cu-paddlewheel. In Cu-btc, there are two symmetry independent Cu–O bonding interactions, the axial Cu–O bond (Cu–O2) which points into the pores of the guest-accessible cavities at (0,0,0) and the equatorial Cu–O bond (Cu–O1, Figure 2) All four Cu–O1 bonds are symmetry equivalent. On initially increasing pressure to 0.5 GPa, no reduction in the equatorial Cu–O1 bonds occurs, while the axial Cu–O2 bond actually increases in length (Figure 3). This coincides nicely with the increase in unit cell volume observed on increasing pressure to 0.5GPa, which suggests that the swelling phenomena observed here is driven by the elongation of the Cu–O2 bonds. We postulate that increasing the pore content with MEW at 0.5 GPa increases H-bonding interactions with the O2 water ligand that points into the large central pore volume at (0,0,0), weakening the Cu–O2 bond causing it to increase in length. It is striking to see that, upon increasing pressure further to 3.9GPa, the axial Cu–O2 bond continuously decreases in length, even though the pore content increases, while the equatorial Cu–O1 bonds remain unchanged (Figure 3). It would therefore appear that after the initial swelling, the overriding drive to smaller volume on applying pressures higher than 0.5 GPa appears to override any energy penalty for compressing the axial Cu–O2 bond.

On increasing pressure to 5.0 GPa (and on entering the pore emptying region), the axial Cu–O2 bond actually increases in length again while the volume and equatorial Cu–O1 bonds (which until now remained relatively unchanged), suddenly decrease (Figure 3). Interestingly, our results therefore demonstrate that the transition at higher pressure is driven not by a decrease in pore content, but by the sudden compression of the significantly stiffer equatorial Cu–O1 bonds. We postulate that the sudden shortening of the Cu–O1 bonds causes the axial Cu-O2

bond to increase in length on undergoing the transition, and the transition here is driven by the need to minimise the volume of the system at 5.0 GPa.

3.4 Conclusions

In conclusion, we have shown that by applying pressure to Cu-btc we can force the hydrostatic medium to enter the pore, initially causing the sample to expand. Expansion of the pore here caused the relatively compliant axial Cu–O bond (Cu–O2), to increase in length (Figure 3). On increasing pressure further to 3.9 GPa, the unit cell volume and the axial Cu–O bond contract, even though more solvent enters the pore, showing that the overall drive to smaller volume overcomes any energy penalty for the swelling phenomena observed on initial application of pressure. On increasing pressure further to 5.0 GPa, we enter a pore emptying region, with which the high pressure squeezes the solvent out of the pores; this is accommodated by the extension of the compliant (axial) Cu–O2 bond. Conversely, the volume decreases quite dramatically here. Importantly, we discover that the transition from a pore filling to a pore emptying mechanism is in fact associated with the sudden compressibility of the stiffer equatorial Cu–O1 bonds. The Cu–O1 bonds are actually very resilient to any compression to 3.9 GPa, and only contract on increasing pressure to 5.0 GPa.

3.5 References

1 S. A. Moggach, T. D. Bennett and A. K. Cheetham, *Angew. Chem., Int. Ed.*, 2009, **48**, 7087.

2 A. J. Graham, D. R. Allan, A. Muszkiewicz, C. A. Morrison and S. A. Moggach, *Angew. Chem., Int. Ed.*, 2011, **50**, 11138.

3 K. W. Chapman, G. J. Halder and P. J. Chupas, *J. Am. Chem. Soc.*, 2008, **130**, 10524.

4 K. Schlichte, T. Kratzke and S. Kaskel, *Microporous Mesoporous Mater.*, 2004, **73**, 81.

5 S. A. Moggach, D. R. Allan, S. Parsons and J. E. Warren, *J. Appl. Crystallogr.*, 2008, **41**, 249.

6 G. J. Piermarini, S. Block, J. D. Barnett and R. A. Forman, *J. Appl. Physics*, 1975, **46**, 2774.

7 A. Dawson, D. R. Allan, S. Parsons and M. Ruf, *J. Appl. Crystallogr.*, 2004, **37**, 410.

8 Bruker-Nonius, Bruker-AXS, Madison, Wisconsin, USA, 2006.

9 G. M. Sheldrick, *SADABS Version 2008-1*, 2008.

10 R. H. Blessing, *J. Appl. Crystallogr.*, 1997, **30**, 421.

11 P. W. Betteridge, J. R. Carruthers, R. I. Cooper, K. Prout and D. J. Watkin, *J. Appl. Crystallogr.*, 2003, **36**, 1487.

12 S. S. Y. Chui, S. M. F. Lo, J. P. H. Charmant, A. G. Orpen and I. D. Williams, *Science*, 1999, **283**, 1148.

13 A. L. Spek, Utrecht University, Utrecht, The Netherlands, 2004.

14 S. A. Moggach, S. Parsons and P. A. Wood, *Crystallogr. Rev.*, 2008, **14**, 143.

15 H. Brand, *J. Phys. Chem. B*, 2005, **109**, 13668.

16 J. C. Tan and A. K. Cheetham, *Chem. Soc. Rev.*, 2011, **40**, 1059.

17 S. A. Moggach, K. W. Galloway, A. R. Lennie, P. Parois, N. Rowantree, E. K. Brechin, J. E. Warren, M. Murrie and S. Parsons, *CrystEngComm*, 2009, **11**, 2601.

Chapter 4

High pressure post-synthetic modification of a Cu-based metal-organic framework

4.1 Introduction

In the field of metal organic frameworks, the pore size and specificity of the resulting material can be modified by derivitisation of the organic linker with a variety of functional groups. Functionalizing the organic component of a MOF can be performed prior to, or after the framework has been formed. Post-synthetic modification (or PSM) has proven to be a very elegant way in which to functionalise MOFs after the framework has formed. To date, two main approaches have been used for PSM of MOFs. The first method involves covalently modifying the organic linker by introducing new functional groups. Examples include post-modification of free pyridyl groups to *N*-methylpyridinium cations in the 2D homochiral MOF D-POST-1; $(C_{72}H_{78}N_{12}O_{31}Zn_3^{2-})_n.2n(H_3O^+).7_n(H_2O)$. This was achieved by treating the crystalline material with excess CH_3I in DMF.[1] In a similar fashion, Cohen and co-workers also showed the PSM of the porous MOF IRMOF-3 ($Zn_4O(H_2N\text{-}BDC)_3$; NH_2-BDC = 2-aminobenzenedicarboxylate), the amino-substituted version of MOF-5 (IRMOF-1). In this study, the amino group on the NH_2-BDC linker was acetylated by reacting the framework with acetic anhydride.[2] Covalent modification of the framework was further expanded to longer chain acid anhydrides. PSM of a gadolinium NH_2-BDC based MOF, was also achieved where the amino group was reacted with ethylisocyanate and acetic acid to form ethylurea and amide functionalised groups respectively.[3] Other examples include a Zn-based paddle-wheel MOF, Zn_2(TCPB)(DPG) (TCPB = 1,2,4,5-tetrakis(4-carboxyphenyl)-benzene, and DPG = *meso*-1,2-bis(4-pyridyl)-1,2-ethanediol), in which Hupp and co-workers were able to introduce free carboxylic acid groups by reacting the native MOF with succinic anhydride.[4]

The second method involves exposing a free site on the metal, usually by removing a ligand. This route has been very successful in modifying the Cu-paddlewheel framework Cu-btc ($[Cu_3(BTC)_2(H_2O)_3]_n$, BTC = benzene-1,3,5-tricarboxylate) in which an axial water ligand can be exchanged for pyridines once the water ligand has been removed.[5] Hupp and co-workers also demonstrated in a 3D non-catenated Zn paddle-wheel MOF, $[Zn_2(L)(dmf)_2]_n(dmf)_n$ (L = (4,4',4'',4'''-benzene-1,2,4,5-tetrayltetrabenzoic acid and DMF = dimethylformamide) that

various pyridine ligands could be introduced on removing the coordinated DMF solvent.[6]

Modification of MIL-101, an iron-based MOF, has also been reported in which coordinated water molecules, removed on dehydration were replaced with chiral L-proline derivatives.[7]

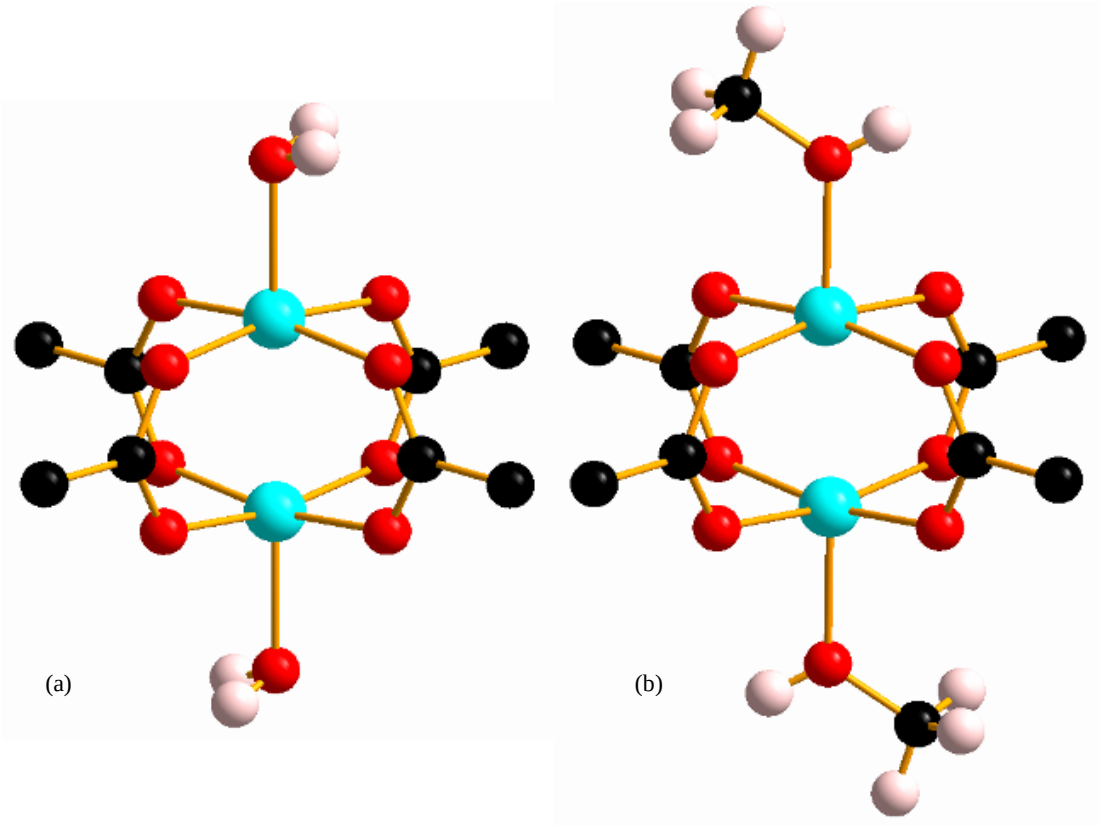

Figure 1. Cu-paddleweheel units in (a) STAM-1 and (b) STAM-1_{MeOH}. Colour scheme O, red; C, black; Cu, blue; and H, pink.

Here, we present the first ever high-pressure post-synthetic modification of a MOF, demonstrated with the Cu-based framework STAM-1 $(Cu_3O_{21}C_{30}H_{24})n.5n(H_2O))$.[8] Under ambient temperature and pressure conditions, STAM-1 contains 5-coordinate Cu 'paddle-wheel' units, similar to that observed in several other MOFs, including Cu-btc and MOF-14 (Cu(II) 4,4',4''-benzene-1,3,5-triyl-tris(benzoate)). These paddle wheels consist of dimeric Cu tetracarboxylate units which form four symmetry-equivalent equatorial Cu-O bonds that measure ≈1.96 Å in length. The 5th (axial) coordination site is filled by a Jahn-Teller distorted

Cu-O bond to a coordinated water molecule, which measures ≈2.15 Å (Figure 1a). Each metal completes a pseudooctahedral coordination sphere with a long Cu-Cu contact (Cu…Cu ≈ 2.6 Å). The preparation of both Cu-btc and STAM-1 involve similar reaction conditions. The synthesis of Cu-btc involves reacting $Cu(NO_3)_2.3(H_2O)$ with benzene-1,3,5-tricarboxylic acid (H_3BTC) in a Teflon-lined autoclave using ethanol as the solvent system. Exchanging the solvent for a 50:50 mixture of water:methanol results in the formation of STAM-1, which is unusual as the H_3BTC linker undergoes selective monoesterification during synthesis to produce a solid with two chemically distinct pore systems, lined by hydrophilic and hydrophobic surfaces.

4.2 Experimental

4.2.1 Synthesis of STAM-1

Single-crystal samples STAM-1 were synthesised by and very gratefully received from M. Infas H. Mohideen in the group of Prof Russell E. Morris at St Andrews University. Below is the procedure followed for the synthesis of this sample:

$Cu(NO_3)_{2.3}(H_2O)$ and 1,3,5-benzenetricarboxylic acid (H_3BTC) were mixed with $MeOH/H_2O$ (50:50) in a Teflon-lined steel autoclave. The mixture was then heated at 383 K for 7 days. The autoclave was cooled to room temperature, and large blue crystals were isolated by Buchner filtration and dried in air.

4.2.2 High-pressure single-crystal X-ray diffraction experiments

4.2.2.1 General procedures

High-pressure experiments were carried out using a modified Merrill-Bassett diamond anvil cell (DAC) equipped with 600 μm culet diamonds and a tungsten gasket.[9] The sample and a chip of ruby (as a pressure calibrant) were loaded into the DAC using one of two hydrostatic media; methanol (MeOH) and isopropyl alcohol (IPA). The ruby fluorescence method was utilised to measure the pressure.[10]

4.2.2.2 Data Collection, Reduction and Refinement

Before each pressure study, an ambient pressure and temperature single-crystal X-ray diffraction data set was collected on a Bruker APEXII diffractometer (Bruker, 2002) with graphite-monochromated Mo *K*α radiation (λ = 0.71073 Å). These data were integrated using the programme SAINT[11], while the absorption corrections were carried out with the program SADABS[12]. Refinements were carried out against $|F|^2$ using all data in CRYSTALS[13]. Pore volume and water content were calculated using the SQUEEZE algorithm within PLATON[14]. Refinement was carried out against $|F|^2$ using all data[15] starting from the ambient temperature coordinates of Mohideen *et al*.[8]

High-pressure single-crystal X-ray diffraction data were collected on beamline I19 at the DIAMOND Light Source (λ = 0.4859 Å). Data were collected in ω-scans in eight settings of 2θ and ϕ with a frame time and step size of one second and 0.5° respectively. This data collection strategy was based on that described by Dawson *et al*.[16] The data were integrated using the program SAINT using 'dynamic masks' to avoid integration of regions of the detector shaded by the body of the pressure cell.[16] Absorption corrections for the DAC and sample were carried out with the programs SHADE[17] and SADABS respectively.

4.2.2.3 Compression study using Isopropyl Alcohol (IPA)

A crystal of STAM-1 was loaded in a DAC with IPA at 0.5 GPa. Data were collected in approximately 0.5 GPa steps up to 2.4 GPa. On increasing pressure from 0.9 to 1.5 GPa, the crystal started to break up, and the resolution deteriorated rapidly. As a result, unit cell dimensions could only be reported above 0.9 GPa. Above 2.4 GPa, the sample became polycrystalline and no further information could be extracted. Refinements of STAM-1 were carried out against $|F|^2$ using all data.[15] Because of the low completeness of the data-sets, all 1,2 and 1,3 distances on the monomethyl benzene-1,3,5-tricarboxylic acid linker were restrained to the values observed from our ambient temperature and pressure structure. All metal-ligand distances and angles, and all torsion angles were refined freely. Thermal and vibrational similarity restraints were applied to the organic linker. H-atoms attached to carbon were placed geometrically and not refined. The water H-atoms were initially found in a difference

map and refined with a bond length restraint to regularise its geometry (*r*O-H = 0.82(1) Å) with U[iso] set to 1.2 times U[eq] of the parent atom. On converging, all H-atoms were refined with riding constraints.

4.2.2.4 Compression study using Methanol

Upon loading STAM-1 in a DAC with MeOH to 0.2 GPa, a ligand exchange reaction was observed. This new form of STAM-1 is hereafter referred to as STAM-1_{MeOH}. The reaction involved exchange of methanol for water at the axial coordination site of the Cu^{II} dimer. The structure of STAM-1_{MeOH} was determined by starting from the ambient pressure coordinates of STAM-1 by Mohideen *et al*. The methyl group position was determined by a difference Fourier map. In order to ascertain whether STAM-1_{MeOH} was stable at room temperature, the same crystal was recovered to ambient pressure and temperature, and a single-crystal X-ray diffraction data set was then collected.

In a separate high-pressure study, another crystal of STAM-1 was loaded into a DAC with methanol to 0.5 GPa and high-pressure data were collected in approximately 0.9 GPa steps up to 5.7 GPa. Refinements of STAM-1_{MeOH} were carried out against $|F|^2$ using all data.[15] Because of the low completeness of the data-sets, all 1,2 and 1,3 distances on the monomethyl benzene-1,3,5-tricarboxylic acid linker and MeOH ligand were restrained to the values observed from our ambient temperature and pressure structure. All metal-ligand distances and angles, and all torsion angles were refined freely. Thermal and vibrational similarity restraints were applied to both the organic linker and MeOH ligand. H-atoms attached to carbon were placed geometrically and not refined. The H-atom attached to the oxygen atom were initially found in a difference map and refined with restraints on the bond length to regularise its geometry (O-H = 0.82 Å) with U[iso] set to 1.2 times U[eq] of the parent atom. On converging, all H-atoms were refined with riding constraints. Above 5.73 GPa, the crystal broke apart, becoming polycrystalline.

4.2.2.5 Software for Structure Analysis

Crystal structures were visualized using the programs DIAMOND[18] and MERCURY.[19] Void analyses carried out in MERCURY used the contact surface with a probe radius of 1.2 Å and an approximate grid spacing of 0.7 Å.

4.3 Results and Discussion

4.3.1 The structures of STAM-1 and STAM-1$_{MeOH}$

The paddle wheels in STAM-1 are connected through the monomethyl BTC ester linkers to form approximately triangular 'cups' (Figure 2a).[8] Because connectivity is lost through the carboxylate linker, which is esterified during the synthesis of STAM-1, the resulting framework forms interpenetrating layers (Figure 2b) that result in the formation of two types of pores, some lined by the ester groups (hydrophobic), and others lined by the axial water molecules (hydrophilic), as shown in Figure 3. There are two hydrophilic and one hydrophobic channel per unit cell, which run down the crystallographic *c*-axis (Figures 5 & 6).

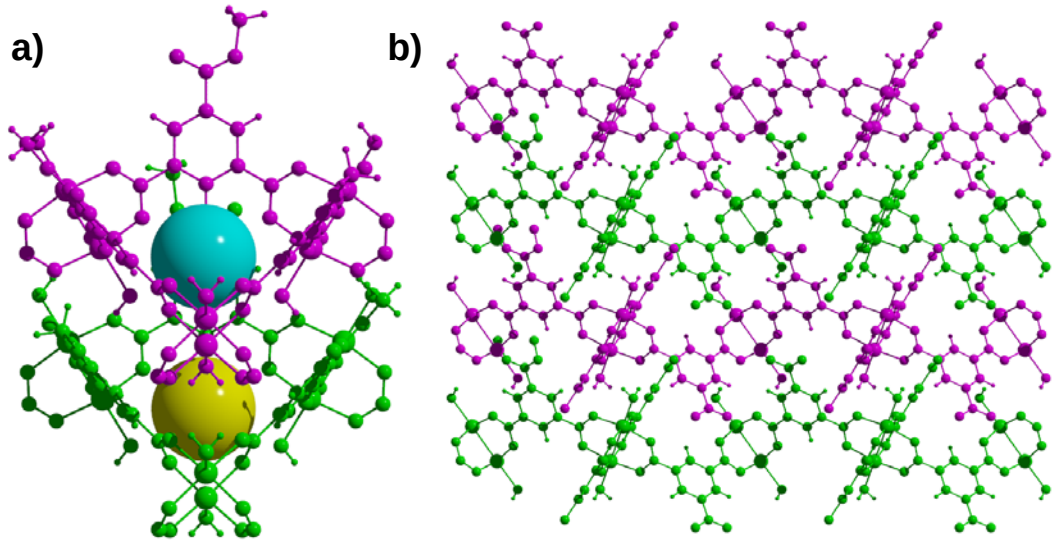

Figure 2. a) Two of the cup-like structural units found in STAM-1 stacked on top of one another. The green and yellow spheres represent the void space in the centre of each cup. **b)** View of STAM-1 parallel to crystallographic *b*-axis showing how the cups are arranged in such a way as to form interpenetrating layers.

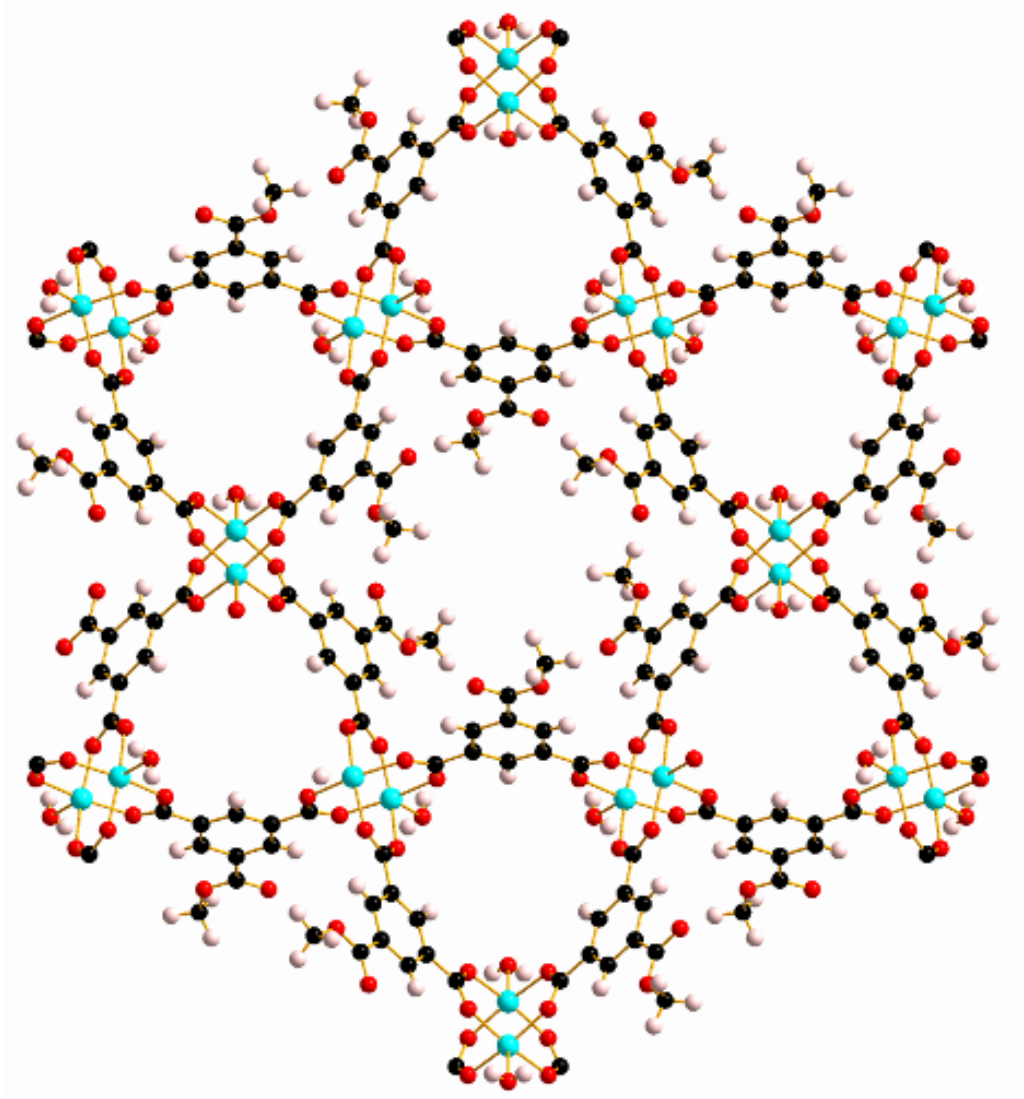

Figure 3. Representation of the as-synthesised STAM-1 structure viewed along the *c*-axis. The central large hydrophobic channel is surrounded by six smaller hydrophilic ones in a hexagonal arrangement. Colour scheme as in Figure 1.

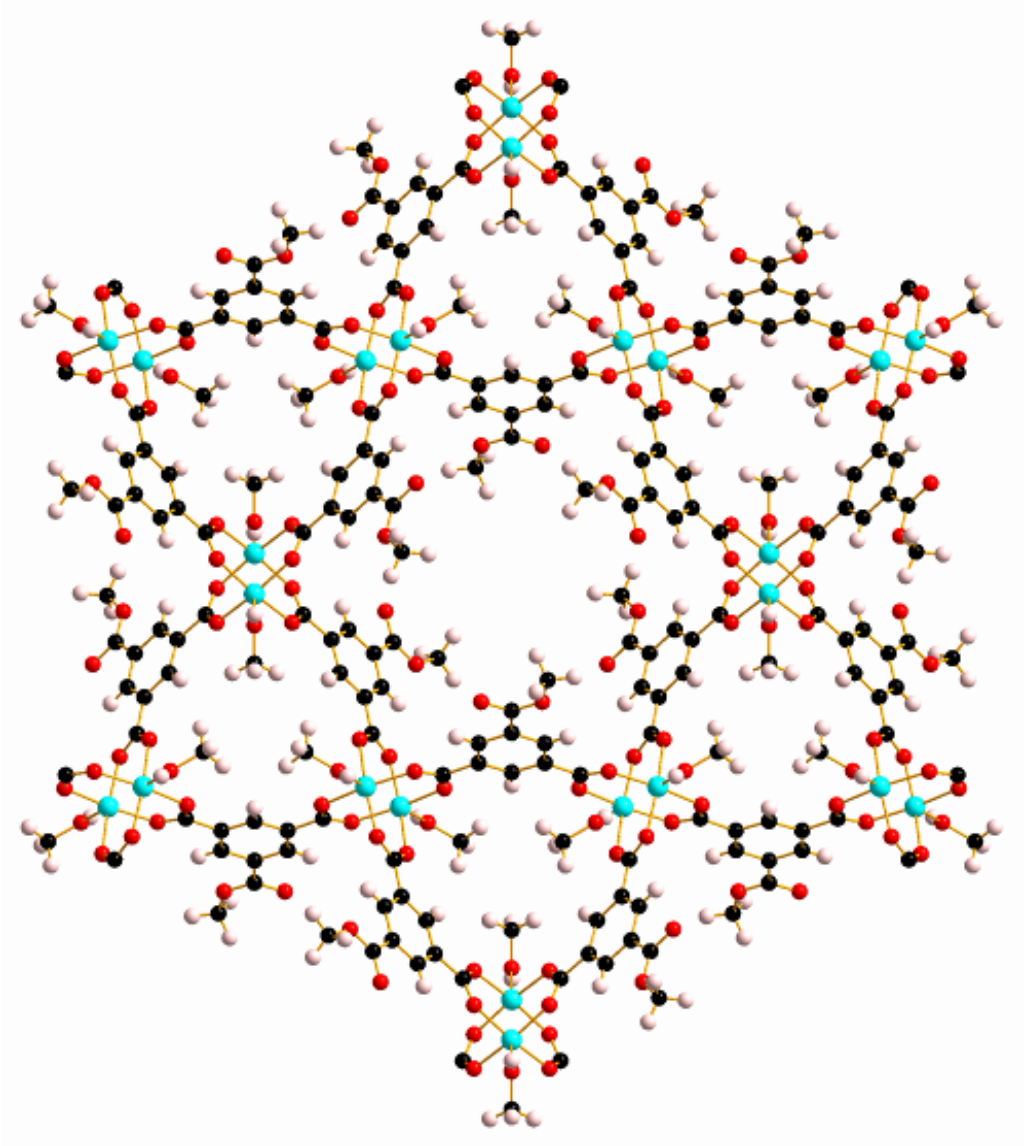

Figure 4. Representation of STAM-1_{MeOH} structure viewed along the *c*-axis. The six small (previously hydrophilic) pores surrounding the central channel are now seen to be decreased in size compared with STAM-1. The methanol substitution has also changed the chemical nature of these smaller pores. Colour scheme as in Figure 1.

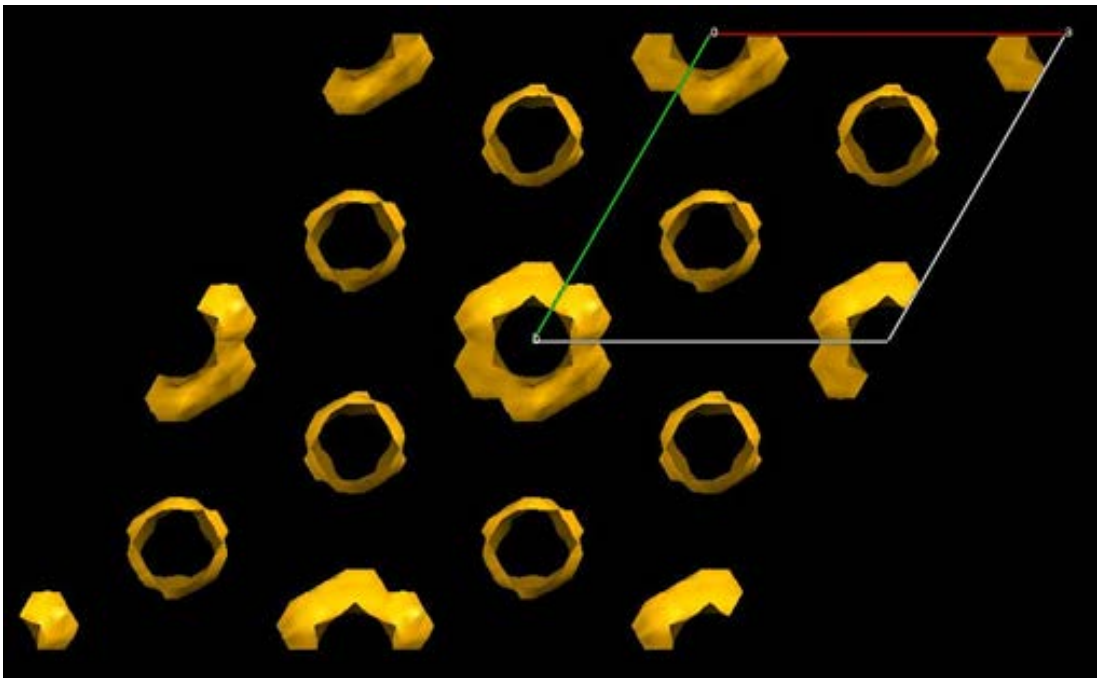

Figure 5. Void spaces of STAM-1 at ambient pressure and temperature. Six smaller hydrophilic channels surround every larger hydrophobic pore.

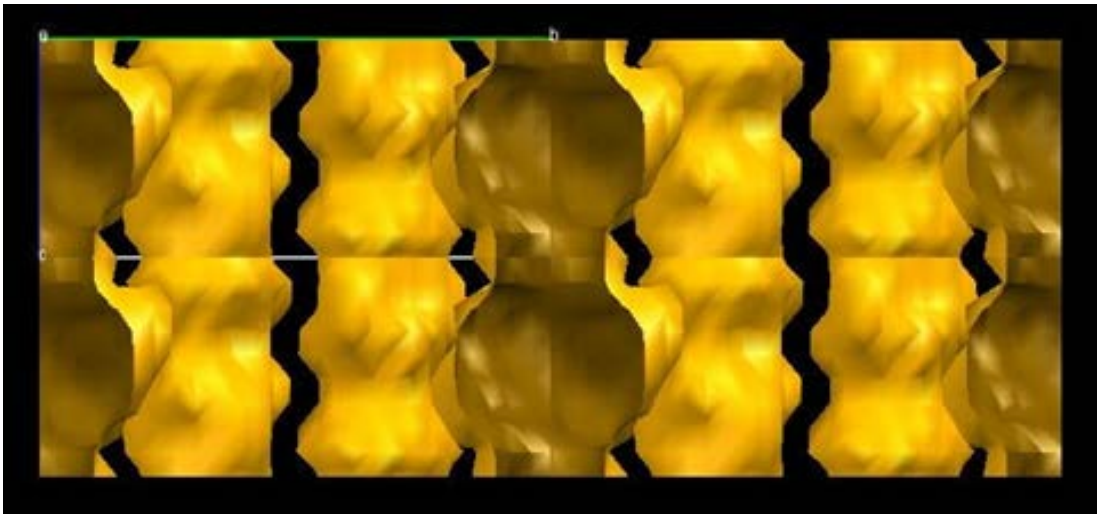

Figure 6. STAM-1 contact surface as calculated in MERCURY, viewed along the crystallographic *a*-axis. The hydrophobic pores are located in the centre and on the extreme left and right of the figure. The hydrophilic channels are located between the hydrophobic pores.

In this study, single-crystal X-ray diffraction data were collected on a crystal of STAM-1 at room temperature and ambient pressure. Under ambient temperature and pressure conditions, STAM-1 contains water molecules in the hydrophilic

channels which equates to three molecules of water per channel, per unit cell (Table 1, calculated using the *SQUEEZE* algorithm within PLATON).[14] The volume of both the hydrophobic and hydrophilic channels measures ≈200 and ≈140 $Å^3$ respectively. Notably, some residual electron density is observed in the larger hydrophobic channel, though the largest difference electron density in this channel measures only 2 electrons $Å^{-3}$, showing that the hydrophobic channels can be regarded as essentially empty. The same crystal was then loaded in a DAC, and surrounded with methanol as a hydrostatic liquid. Upon loading to 0.2 GPa, a single-crystal to single-crystal phase transition was observed, to a previously unknown form of STAM-1, which we hereafter refer to as STAM-1_{MeOH}. This transition entailed a ligand exchange of the coordinated water at the axial position of the Cu^{II} paddle-wheel for the methanol that was used as the pressure-transmitting medium (Figure 1). The ligand exchange reaction was accompanied by an increase in unit cell volume (45.0(6) $Å^3$), with the *a/b*- and *c*-axes expanding by 0.34 and 0.30% respectively.

On undergoing the transition, a rather marked change in the pore volume and content was observed, with the hydrophobic pores increasing by 74 $Å^3$, accompanied by an increase in solvent content equating to inclusion of two methanol molecules per hydrophobic pore (Table 1). Contrary to this, the hydrophilic channels decrease in both size and content. One reason for this could be that exchanging the water ligand for methanol increases the hydrophobicity of the previously hydrophilic channels, as the methyl groups on the methanol ligand protrude into the cavity (Figure 4). The effect of pressure on the hydrophobic channels however counteracts this argument, as the hydrophobic nature of the pores is easily overcome by the onset of pressure. A more realistic argument is that the ligand exchange reaction, which results in significantly decreasing the size of the hydrophilic channels forces the included water molecules out of these channels (Figures 7 & 8).

Table 1. Crystallographic and pore data for STAM-1 as a function of pressure. The * denotes the recovered phase of STAM-1_{MeOH} on removing from the DAC.

Pressure (GPa)	**Unit cell volume (Å³)**	**Hydrophobic pore**		**Hydrophilic pore**	
		Volume (Å^3)	**Electron count**	**Volume (Å^3)**	**Electron count**
0.0	2058.2(4)	209	14	142	33
0.2	2103.2(5)	283	51	46	11
0.0*	2083.69(6)	215	14	48	2

In order to evaluate whether STAM-1_{MeOH} was stable under ambient conditions, the pressure was decreased and the same crystal was then recovered from the DAC. Single crystal X-ray diffraction data were then collected under ambient temperature and pressure conditions and the recovered sample was confirmed as the exchanged STAM-1_{MeOH} structure.

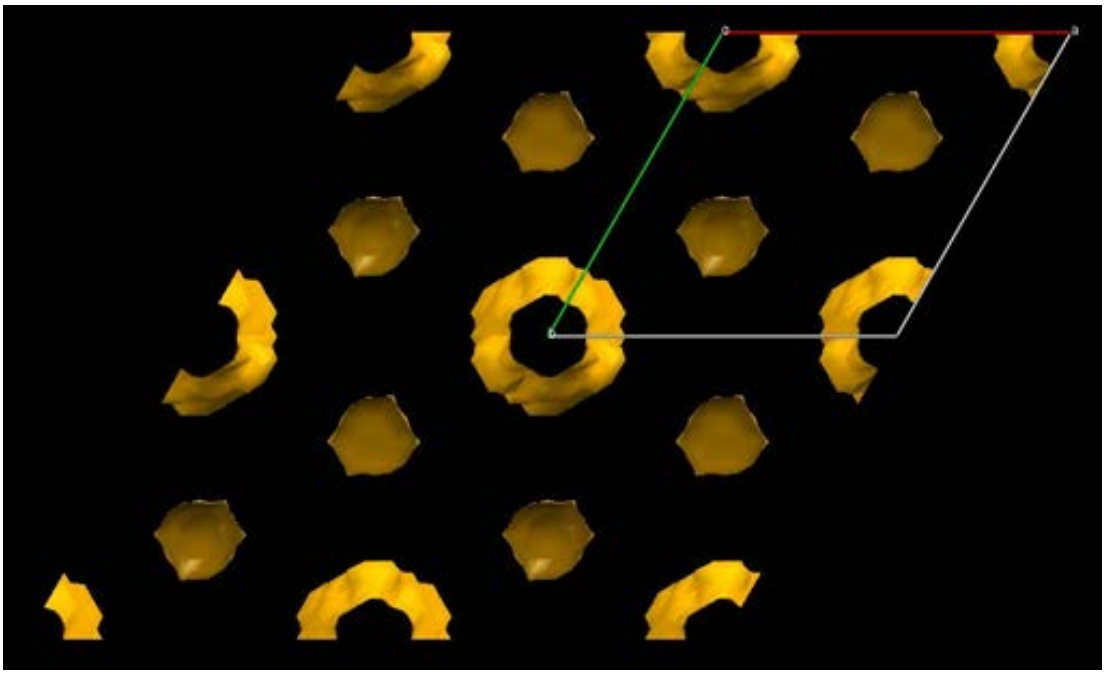

Figure 7. STAM-1_{MeOH} contact surface as calculated in MERCURY. The previously hydrophilic pores are now effectively closed.

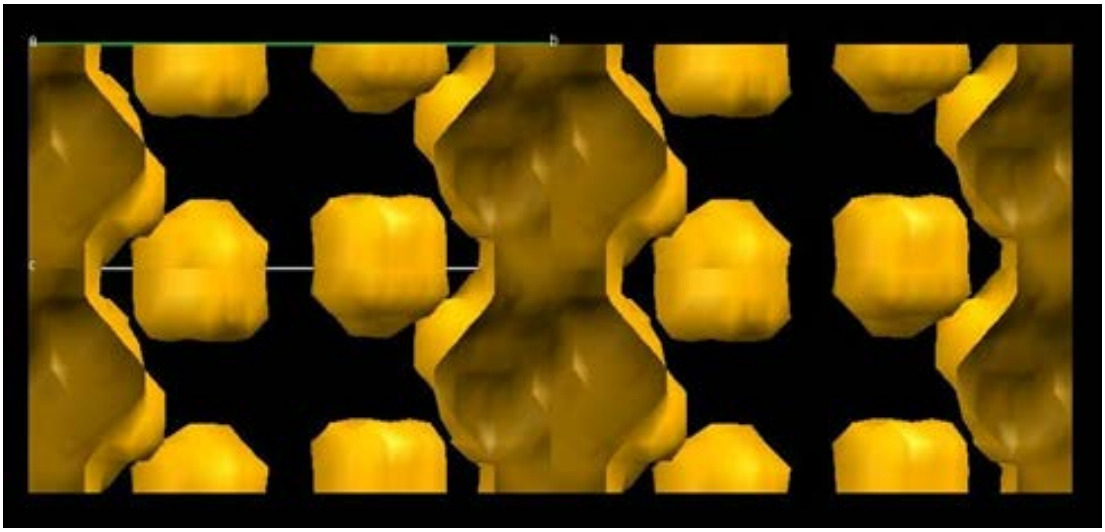

Figure 8. STAM-1_{MeOH} contact surface as calculated in MERCURY, viewed along the crystallographic *a*-axis. The hydrophobic pores can be seen centre, left and right. The previously hydrophilic channels are now seen as discrete pores with no permeability between them. Each spherical pore contains a disordered methanol molecule.

STAM-1_{MeOH} under ambient conditions has a volume ≈ 25 Å³ larger than that of native STAM-1, though the density of the frameworks (ignoring included solvent) measures 1.482 and 1.519 gcm^{-3} for STAM-1 and STAM-1_{MeOH} respectively. This could indicate the exchanged sample is more stable, though further investigation is needed to confirm this. On recovering STAM-1_{MeOH}, the hydrophobic pores decrease in size, and are comparable to STAM-1 prior to application of pressure (Table 1). This coincides with a reduction in the pore content, as the included methanol molecules observed at 0.2 GPa, come out of the hydrophobic pores on decreasing pressure, confirming that inclusion of methanol guest molecules is stabilised at high-pressure. The volume of the hydrophilic pores remains unchanged on decreasing pressure, though the pore content at ambient pressure is almost negligible. We propose that this is caused by the greater hydrophobicity of the pores produced by the methyl groups on the exchanged methanol ligand, which could be counteracted at 0.2 GPa, but not at ambient pressure. The coordination environment around the Cu-centre is very similar in both STAM-1 and STAM-1_{MeOH}, though the axial Cu-O bond, and Cu…Cu distance do decrease by 0.015(4) and 0.012(1) Å respectively on exchange with methanol. One main difference between the two structures is that, on undergoing the ligand exchange reaction, the hydrophilic channels are essentially blocked as the opening to these channels decreases from 1.79 to 0.49 Å (Figures 3 to 8).[20] The ligand exchange reaction therefore turns the hydrophilic channels into discrete pores, measuring ≈50 Å³.

4.3.2 Compression studies

In order to discover whether larger alcohols could undergo a similar exchange reaction and to elucidate the stability of the methanol exchanged sample, further high-pressure experiments were carried out in which another single crystal of STAM-1 was loaded with IPA, and a separate sample loaded with methanol as a pressure transmitting medium.

4.3.2.1 STAM-1 compression in IPA

On loading a crystal of STAM-1 in IPA to 0.5 GPa, no exchange reaction was observed. High-pressure data were then collected from 0.5 to 2.4 GPa. Increasing pressure above 2.4 GPa resulted in the sample becoming polycrystalline, and no further information could be extracted. Structural data could only be reliably determined to 0.9 GPa for compression data in IPA, above this pressure only unit cell dimensions could be determined.

In response to the increase in pressure from ambient to 0.5 GPa, the unit cell volume of STAM-1 decreased (Figure 9). Increasing pressure to 0.9 and then 1.5 GPa resulted in further near-linear reduction in unit cell volume to 1933.5(16) $Å^3$. A large discontinuity is then observed between 1.5 and 2.4 GPa with a 13% decrease in volume. Unfortunately, as structural data could only be reliably determined to 0.9 GPa we do not have an explanation for this dramatic change in compressibility.

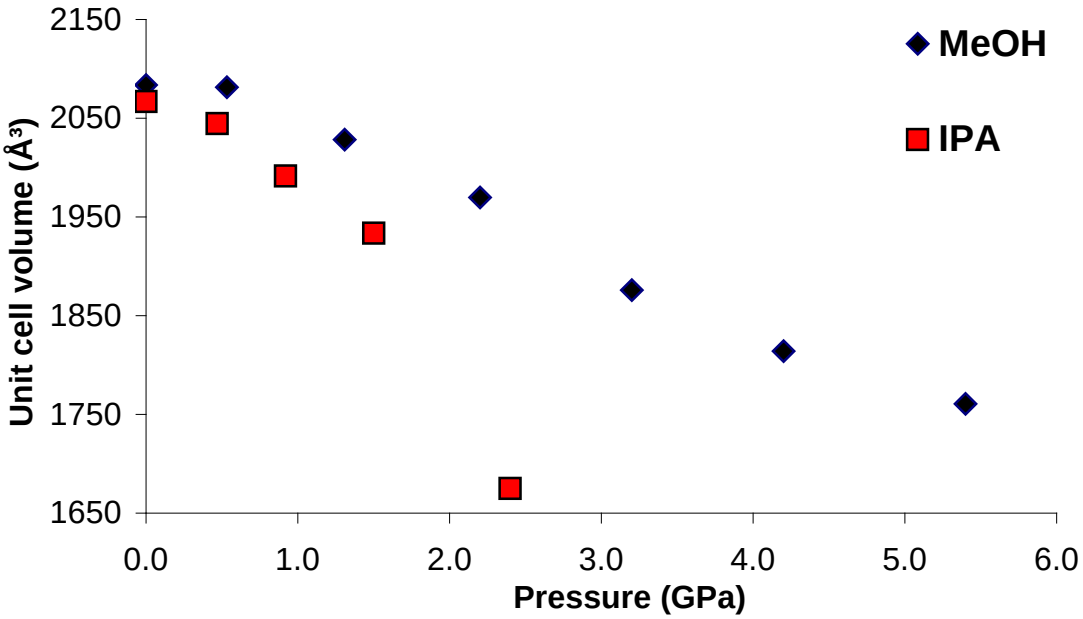

Figure 9. Unit cell volume of STAM-1 in IPA (red blocks) and STAM-1_{MeOH} in methanol (blue diamonds) as a function of pressure.

From inspection of the unit cell axes response to applied pressure (Figures 10 & 11), it can be seen that during this marked changed in compressive behavior there was a contraction of all three crystallographic axes but the contraction is not

isotropic. The *a/b*-axes contract by approximately 4% between 1.5 and 2.4 GPa, while the *c*-axis shortens by ~7.6%. Although we cannot attribute this to any observed structural change, the layers formed in STAM-1 stack approximately perpendicular to the c-axis direction. This would suggest that the inter-layer interaction is by far the most compressible feature of STAM-1, with the inter-layer distance decreasing by 0.499(13) Å to accommodate the increase in pressure.

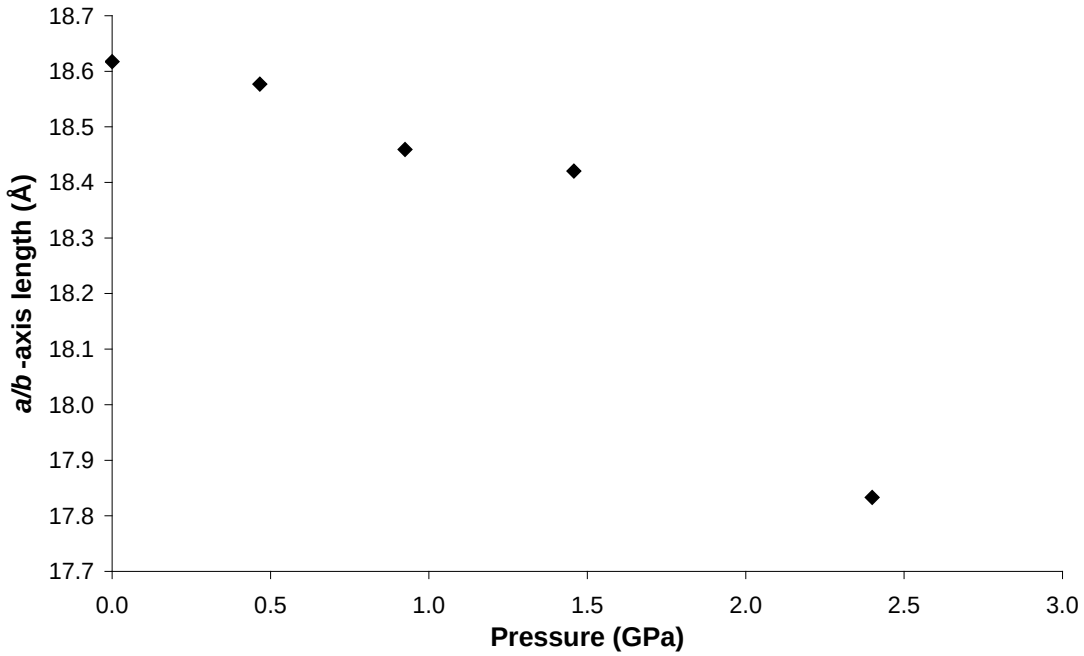

Figure 10. Unit cell *a*/*b* axes length of STAM-1 in isopropyl alcohol as a function of pressure.

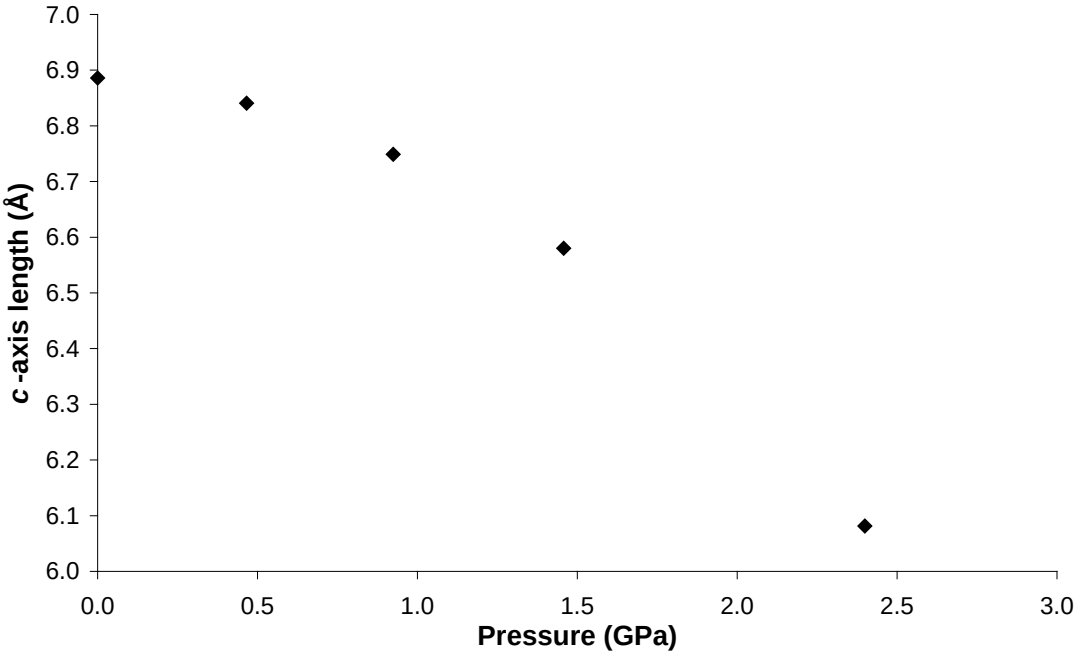

Figure 11. Unit cell *c*-axis length of STAM-1 in isopropyl alcohol as a function of pressure.

Increasing the pressure on STAM-1 in IPA to 0.5 GPa, results in an uptake of hydrostatic liquid similar to that observed with methanol (though no ligand exchange is observed), with an increase in electron density observed in the hydrophobic channels (Table 2). The application of pressure here would therefore seem to override any energy penalty for IPA molecules entering the hydrophobic channels. On increasing pressure further, the IPA content of the hydrophobic channels continues to increase, with two molecules of IPA occupying the hydrophobic channels at 0.9 GPa. The content of the hydrophilic channels appears to vary somewhat across this pressure range, both decreasing, and then increasing again on increasing pressure to 0.5, and then further to 0.9 GPa. We suspect, however that this is due to the mobility of water molecules already present in these pores, as the pore size (≈50 Å³) is too small to accommodate IPA, which has a molecular volume of ≈ 60 Å³ at ambient pressure.[20] This argument is also supported by the fact that no exchange reaction takes place which would necessitate the inclusion of IPA in these pores.

Table 2. Pore volume and content statistics of STAM-1 in isopropyl alcohol as a function of pressure.

Pressure (GPa)	Hydrophobic pore		Hydrophilic pore	
	Volume (Å^3)	Electron count	Volume (Å^3)	Electron count
0.0	209	14	142	33
0.5	201	64	140	14
0.9	176	94	133	42

4.3.2.2 STAM-1 compression in methanol

On loading to 0.5 GPa in methanol, the ligand exchange reaction occurred again and high-pressure data were then collected from 0.5 to 5.7 GPa, above which the sample became polycrystalline and no further information could be extracted. Structural data could only be reliably determined to 1.3 GPa, with only unit cell dimensions reported above this pressure.

Comparing the compressibility of STAM-1 with STAM-1$_{MeOH}$, the greater stability of STAM-1$_{MeOH}$ to pressure is apparent from its greater rigidity, and the fact that STAM-1$_{MeOH}$ remains stable to much higher pressures (Figure 9). This is unsurprising as STAM-1$_{MeOH}$ is a much denser framework.

In STAM-1$_{MeOH}$, increasing pressure above 0.5 GPa results in more methanol being squeezed into the hydrophobic pores. A clear transition is observed on increasing pressure from 0.5 to 1.3 GPa, with the solvent content increasing from 55 to 151 e$^-$ per hydrophobic pore, equating to 7 methanol molecules (Table 3). In a separate compression study of ZIF-8 (Zn(MeIM)$_2$, MeIM = 2-methylimidazolate), a similar jump in pore content was observed on increasing pressure from 0.96 to 1.47 GPa, though the sudden increase in pore content here was accompanied by a rotation of the MeIM rings, which increased the available pore volume. No significant structural changes were observed in the framework of STAM-1$_{MeOH}$, though this is unsurprising, as the monoesterified BTC ligands have much fewer degrees of freedom compared to the MeIm ligands in ZIF-8.[21]

Table 3. Pore volume and content statistics of STAM-1_{MeOH} in methanol as a function of pressure.

Pressure (GPa)	Hydrophobic pore		Hydrophilic pore	
	Volume (Å^3)	Electron count	Volume (Å^3)	Electron count
0.0	215	14	48	2
0.5	256	55	50	22
1.3	265	159	43	21

The significant uptake of methanol molecules into STAM-1_{MeOH} explains the greater rigidity of the framework over the native STAM-1 structure, as inclusion of solvent makes the framework much harder. Similar behavior has been observed before in the compression behavior of Cu-btc, where this 'solvent filling' regime resulted in a much higher bulk modulus of the sample.[22] This behavior appears to be a consistent feature of MOFs put under extreme pressure, with the compressibility changing by several orders of magnitude depending on whether guest inclusion occurs, the nature of the guest species and how the pressure is applied. In MOF-5, amorphisation can occur either on grinding the sample at 3.5 MPa,[23] or on applying hydrostatic pressure above 3.2 GPa.[24] More recently, in a high-pressure study of the flexible framework NH_2-MIL-53-(In), amorphisation does not take place until >20 GPa.[25]

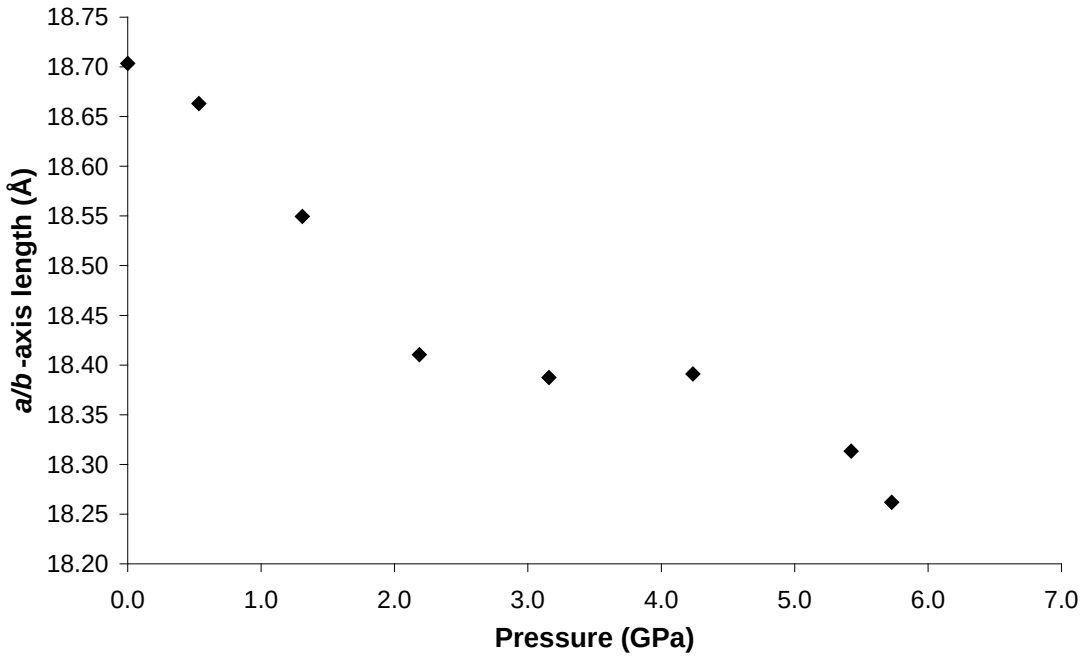

Figure 12. Unit cell *a*/*b* axes length of STAM-1_{MeOH} in methanol as a function of pressure.

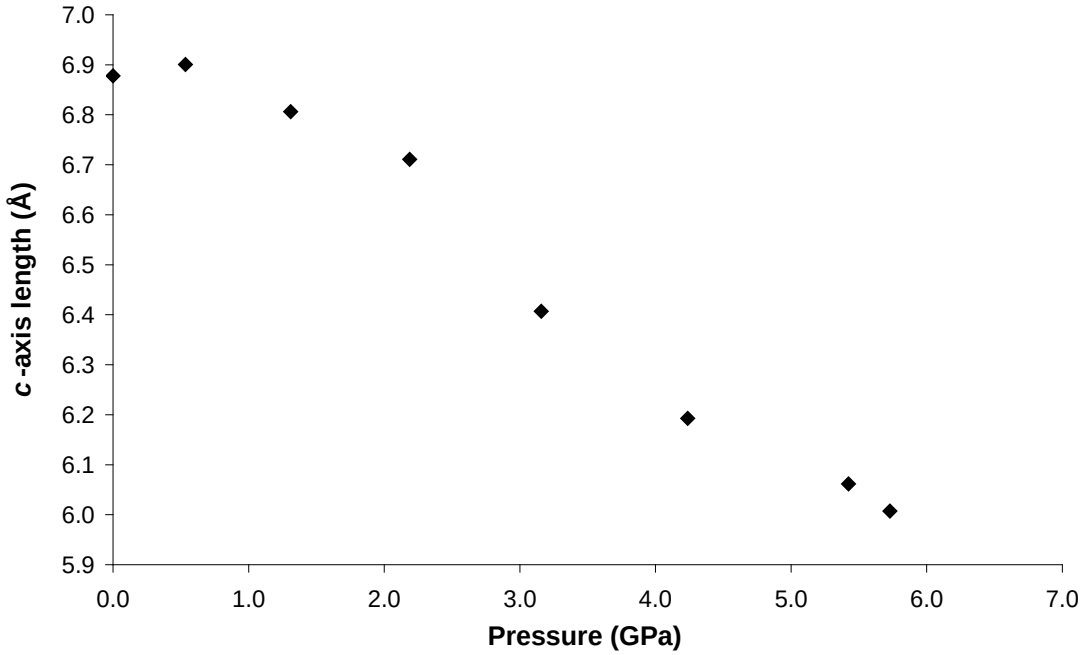

Figure 13. Unit cell *c*-axis length of STAM-1_{MeOH} in methanol as a function of pressure.

Between 1.3 and 4.2 GPa, a clear plateau is reached in the compressibility of the *a*/*b*-axes, which actually *increase* slightly on increasing pressure from 3.2 to 4.2

GPa (Figure 12), though the changes here are marginal. Unfortunately, this could not be correlated to any changes in the structure or pore content reliably, as the resolution of the data deteriorated above this pressure. On increasing pressure above 4.2 GPa, the *a/b*-axes show a rapid decrease in length, and could indicate that the hydrophobic pores empty above this pressure. Very similar behavior has been observed in the compressibility of the MOFs MOF-5 [$Zn_4O(BDC)_3$, BDC = 1,4-benzenedicarboxylate] and Cu-btc, where a 'gating' pressure was reached which resulted in a decrease in pore content at higher pressures. In MOF-5 and Cu-btc this was achieved above 0.8 and 3.9 GPa respectively. Further investigation will be required to ascertain whether we are observing the same effect here.

4.4 Conclusions

In summary, we have shown that by applying pressure to STAM-1 we can force methanol to enter the pores causing the sample to undergo a ligand exchange reaction. This new phase, referred to as STAM-1_{MeOH}, can be recovered at ambient pressure, and results in a significant change in the pore size and shape. In particular, hydrophilic channels in the native STAM-1 framework are now converted into discrete pores having a much smaller volume. On applying pressure to STAM-1 using IPA (a much larger alcohol) as a hydrostatic liquid, no ligand exchange reaction occurs. The compressibility behaviour of STAM-1_{MeOH} in methanol, and STAM-1 in IPA is somewhat similar, in that uptake of the alcohol hydrostatic medium into the hydrophobic pores is observed in both cases, showing that high pressures can override the energy penalty for this process. No uptake of hydrostatic liquid is observed in the hydrophilic channels in STAM-1_{MeOH} above 0.5 GPa as the channels are converted to discrete pores, while the larger IPA molecules are too large to enter the hydrophilic channels in STAM-1. These high-pressure experiments also demonstrate the greater compressibility of STAM-1 over STAM-1_{MeOH}, as more solvent molecules can be forced into the pores of STAM-1_{MeOH}, making the framework much harder and therefore more resilient to compression.

4.5 References

1 J. S. Seo, D. Whang, H. Lee, S. I. Jun, J. Oh, Y. J. Jeon and K. Kim, *Nature*, 2000, **404**, 982.

2 Z. Wang and S. M. Cohen, *Chem. Soc. Rev.*, 2009, **38**, 1315.

3 J. S. Costa, P. Gamez, C. A. Black, O. Roubeau, S. J. Teat and J. Reedijk, *Eur. J. Inorg. Chem.*, 2008, **2008**, 1551.

4 T. Gadzikwa, O. K. Farha, K. L. Mulfort, J. T. Hupp and S. T. Nguyen, *Chem. Commun.*, 2009, 3720.

5 S. S.-Y. Chui, S. M.-F. Lo, J. P. H. Charmant, A. G. Orpen and I. D. Williams, *Science*, 1999, **283**, 1148.

6 Y.-S. Bae, O. K. Farha, J. T. Hupp and R. Q. Snurr, *J. Mater. Chem.*, 2009, **19**, 2131.

7 M. Banerjee, S. Das, M. Yoon, H. J. Choi, M. H. Hyun, S. M. Park, G. Seo and K. Kim, *J. Amer. Chem. Soc.*, 2009, **131**, 7524.

8 M. I. H. Mohideen, B. Xiao, P. S. Wheatley, A. C. McKinlay, Y. Li, A. M. Z. Slawin, D. W. Aldous, N. F. Cessford, T. Düren, X. Zhao, R. Gill, K. M. Thomas, J. M. Griffin, S. E. Ashbrook and R. E. Morris, *Nat Chem*, 2011, **3**, 304.

9 S. A. Moggach, D. R. Allan, S. Parsons and J. E. Warren, *J. Appl. Crystallogr.*, 2008, **41**, 249.

10 G. J. Piermarini, S. Block, J. D. Barnett and R. A. Forman, *J. Appl. Physics*, 1975, **46**, 2774.

11 Bruker-Nonius, Bruker-AXS, Madison, Wisconsin, USA, 2006.

12 G. M. Sheldrick, *SADABS Version 2008-1*, 2008.

13 P. W. Betteridge, J. R. Carruthers, R. I. Cooper, K. Prout and D. J. Watkin, *J. Appl. Crystallogr.*, 2003, **36**, 1487.

14 A. L. Spek, Utrecht University, Utrecht, The Netherlands, 2004.

15 P. W. Betteridge, J. R. Carruthers, R. I. Cooper, K. Prout and D. J. Watkin, *J. Appl. Crystallogr.* , 2003, **36**, 1487.

16 A. Dawson, D. R. Allan, S. Parsons and M. Ruf, *J. Appl. Crystallogr.*, 2004, **37**, 410.

17 S. Parsons, The University of Edinburgh, Edinburgh, United Kingdom, 2004.

18 K. Brandenburg and H. Putz, Crystal Impact, Bonn, Germany, 2005.

19 C. F. Macrae, I. J. Bruno, J. A. Chisholm, P. R. Edgington, P. McCabe, E. Pidcock, L. Rodriguez-Monge, R. Taylor, J. van de Streek and P. A. Wood, *J. Appl. Crystallogr.*, 2008, **41**, 466.

20 O. V. Dolomanov, L. J. Bourhis, R. J. Gildea, J. A. K. Howard and H. Puschmann, *J. Appl. Crystallogr.*, 2009, **42**, 339.

21 S. A. Moggach, T. D. Bennett and A. K. Cheetham, *Angew. Chem., Int. Ed.*, 2009, **48**, 7087.

22 A. J. Graham, J.-C. Tan, D. R. Allan and S. A. Moggach, *Chem. Commun.*, 2012, **48**, 1535; K. W. Chapman, G. J. Halder and P. J. Chupas, *J. Am. Chem. Soc.*, 2008, **130**, 10524.

23 Y. H. Hu and L. Zhang, *Phys. Rev. B: Condens. Matter Mater. Phys.*, 2010, **81**, 1741031.

24 A. J. Graham, D. R. Allan, A. Muszkiewicz, C. A. Morrison and S. A. Moggach, *Angew. Chem., Int. Ed.*, 2011, **50**, 11138.

25 P. Serra-Crespo, E. Stavitski, F. Kapteijn and J. Gascon, *RSC Advances*, 2012, **2**, 5051.

Chapter 5

The effect of pressure on ‘breathing’ mechanisms in Zeolitic Imidazolate Frameworks (ZIFs)

5.1 Introduction

ZIF-8 crystallises in the cubic space group *I*-43*m*. It consists of Zn^{II} ions tetrahedrally coordinated by four nitrogen atoms from bridging imidazolates to yield a three dimensional network with an expanded sodalite structure (Figure 1). The five-membered imidazolate ring serves as the bridging unit between the Zn^{II} centres and imparts a Zn-Imidazole-Zn angle of ≈ 145° via the coordinating N atoms. An important structural feature of this material is the presence of a large central pore with a volume of ≈ 2500 $Å^3$ (≈ 50% of the unit cell volume). At ambient temperature and pressure, these large central pores are linked by six-membered-ring apertures which form channels running along the [111] direction (Figure 1b). There are also smaller four-membered-ring windows, which are lined by R-imidazolate linkers (Figure 1). The imidazolate linkers are oriented in an alternating up-down arrangement resulting in opposing linkers being oriented in the same direction (Figure 2). At ambient temperature and pressure, the imidazole ligands are tilted with respect to the cell axes resulting in the CH_3-groups pointing towards each other, decreasing the size of the opening to the channels (Figure 3).

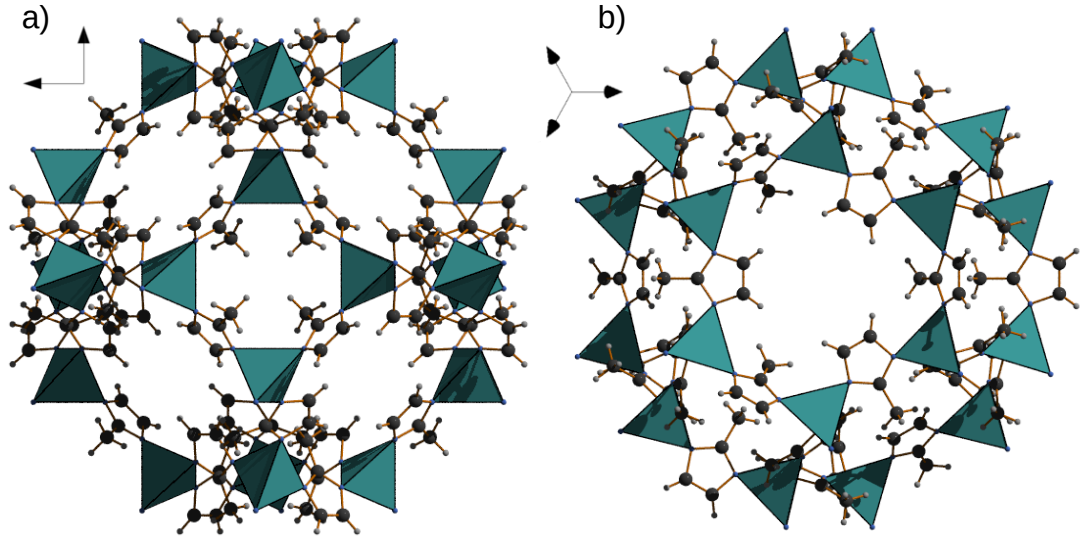

Figure 1. Packing diagram of ZIF-8 at ambient pressure viewed along a) the [100] direction showing the four-membered-ring windows and b) the [111] direction, along which run the channels that link the large central pores of the framework.

Here we present an extension to the initial compression study of ZIF-8 in a methanol:ethanol hydrostatic liquid, and describe the effect of pressure and guest uptake on ZIF-8 in a 1:1 by volume pentane:isopentane mixture and Fluorinert. We have also carried out a geometry optimization and a series of single-point energy calculations in order to probe the energy surface of imidazolate ring rotation.

5.2 Experimental

5.2.1 Synthetic procedure and crystal growth

Single-crystal samples of ZIF-8 were synthesised by and very gratefully received from Dr Thomas Bennett (University of Cambridge). Below is the procedure followed for the synthesis of these samples:

ZIF-8 was prepared following the method described by Huang *et al.*[1] A solid mixture of zinc(II) nitrate hexahydrate (0.525 g, 1.76×10^4 mol) and 2-methylimidazole (MeIM; 0.015 g, 1.83×10^4 mol) was dissolved in DMF (9 mL) in a 12 mL Teflon-capped vial. The vial was heated at a rate of $200^{\circ}Ch^{-1}$ to $130^{\circ}C$, held at this temperature for 24 h, and then cooled at a rate of $5^{\circ}Ch^{-1}$ to room temperature. Colourless polyhedral crystals were filtered from the reaction mixture, washed with chloroform (3×5 mL), and dried in air (30 min).

5.2.2 High-pressure single-crystal X-ray diffraction experiments

5.2.2.1 General procedures

High-pressure experiments were carried out using a Merrill–Bassett diamond–anvil cell (DAC) with a half-opening angle of 40°. The DAC was equipped with 600 μm culets and a tungsten gasket[2]. A small ruby chip was also loaded into the cell as a pressure calibrant, with the ruby-fluorescence method being used to measure the pressure.[3]

5.2.2.2 Data Collection, Reduction and Refinement

5.2.2.2.1 ZIF-8 compression using pentane:isopentane

Ambient temperature and pressure single-crystal X-ray diffraction data were collected on a block-shaped crystal of ZIF-8 (0.14 x 0.13 x 0.08 mm) on a Bruker

APEXII diffractometer with graphite-monochromated Mo *K*α radiation (λ = 0.71073 Å). The crystal was loaded into a DAC with a 1:1 by volume mixture of pentane:isopentane. Ambient-temperature, high-pressure diffraction data were collected on beamline I19 at the Diamond Light Source with double-crystal monochromated synchrotron radiation (λ = 0.4859 Å). High-pressure data collection and processing procedures were based on those described by Dawson *et al*[4]. Pressure was increased in approximately 0.5 GPa steps from 0.16 to 2.96 GPa. X-ray diffraction data were collected at each pressure stage. Above 2.96 GPa, the sample became polycrystalline and structural data could not be extracted.

Integrations were carried out using the program SAINT[5]. Absorption corrections were applied in a two-stage procedure with the programs SHADE[6] and SADABS[7] for high-pressure data sets, and with SADABS alone for the ambient-pressure data. Refinements were carried out against $|F|^2$ using all data using the software CRYSTALS[8]. Pore volume and solvent content were calculated using the *SQUEEZE* algorithm within PLATON[9]. The starting structure for refinement was taken from the ZIF-8 structure deposited in the CSD (refcode VELVOY). During refinement, all 1,2 and 1,3 distances were restrained to the values observed from our ambient pressure values for the 2-methylimidazolate ligand. Metal to ligand bond distances and angles were allowed to refine freely. All non-hydrogen atoms were refined anisotropically with thermal similarity and vibrational restraints applied to all non-hydrogen atoms except Zn. A planar restraint was also applied to the imidazole ring.

5.2.2.2.2 ZIF-8 compression using Fluorinert FC-77

Ambient-pressure and temperature single-crystal X-ray diffraction data were collected on an APEXII diffractometer on a crystal of ZIF-8 (0.20 x 0.20 x 0.10 mm). The same crystal was then loaded into a DAC with Fluorinert FC-77 as the pressure transmitting medium. Further data was collected at 0.35, 0.74 and 1.41 GPa. Data collection, integration, processing and crystallographic refinements and restraints followed the procedure outlined above (section 5.2.2.2.1). A sharp decrease in resolution of the data was observed at 1.41 GPa, as a result, only unit cell dimensions could be determined at this pressure.

5.2.3 Computational work

All calculations were performed using the CASTEP (version 5.0) simulation package.[10] Starting coordinates for ZIF-8 were taken from the ambient pressure, 4 K neutron powder data from Wu *et al.*.[11] The Hamiltonian operator was approximated using the Perdew-Burke-Ernzerhof (PBE)[12] exchange-correlation functional, with the molecular wavefunction description provided by 'on-the-fly' pseudopotentials and a plane wave basis set operating at 500 eV, which gave convergence to within 4 meV per atom

The geometry optimisation calculations were run without any symmetry constraints, thus allowing for an independent variation of both the atomic positions and the primitive cell parameters. The potential energy surface was searched for energy minima by means of the Broyden-Fletcher-Goldfarb-Shanno (BFGS) algorithm. Structures were considered to be optimised when the energy per atom, maximum force, maximum stress, and maximum atomic displacement converged to the values of 0.02 meV/atom, 0.05 eV/Å, 0.1 GPa, and 0.002 Å, respectively. Once the first, ambient pressure, model was optimised, an external hydrostatic pressure of 5 GPa was applied and the system re-optimised.

Starting from the geometry optimized structure a series of single-point energy calculations were carried out as a function of the imidazolate rotation angle. A vector was created between the N atoms of the imidazolate ring around which the rotation was incremented (Figure 2). The rotation was implemented in a positive direction in 5° steps up to 50° and then 10° steps up to 90°. The negative rotation was incremented in 5° steps to -10° and then 10° steps to -90°. For each rotation angle, a single-point energy calculation was carried out without the framework being able to minimize, thus the energies taken from these are relative rather than absolute.

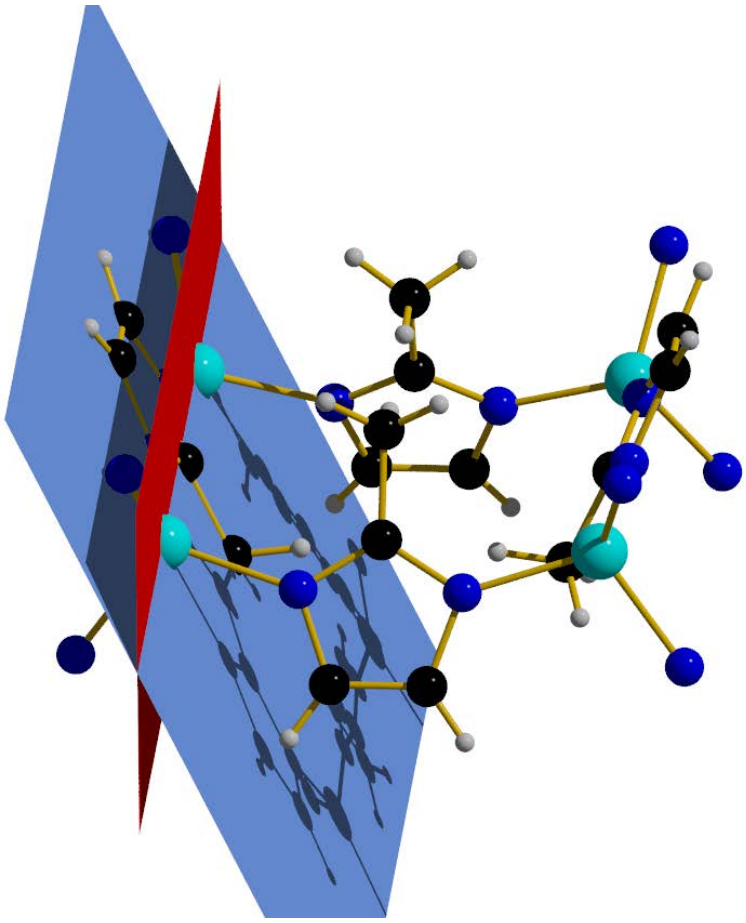

Figure 2. Representation of the four-membered window between the large central pores of ZIF-8 at ambient temperature and pressure. The rotation angle is taken as the angle between the (110) plane (red plane) and the mean imidazolate ring plane as determined in MERCURY CSD 3.0.1[13] (blue plane). The ambient pressure structure (shown above) has a value of 25.7°, while the high pressure structure determined by Moggach *et al.* gave a rotation angle of 0°, Key: Zn, turquoise; N, blue; C, black; H, grey.

5.3 Results and Discussion

5.3.1 Compression of ZIF-8 in pentane:isopentane

In a previous high-pressure study of ZIF-8 using MeOH:EtOH as a hydrostatic liquid, initial application of pressure to 0.18 GPa resulted in the MeOH and EtOH molecules entering the pores (equivalent to 4 MeOH molecules), causing the framework to expand by 99.1(8) $Å^3$ (2%) (Figure 4). On increasing pressure further to 0.52 GPa, the electron count continued to increase in the pores (equating to a

further 5 molecules of MeOH), while the volume decreased in comparison to the initial expansion. This continued until at 1.47 GPa the sample underwent a phase transition, which resulted in both an *increase* in volume (by 81.3(9) Å^3), on increasing pressure and a twisting of the MIm groups (Figure 3).

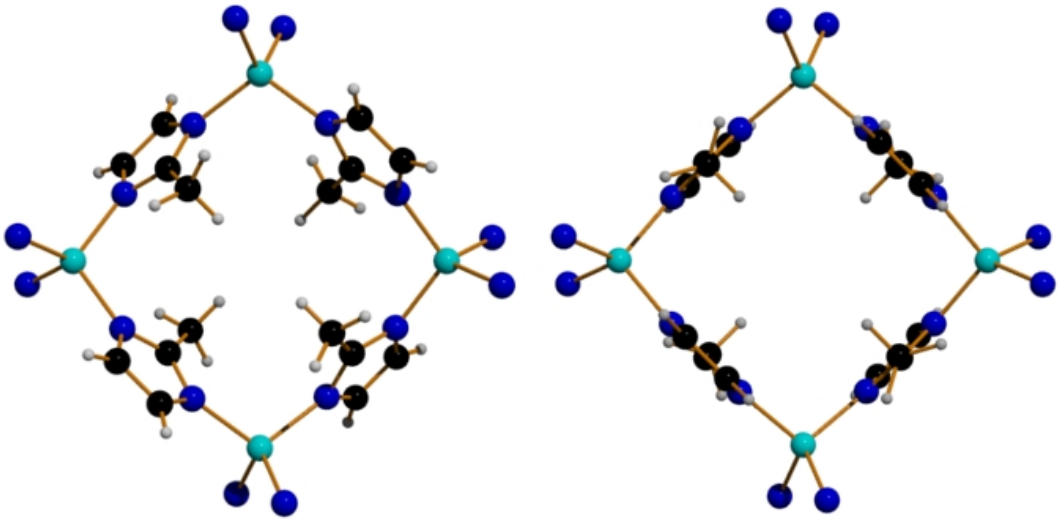

Figure 3. View parallel to the *b*-axis of the four-membered window of ZIF-8 in methanol:ethanol at ambient pressure (left) and at 1.48 GPa (right).

In this study, the effect of pressure using a 1:1 mixture of pentane:isopentane as a hydrostatic liquid has been investigated. Under ambient temperature and pressure, ZIF-8 contains some residual MeOH molecules which could not be fully evacuated from the pores, and equates to 10 MeOH molecules per unit cell. On increasing pressure to 0.16 GPa, the unit cell volume increased by 41.775(3) Å^3 (0.85%) (Figure 4), accompanied by a slight elongation of the Zn-N coordination bonds by 0.018(6) Å (Figure 6), though the increase here is only marginal (3.09σ). This lattice swelling is almost identical to that observed in the compression study using MeOH:EtOH, and indicates that the pores are large enough to accommodate inclusion of pentane/isopentane molecules, though the porous expansion on uptake of pentane:isopentane was less than in MeOH:EtOH.

Increasing the pressure further to 0.85 GPa yielded a further increase in unit cell volume, though the change here is not statistically significant, while the pore content remains essentially unchanged (Figure 5). On increasing pressure to 1.10

GPa, a sudden drop in pore content is observed, resulting in the equivalent of 12 pentane molecules being pushed out of the unit cell, with the unit cell volume, pore volume and Zn-N bond lengths all compressing by 14.9(12) Å^3, 78 Å^3 and 0.008(6) Å, respectively. Tracing the unit cell compression up to 2.96 GPa (Figure 4) shows that the gradient of compression increases over this pressure regime, suggesting that the framework becomes *more compressible* on increasing pressure. This behaviour is similar to that observed in our previous work on the metal organic frameworks MOF-5 and Cu-btc,[14] but quite the opposite to what was observed in ZIF-8 on compression using MeOH:EtOH as a hydrostatic liquid, where a continuous increase in MeOH in the content of the pores was observed to 1.47 GPa. We attribute this rapid pore filling behaviour in pentane:isopentane to the chemical nature of the framework and guest. Pentane and isopentane are non-polar molecules and thus have a lower energy barrier to entering the hydrophobic pore of ZIF-8 compared to the *smaller* polar methanol and ethanol molecules. The saturation of pentane and isopentane molecules in the pores at 0.85 GPa could also be the result of the larger size of the molecules, which accounts for the sudden decrease on increasing pressure. This may indicate that the same behaviour could be observed in ZIF-8 in MeOH:EtOH but at higher pressures.

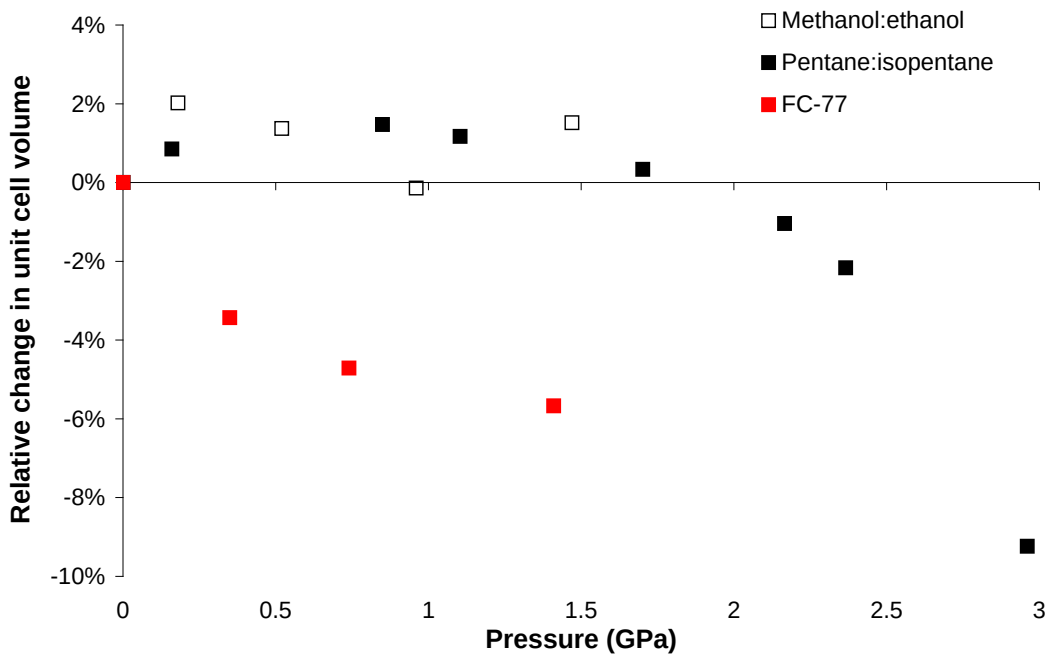

Figure 4. Relative change in unit cell volume of ZIF-8 in MeOH:EtOH (open squares), pentane:isopentane (black squares), and Fluorinert (red squares) as a function of applied pressure.

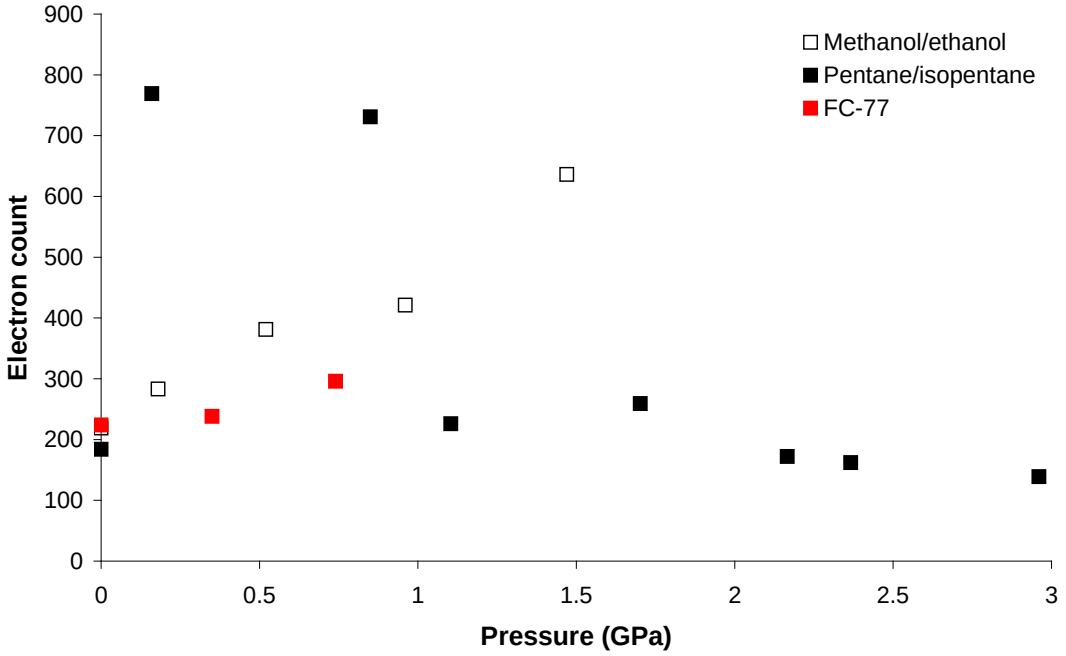

Figure 5. Electron count per unit cell for ZIF-8 in MeOH:EtOH (open squares), pentane:isopentane (black squares), and Fluorinert (red squares) as a function of applied pressure, calculated using the *SQUEEZE* algorithm in PLATON.

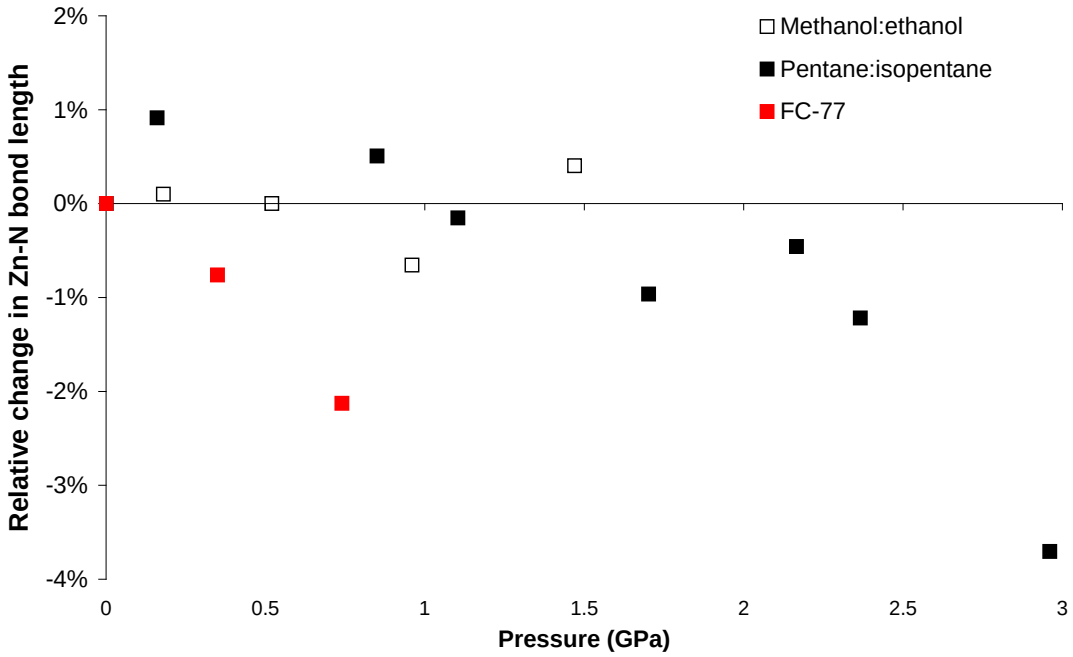

Figure 6. Relative change in Zn-N bond length during compression of ZIF-8 in various hydrostatic mediums.

Supersaturation of the pores on inclusion of pentane and isopentane is also supported in the measured electron count (Figure 5), which is almost three times greater at ≈ 0.18 GPa in pentane:isopentane than it is in MeOH:EtOH. The expansion of the pores (and therefore unit cell volume) does not match this uptake, though again we attribute this to the hydrophobic nature of the pores, which make them more likely to interact with the more hydrophobic pentane:isopentane molecules.

In the previous high-pressure study of ZIF-8 using MeOH:EtOH, on increasing pressure from 0.96 to 1.47 GPa, a phase transition was observed which resulted in a twisting of the MIm groups and a subsequent increase in accessible porous volume and content (Figure 5). This twisting can be quantified by looking at the angle subtended between a plane made through the imidazolate ring, and the unit cell axes, which at ambient temperature and pressure measures ≈ 25° (Figure 7). On initially increasing pressure in MeOH:EtOH from ambient to 0.18 GPa, a small increase in the rotation angle can be seen (by 5.1°), which coincides with an uptake of four additional MeOH molecules (12 to 16) within the pores. On increasing pressure further to 0.96 GPa, the imidazolate rotation angle remains relatively

unchanged even though the pore content continually increases. On increasing pressure from 0.96 to 1.47 GPa (to the ZIF-8-HP phase), the rotation angle suddenly *decreases* from 30.2 to 0.0° respectively, in order to substantially increase the pore volume (Figure 7). In our study using pentane:isopentane, some movement of the imidazole rings is also observed. As the pressure is increased from ambient to 0.85 GPa, the imidazolate rings rotate from 25.5 to 27.0°, and coincides with an associated increase in pentane:isopentane content equivalent to 14 pentane molecules. Increasing the pressure from 0.85 to 1.10 GPa, within the region where the pentane:isopentane is flushed out of the framework, the rotation angle remains relatively unchanged, decreasing marginally from 31.9 to 31.7°. On increasing pressure to 2.96 GPa, the imidazolate rotation angle continues to decrease from 31.7 to 16.0°. The initial increase in imidazolate rotation angle would therefore appear to be the mechanism by which molecules enter the central pore volume (as observed in both MeOH:EtOH and pentane:isopentane). The subsequent *decrease* in imidazolate rotation angle observed after evacuation of the pentane:isopemtane must therefore occur in order for the framework to minimize its volume to accommodate the increase in pressure. The imidazolate angle would therefore appear to be a structure directing 'gauge' or 'gate' which indicates the uptake of guest molecules.

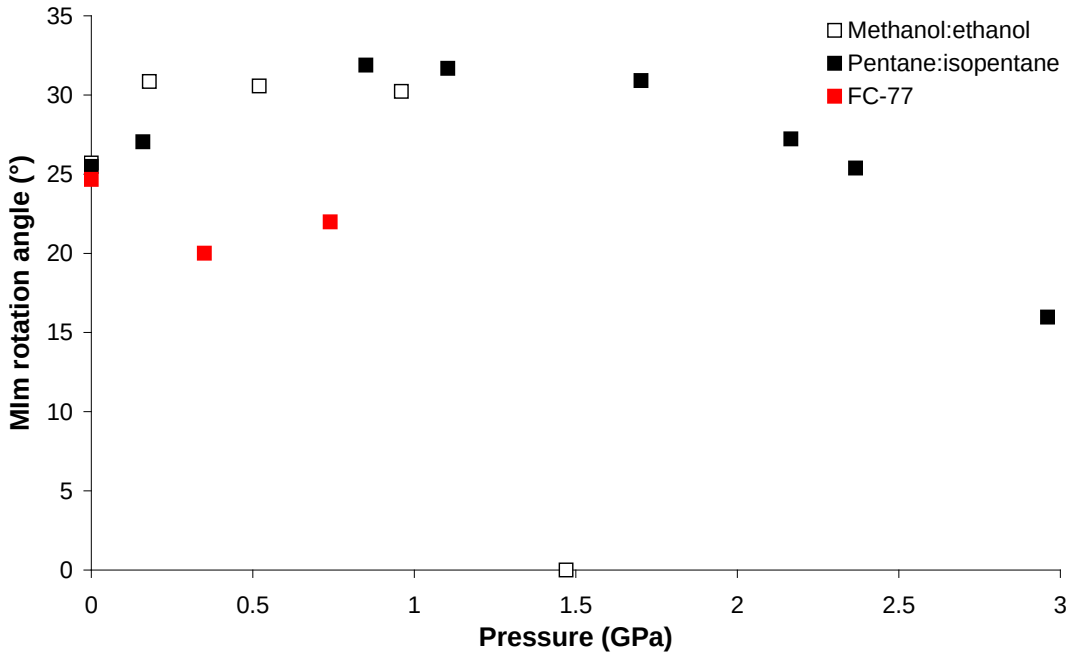

Figure 7. MIm ring rotation angle as a function of pressure for ZIF-8.

Evacuation of the pores continues to 2.96 GPa with the final pore content determined as 139 e-/unit cell, 45 electrons (and 2.5 methanol molecules fewer per unit cell) than the ambient pressure structure. A pore content less than that of the ambient pressure structure suggests that not only has pressure expelled the pentane:isopentane that had previously been forced into the pores at lower pressure, but also that the methanol molecules present post-synthesis are also forced out of the framework. As the unit cell volume decreases, the Zn-N bond lengths decrease from 1.967(6) to 1.897(12) Å causing opposing methyl groups to be forced closer together as the sides of the 4-membered ring contract. Consequently, the MIm rings rotate in order to minimize the steric interactions between them, yielding a more favourable conformation.

The geometry optimization of ZIF-8 was carried out in the absence of medium molecules to save on computational complexity and also to allow for the investigation of the pressure response of the framework without the influence of guest molecules. The lattice parameters of the geometry optimized structure of ZIF-8, hereafter called ZIF-8_{EVAC}, were in good agreement with the experimentally determined values at ambient temperature and pressure; ZIF-8_{EVAC} a = 17.1632 Å

and V = 5055.9 Å^3, ZIF-8 = 17.001(3) Å and 4914(2) Å^3. The MIm rings also optimized to a position very close to the experimental value i.e. ZIF-8$_{EVAC}$ = 25.2° *c.f.* 25.5° for the experimentally measured angle (Figure 8a).

A further geometry optimization was carried out on the structure of ZIF-8$_{EVAC}$, this time with an applied pressure of 5 GPa. The unit cell volume decreased to 3443.7 Å^3 (32 % smaller than ZIF-8$_{EVAC}$ at ambient pressure) which is significantly below the lowest volume observed experimentally. This highlights a limitation of the computational modelling, which cannot model catastrophic events such as the onset of amorphization. It is interesting to note, however, that the increase in pressure and corresponding decrease in unit cell volume caused the MIm rings to rotate to form the ZIF-8-HP structure (Figure 8b).

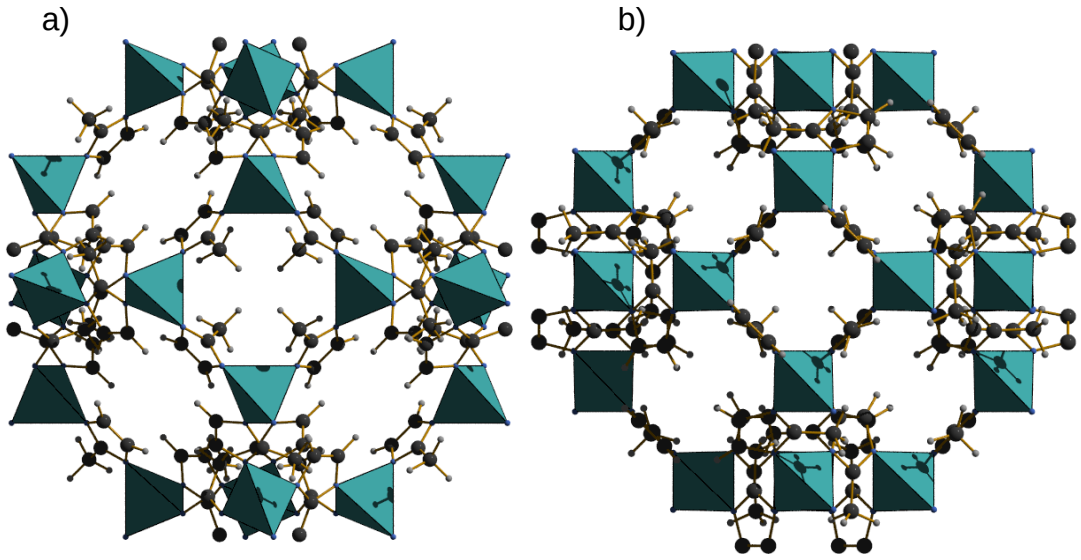

Figure 8. Geometry optimized of ZIF-8$_{EVAC}$ at a) ambient pressure and b) 5 GPa. Even in the absence of guest molecules, the application of pressure causes the negative rotation of the MIm rings to accommodate the decrease in unit cell volume.

The energies associated with the geometry optimized structures of ZIF-8$_{EVAC}$ at ambient pressure and 5 GPa, differed by 40 kJmol^{-1}. To probe the effect of MIm ring rotation on the energy, a series of single point energy calculations were carried out starting from the geometry optimized structure of ZIF-8$_{EVAC}$. The structure was altered by rotating the MIm ring independently of the structure and the energy was

calculated while the structure was constrained, therefore the energy is relative rather than absolute (Figure 9).

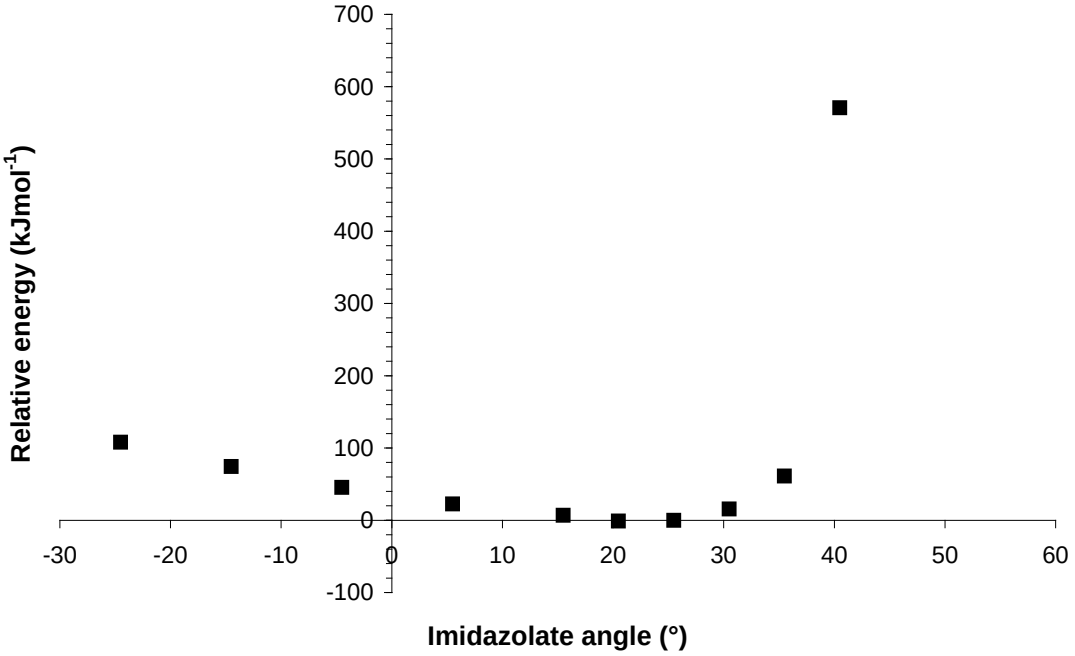

Figure 9. Relative energy of MIm rotation for ZIF-8_{EVAC} taken from a series of single point energy calculations.

The energy profile clearly shows the large barrier to positive rotation of the MIm rings in ZIF-8, with the methyl groups being pushed into sterically unfavourable proximity. The energy associated with the high pressure structure i.e. when the rotation angle = 0°, is approximately 38 $kJmol^{-1}$, in very close agreement with the energy difference calculated for the geometry optimized ambient and high pressure structures of ZIF-8_{EVAC}.

5.3.2 Compression of ZIF-8 in Fluorinert FC-77

In order to observe the effect of compression in a non-penetrating medium we chose the per-fluorinated aliphatic compound Fluorinert FC-77 as a hydrostatic liquid, as it is too large to enter the pores (Figure 10).

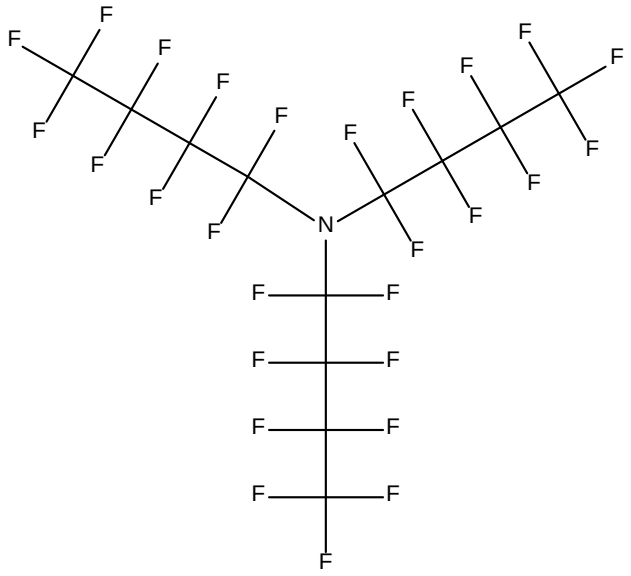

Figure 10. Schematic representation of Fluorinert FC-77.

On increasing pressure from ambient to 0.35 GPa, a 166(6) Å^3 (3.4%) decrease in unit cell volume was observed (Figure 4). This is in contrast with the response of ZIF-8 to compression using both MeOH:EtOH and pentane:isopentane, which both *increase* by 99.1(8) Å^3 (2.0%) and 41.775(3) Å^3 (0.85%), respectively. On increasing pressure further, a smooth and continuous decrease in volume occurs, with the framework compressing in total by 5.7% at 1.41 GPa. At this pressure, the crystal began to break apart, and the resolution of the data decreased rapidly (> 1.8 Å). As a result, only the unit cell parameters and volume are reported. On increasing pressure above 1.41 GPa, the sample became amorphous, and no structural data could therefore be determined.

The compression of ZIF-8 here in Fluorinert is typical for compression curves of molecular solids, where the gradient of the unit cell compression decreases over the course of the pressure regime (the crystal becomes less compressible with

increasing pressure). This behaviour highlights the non-penetrating nature of Fluorinert as a hydrostatic medium, which is also supported by the pore content, which remains essentialy unchanged on increasing pressure from ambient to 0.74 GPa.

Similar to the compressibility of ZIF-8 in pentane:isopentane and MeOH:EtOH, the imidazolate ring rotation again seems to play a pivotal role in accommodating the unit cell volume decrease in Fluorinert, with the imidazolate rotation angle decreasing by 2.7º on increasing pressure to 0.74 GPa. This coincides with a much more drastic decrease in the Zn-N bonds compared to compressing in both pentane:isopentane and MeOH:EtOH, decreasing by 0.042(10) Å (4.2 σ) from ambient to 0.74 GPa (Figure 6). The total pore volume also reduces by 137 Å^3. The lowest observable unit cell volume for the ambient pressure crystalline phase of ZIF-8 in Fluorinert is 4558(14) Å^3 (Figure 4). Interestingly, however, in pentane:isopentane the smallest unit cell volume observed was 4460(12) Å^3 measured at 2.96 GPa, 98(18) Å^3 lower. Application of pressure using a penetrating medium (such as pentane:isopentane) therefore not only confers a level of resistivity to applied pressure but also stabilizes the crystalline ZIF-8 phase when compressed to lower volume. Similar behaviour has been observed previously in MOF-5 and HKUST-1, where inclusion of small penetrating guest molecules inferred a level of resistivity (and stability) to hydrostatic compression.[14] Previous work has also shown that application of non-hydrostatic pressure to ZIF-8 produced an irreversible amorphization above 0.34 GPa[15]. Here, ZIF-8 remained crystalline under direct (non-penetrating) hydrostatic pressure up to 2.96 GPa. This suggests that deviatoric stress on the material must play a pivotal role in the onset of amorphization.

5.4 Conclusions

In summary, on increasing pressure to 0.85 GPa using pentane:isopentane, the hydrostatic liquid is forced inside the pores of ZIF-8 causing the unit cell (and pore volume) to expand, identical to the behaviour observed on applying pressure using MeOH:EtOH as a hydrostatic liquid, though the expansion observed here is not as significant. On increasing pressure further to 1.10 GPa, the pentane:isopentane medium is forced out of the pores, quite dissimilar to the compressibility in MeOH:EtOH, while further compression to 2.96 GPa results in direct compression of the framework.

The compressibility of ZIF-8 in pentane:isopentane is driven by the compressibility of the Zn-N bonds, which expand and compress in conjunction with the unit cell volume. The uptake and expulsion of medium from the pores appears to be highly dependent of the imidazolate ring rotation, which initially rotate in a 'positive' direction (see Figure 2) in order to uptake pentane molecules, then rotate in a 'negative' direction in order to allow the pores to compress at higher pressures *i.e.* >1.7 GPa. On increasing pressure to 0.85 GPa, saturation of pentane:isopentane in the pores occurs with a pore content equivalent to 14 pentane molecules per unit cell. A sudden expulsion of hydrostatic medium from the pores occurs upon increasing pressure to 1.10 GPa, with the electron count returning to near-ambient pressure values despite the unit cell volume remaining 57(3) $Å^3$ (1.2%) larger than the ambient pressure structure. Further increases in pressure resulted in the material becoming *more* compressible until the onset of an irreversible single crystal to amorphous transition.

Performing a geometry optimization on ZIF-8 in the absence of any guest molecules, ZIF-8_{EVAC}, yielded a structure almost identical to that determined experimentally. Applying 5 GPa pressure to this structure resulted in a rotation of the MIm rings, analogous to that seen in the previously reported phase transition. The energy difference between these structures was calculated as 40 $kJmol^{-1}$, in very good agreement with a series of single point energy calculations performed on structures created by rotation of the MIm rings.

Applying pressure to ZIF-8 without the effect of guest inclusion highlighted the role of the Zn-N bond compression for pressure accommodation, and the rotation of the imidazolate rings. In Fluorinert, ZIF-8 shows no increase in volume and instead behaves much more like a molecular solid, with the material becoming *less* compressible with increasing pressure. The decrease in lattice volume is accompanied by a direct compression of the Zn-N bond lengths which decrease by 0.04(1) Å (2%) between ambient pressure and 0.74 GPa, and a twisting of the MIm rings, similar to the rotation observed within the pore emptying region in pentane:isopentane (rotating in a 'negative' direction). A decrease in the rotation angle would therefore appear to allow the framework to decrease in volume, rather than being an influence of the excluded guest molecules. Compared with the behaviour of ZIF-8 in Fluorinert, application of pressure using a penetrating medium (such as pentane:isopentane) confers a level of resistivity to applied pressure and stabilizes the crystalline ZIF-8 phase when compressed to lower volume, though the saturation of the pore at 1.10 GPa, and the onset of a pore-emptying region is in stark contrast to the behaviour in MeOH:EtOH, in which a continuous increase in pore content occurs to 1.47 GPa.

5.5 References

1 X.-C. Huang, Y.-Y. Lin, J.-P. Zhang and X.-M. Chen, *Angew. Chem., Int. Ed.*, 2006, **45**, 1557.

2 S. A. Moggach, D. R. Allan, S. Parsons and J. E. Warren, *J. Appl. Crystallogr.*, 2008, **41**, 249.

3 G. J. Piermarini, S. Block, J. D. Barnett and R. A. Forman, *J. Appl. Physics*, 1975, **46**, 2774.

4 A. Dawson, D. R. Allan, S. Parsons and M. Ruf, *J. Appl. Crystallogr.*, 2004, **37**, 410.

5 Bruker-Nonius, Bruker-AXS, Madison, Wisconsin, USA, 2006.

6 S. Parsons, The University of Edinburgh, Edinburgh, United Kingdom, 2004.

7 G. M. Sheldrick, *SADABS Version 2008-1*, 2008.

8 P. W. Betteridge, J. R. Carruthers, R. I. Cooper, K. Prout and D. J. Watkin, *J. Appl. Crystallogr.*, 2003, **36**, 1487.

9 A. L. Spek, Utrecht University, Utrecht, The Netherlands, 2004.

10 S. J. Clark, M. D. Segall, C. J. Pickard, P. J. Hasnip, M. J. Probert, K. Refson and M. C. Payne, *Z. Kristallogr.*, 2005, **220**, 567.

11 H. Wu, W. Zhou and T. Yildirim, *J. Am. Chem. Soc.*, 2007, **129**, 5314.

12 J. P. Perdew, K. Burke and M. Ernzerhof, *Phys. Rev. Lett.*, 1996, **77**, 3865.

13 C. F. Macrae, I. J. Bruno, J. A. Chisholm, P. R. Edgington, P. McCabe, E. Pidcock, L. Rodriguez-Monge, R. Taylor, d. S. J. van and P. A. Wood, *J. Appl. Crystallogr.*, 2008, **41**, 466.

14 A. J. Graham, D. R. Allan, A. Muszkiewicz, C. A. Morrison and S. A. Moggach, *Angew. Chem., Int. Ed.*, 2011, **50**, 11138.

15 K. W. Chapman, G. J. Halder and P. J. Chupas, *J. Am. Chem. Soc.*, 2010, **131**, 17546.

Chapter 6

The effect of pressure on Sc-based MOFs

6.1 Introduction

Recent interest in gas storage materials has seen a vast increase in the number of publications devoted to the synthesis of microporous metal-organic framework materials.[1] In certain circumstances, uptake of guest molecules can have a major influence on the structure and properties of MOFs, including changing their magnetic and luminescence properties.[2] In some flexible MOFs, for example in the metal terephthalate MIL-53 and MIL-88, a stepwise uptake of guest molecules occurs at a certain 'gating' pressure,[3] though more recent work has shown that this process is highly dependent on the nature of the adsorbate and is time-dependant.[4] This unusual sorption behaviour, referred to as 'breathing', is caused by a reversible modulation of the structure which results in a significant increase in volume (up to 125% for MIL-88B(Cr)).[5] The modulation allows the MOF to uptake more guest molecules into its pores, and highlights the importance of obtaining structural data as a function of guest uptake since it often leads to changes in the pore size, shape and therefore selectivity. In other more rigid systems, less drastic 'breathing' behaviour has been observed. In the zeolitic imidazolate MOF called ZIF-8 ($Zn(MIm)_2$, MIm = 2-methylimidazole), the MIm groups twist at higher partial pressures during sorption measurements in order to accommodate more guest molecules[6] (as discussed in Chapter 5). In even more rigid systems such as $Zn_2(bdc)_2(dabco)$, much less pronounced changes in volume have been observed, though counter intuitively, the framework expands upon guest release and shrinks upon guest uptake.[7] The hydrophilic/hydrophobic nature of the pores can also have a pronounced effect on guest uptake. In the Cu-framework STAM-1 ($((Cu_3O_{21}C_{30}H_{24})_n.5_n(H_2O))$), the formation of both hydrophilic and hydrophobic channels in the same structure results in pore-discriminating adsorption of guests, with CO_2, N_2, N_2O and hexane all showing much lower uptake than expected (based on the known crystal structure) as these are only adsorbed into the hydrophobic channels.[8] Uptake of methanol and H_2O however takes place in both pores. This has been seen in our work at high pressure where the uptake of methanol post-synthetically modified the pores and therefore their discriminatory properties (see Chapter 4).

Recently a scandium terephthalate (Sc_2BDC_3, BDC = 1,4-benzenedicarboxylate) MOF has been made which has a high density of

terephthalate linkers, resulting in the formation of small hydrophobic pores with channels measuring ≈ 4 Å in diameter. Despite its small pore character, it is possible to prepare the MOF with monofunctionalized ligands of the form $O_2CC_6H_3XCO_2$ (X = NH_2 or NO_2), where the X-substituent is disordered over two positions on the BDC linker. Under ambient pressure conditions, Sc_2BDC_3 is known to undergo a phase transition from *Fddd*, to *C*2/*c* on cooling below 225 K, or on sorption of CO_2 and H_2 at one atmosphere and 235 and 80 K respectively.[9, 10] The orthorhombic form has also demonstrated negative thermal expansion behaviour between 225 and 523 K caused by carboxylate group rotation. The structure of $Sc_2(NO_2\text{-}BDC)_3$ however, shows no such transition and remains isostructural to the monoclinic form of Sc_2BDC_3 between 100 to 473K, while $Sc_2(NH_2\text{-}BDC)_3$ is isostructural to the orthorhombic phase of Sc_2BDC_3 between 100 to 298K. All three derivatives show uptake of CO_2 though whether any phase transition takes place is currently unknown.

Here we describe the effect of pressure and guest uptake in Sc_2BDC_3 and $Sc_2(NO_2\text{-}BDC)_3$ at GPa pressures in two different hydrostatic media: methanol and Fluorinert FC-77 (perfluorotripentylamine).

6.2 Experimental

6.2.1 Synthetic procedure and crystal growth

Single-crystal samples of Sc_2BDC and $Sc_2(NO_2\text{-}BDC)_3$ were synthesised by and very gratefully received from Dr John Mowat in the group of Prof Paul Wright at St Andrews University. Below are the procedures followed for the synthesis of these samples:

Sc_2BDC_3 synthesis: $Sc(NO_3)_3{\cdot}_4H_2O$ (0.34 g, 99.9%, 1.1 mmol), H_2BDC (0.170 g, 99%, 1 mmol), H_2O_2 (30 wt% in H_2O, 0.25 mL), pyridine (0.5 mL, 99%) and DMF (10 mL, 99.8%) were stirred in a Teflon-lined steel autoclave. The autoclave was then placed in an oven and heated at 493 K for 48 hours. The autoclave was cooled to room temperature and crystals were isolated by Buchner filtration washed with DMF and dried in air.

$Sc_2(NO_2\text{-}BDC)_3$ synthesis: $Sc(NO_3)_3{\cdot}_4H_2O$, NO_2-BDC and water were mixed together in a 1:1.5:600 molar ratio in a Teflon-lined steel autoclave. The

autoclave was then placed in an oven and heated to 463 K for 72 h. The autoclave was cooled to room temperature and crystals were isolated by Buchner filtration.

6.2.2 High-pressure single-crystal X-ray diffraction experiments

6.2.2.1 General procedures

High-pressure experiments were carried out using a modified Merrill-Bassett diamond anvil cell (DAC) equipped with 600 μm culet diamonds and a tungsten gasket.[11] The sample and a chip of ruby (as a pressure calibrant) were loaded into the DAC using one of two hydrostatic media; methanol (MeOH) and Fluorinert (FC-77), a liquid mixture of fluorinated aliphatic compounds. The ruby fluorescence method was utilised to measure the pressure.[12]

6.2.2.2 Data Collection, Reduction and Refinement

Before each pressure study, an ambient pressure and temperature single-crystal X-ray diffraction data set was collected on a Bruker APEXII diffractometer with graphite-monochromated Mo *K*α radiation (λ = 0.71073 Å). These data were integrated using the programme SAINT[13], while the absorption corrections were carried out using the program SADABS[14]. Refinements were carried out against $|F|^2$ using all data using CRYSTALS[15]. Pore volume and water content were calculated using the *SQUEEZE* algorithm within PLATON.[16] Refinements were carried out against $|F|^2$ using all data starting from the ambient temperature coordinates of Mowat *et al*..[9]

During refinement of data at each pressure point, all 1,2 and 1,3 distances were restrained to the values observed from our ambient pressure values for the organic linkers. Metal to ligand bond distances and angles were allowed to refine freely. All non-hydrogen atoms were refined anisotropically with thermal similarity and vibrational restraints applied to all non-hydrogen atoms except Sc.

High-pressure single-crystal X-ray diffraction data were collected on a Bruker APEXII diffractometer using Mo Kα radiation (λ = 0.71073 Å). Data were collected in ω-scans in eight settings of 2θ and ϕ with a frame time and step size of one second and 0.3° respectively. This data collection strategy was based on that described by Dawson *et al.*[17] The data were integrated using the program SAINT using 'dynamic masks' to avoid integration of regions of the detector shaded by the

body of the pressure cell. Absorption corrections for the DAC and sample were carried out using programs SHADE[18] and SADABS respectively.

6.2.2.3 Compression of Sc_2BDC_3 using Methanol

A crystal of Sc_2BDC_3 was loaded into a DAC using methanol as the hydrostatic medium. Compression data were collected in approximately 0.4 GPa steps from 0.3 to 3.0 GPa. Data collection, integration, processing and crystallographic refinements and restraints followed the procedure outlined above. The diffraction resolution limit decreased as a function of pressure, with an attributed decrease in data quality being observed. As a result only unit cell dimensions are reported above 2.3 GPa. On increasing pressure above 3.0 GPa, the sample became polycrystalline and no data could be extracted.

On increasing pressure to 0.3 GPa, methanol molecules from the hydrostatic medium were forced into the pores. Two symmetry independent methanol molecules were found through Fourier difference maps. The positions and isotropic displacement parameters of these included molecules were refined, though the C-O bond length was restrained to 1.47(1) Å. Thermal similarity restraints were also applied. One of the methanol molecules was located in a general position. Its occupancy was refined freely as a function of pressure (Table 1). The second methanol was located about a 2-fold axis. The identity of the methyl group on this disordered methanol molecule could not be determined. Nevertheless, even though either the methyl C-atom or hydroxyl O-atom was disordered about the 2-fold axis, the site contains in total one fully occupied methanol molecule. The final occupancy values of methanol molecules on both sites were also compared to those calculated utilising the program *SQUEEZE* (Table 1).

6.2.2.4 Compression of Sc_2BDC_3 using Fluorinert

A crystal of Sc_2BDC_3 was loaded into a DAC using Fluorinert FC-77 as the hydrostatic medium. Compression data were collected at 0.14 GPa. Data collection, integration, processing and crystallographic refinements and restraints followed the

procedure outlined above. Pressure was increased further to 0.40 GPa. This increase in pressure was accompanied by a colour change in the crystal from colourless to opaque. A high-pressure data collection was attempted on the opaque crystal; however no diffraction was observed, indicating the sample had become amorphous. On decreasing pressure, the transition was found to be reversible, with the crystal colour reverting back to colourless. The crystal was recovered to ambient pressure and an ambient pressure and temperature single-crystal X-ray diffraction data set was collected on an Agilent SuperNova diffractometer with graphite-monochromated Cu *K*α radiation (λ = 1.5418 Å), equipped with an Atlas detector. These data were integrated using the programme CrysAlisPro and absorption corrections were carried out in the same programme.[19] Refinements were carried out against $|F|^2$ using all data in CRYSTALS. Pore volume and water content were calculated using the *SQUEEZE* algorithm within PLATON. Refinement was carried out against $|F|^2$ using all data starting from the ambient temperature coordinates of Mowat *et al*.

6.2.2.5 Raman spectroscopy of Sc_2BDC_3 using Fluorinert

Raman spectra were collected on another single-crystal of Sc_2BDC_3 on a Jobin-Yvon LabRam 300 Raman spectrometer. The same crystal was then loaded in a DAC using Fluorinert as a hydrostatic medium to 0.1 GPa, and Raman spectra collected again. The pressure was then increased to 0.7 GPa (above the amorphization pressure), and Raman spectra collected on the amorphous sample. Amorphization of the sample was confirmed by the previously observed colour change from colourless to opaque. The pressure was then released to 0.1 GPa, upon which the sample reverted back to colourless again. The crystal was then recovered from the pressure cell. Single-crystal X-ray diffraction data were then collected on the recovered sample at room temperature and ambient pressure on a Bruker SMART APEX diffractometer with graphite-monochromated Mo Kα radiation (λ = 0.71073 Å).

6.2.2.6 Computational Details

Note: Grand canonical Monte Carlo (GCMC)[20] simulations were performed in order to study methanol adsorption in Sc_2BDC_3. These were performed by Dr Tina Düren

of the Institute of Materials and Processes, School of Engineering, The University of Edinburgh. This section is included here for the sake of completeness.

The framework atoms remained fixed at their crystallographic positions, while the number of methanol molecules was allowed to fluctuate. Trial moves consisting of random insertions, deletions, rotations and translations of methanol molecules were performed while the temperature and chemical potential of the system were kept constant. Dispersion interactions were determined using the Lennard-Jones (LJ) model[21] and the Lorentz-Berthelot mixing rules were employed in obtaining cross-interaction parameters. Coulombic interactions were calculated with the Ewald summation method.[22] All framework atoms were represented using parameters taken the Dreiding force field[23], with the exception of scandium which was modelled using the Universal Force Field (UFF)[24]. Lennard-Jones parameters and partial charges describing methanol molecules were obtained the TraPPE force field.[25] Partial charges for the framework atoms were taken directly from the work of Mowat *et al.*[26] The simulations were carried out with the multipurpose simulation code (MuSiC),[27] and consisted of 6 x 10^6 simulation steps, 40% of which were used for system equilibration. Once equilibrium was reached the centre of mass locations of methanol molecules were recorded at regular intervals, along with methanol-framework and methanol-methanol interaction energies.

6.2.2.7 Compression of $Sc_2(NO_2\text{-}BDC)_3$ using Methanol

Crystals of $Sc_2(NO_2\text{-}BDC)_3$ tend to be twinned i.e. composed of two separate domains. In order to be able to collect high-pressure data, a crystal in which both domains could be easily separated were loaded into a DAC using methanol as the hydrostatic medium. Compression data were collected in approximately 0.4 GPa steps from 0.2 to 1.2 GPa. Above 0.9 GPa, the diffraction resolution decreased substantially (> 1.5 Å). As a result, no further structural data could be extracted above 0.9 GPa.

Data collection and crystallographic refinements and restraints followed the procedure outlined above. The data were integrated as a two component twin, with the absorption corrections carried out using the program TWINABS. A twin scale

factor was calculated within TWINABS, and the data were refined against a merged hkl file.

All non-hydrogen atoms were refined with anisotropic displacements parameters with the exception of the disordered -NO_2 groups, which were refined with isotropic displacement parameters and restrained to a chemical occupancy of 0.5.

6.2.2.8 Compression of $Sc_2(NO_2\text{-}BDC)_3$ using Fluorinert (FC-77)

A twinned crystal of $Sc_2(NO_2\text{-}BDC)_3$ with well separated domains was loaded into a DAC to 0.3 GPa using Fluorinert as a hydrostatic medium. Data collections were carried out in approximately 0.4 GPa steps up to 2.6 GPa. On increasing pressure from 0.4 to 0.8 GPa, a single-crystal to single-crystal phase transition was observed to a new phase which we have designated $Sc_2(NO_2\text{-}BDC)_3$-HP. The transition was accompanied by a change in space group symmetry from *C*2/*c* to *Fdd*2. $Sc_2(NO_2\text{-}BDC)_3$-HP was solved using direct methods. High-pressure data were collected on $Sc_2(NO_2\text{-}BDC)_3$-HP to 2.6 GPa. On increasing pressure above 2.2 GPa (to 2.6 GPa), a rapid decrease in resolution of the data was observed, with the sample becoming polycrystalline. As a consequence, only unit cell dimensions are reported at 2.6 GPa. Above 2.6 GPa, the sample became amorphous. Data collection, integration, processing and crystallographic refinements and restraints followed the procedure outlined above for compression using methanol.

6.3 Results and Discussion

6.3.1 Compression of Sc_2BDC_3 using Methanol

Under ambient temperature and pressure conditions Sc_2BDC_3 crystallises in the orthorhombic space group *Fddd*; a = 8.7467(2) Å, b = 20.7505(4) Å, c = 34.3708(6) Å and V = 6238.2(2) Å^3. The structure of Sc_2BDC_3 is constructed via octahedral Sc-metal centres, with each Sc-atom coordinated to six BDC linkers. The BDC linkers bridge across four separate Sc-atoms with each carboxyl oxygen bonded to one Sc-atom forming a small pore framework with pores measuring ≈ 3 Å in diameter (Figure 1). On looking in projection down the *a*-axis the pores appear one dimensional, however there are small voids between adjacent BDC ligands which

interconnect the pore channels along the *b* and *c*-axes (Figure 2). Under ambient pressure and temperature conditions, the orthorhombic form of Sc_2BDC_3 has two symmetry independent BDC molecules; the first has an inversion centre at the centre of the BDC ring (BDC'), while the other is bisected by two perpendicular 2-fold axes and penetrated by a third (BDC''). The voids formed between pairs of BDC' and BDC'' molecules form the interconnecting channels along the *b*- and *c*-axis directions respectively, giving rise to a three dimensional porous framework structure.

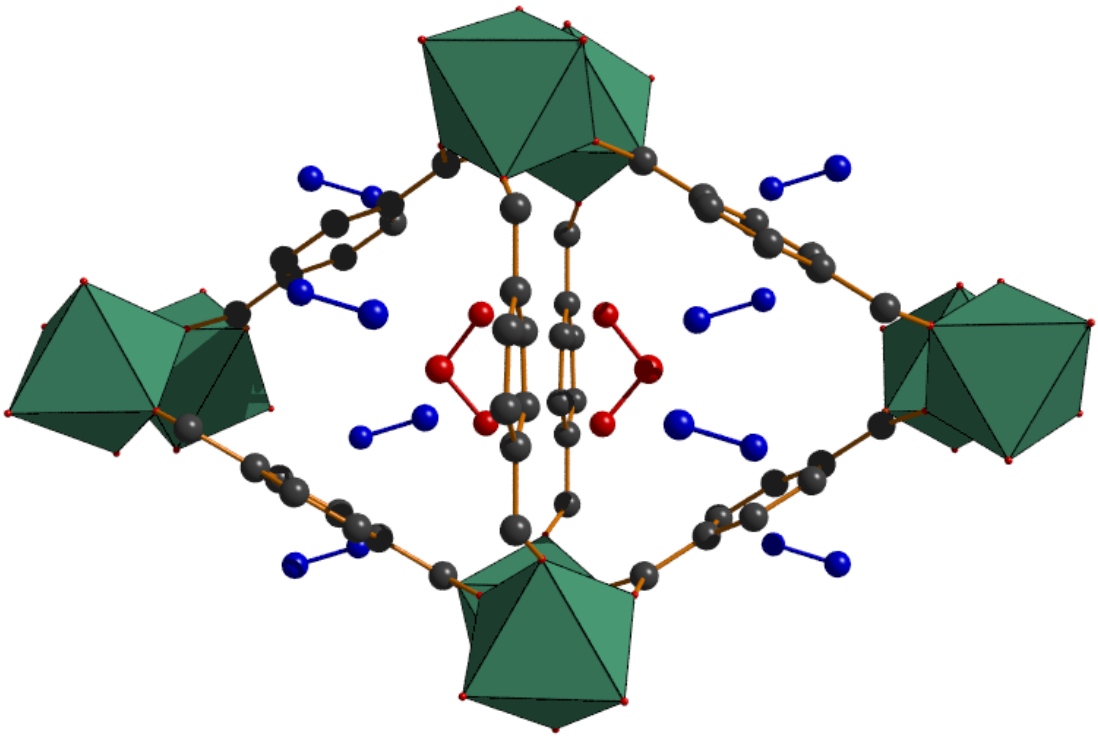

Figure 1. Triangular pores formed in Sc_2BDC_3 viewed along the *a*-axis. Disordered methanol molecules are represented by solid red (site 1) and blue (site 2) coloured molecules. Key: C, grey, ScO_6 octahedra, green. H atoms have been omitted for clarity of view.

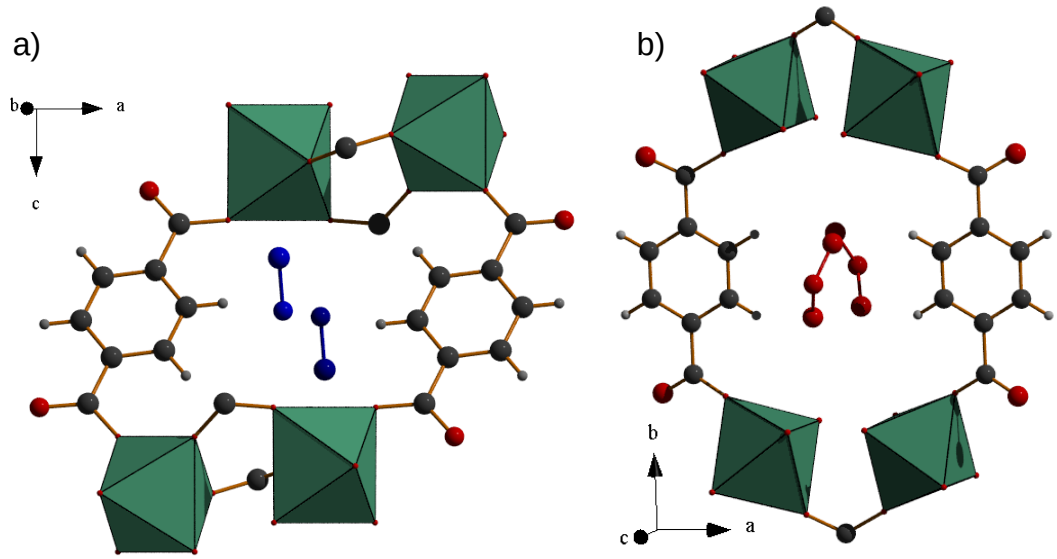

Figure 2. Two distinct channels formed in Sc_2BDC_3 between (a) BDC' and (b) BDC'' ligands as viewed along the *c* and *b*-axes, respectively. Disordered methanol molecules interacting between the channels are shown as solid red and blue molecules. Key: as for Figure 1 with the addition of H, light grey.

On initially loading the sample using methanol as a hydrostatic liquid to 0.3 GPa, the unit cell volume expanded, corresponding to inclusion of methanol molecules into the framework (Figure 1, Table 1). Expansion of the framework continued to 0.6 GPa, with the unit cell volume increasing by 41.4 Å^3 (0.7%). On further increasing the pressure to 1.1 GPa, the volume began to compress, with the volume continually compressing until the maximum pressure of 3.0 GPa was reached (Figure 3). The compressibility of the unit cell dimensions is anisotropic, with appreciable differences observed in the relative compressibilities (Figure 4). The *a*-axis, for example, follows the same trend as the unit cell volume, showing an initial increase in length to 1.1 GPa, followed by a continuous compression to 3.0 GPa. Contrary to this, both the *b* and *c*-axes decrease in length for the entirety of the pressure study.

Table 1. Electron count, no. of MeOH molecules and MeOH density are all calculated from the PLATON *SQUEEZE* algorithm. Occupancy of Site-2 MeOH molecules calculated from *SQUEEZE*, and freely refined from the model is also shown.

Pressure (GPa)	Electron count	MeOH molecules	MeOH density (gcm^{-1})	Occupancy of Site-2 MeOH molecules	Freely refined Site-2 MeOH molecule occupancy.
0.0	169	9	0.23	-0.21	N/A
0.3	572	32	0.76	0.49	0.51
0.6	695	39	0.91	0.71	0.69
1.1	744	41	0.96	0.79	0.81
1.4	683	38	0.92	0.69	0.79
1.6	747	42	1.01	0.80	0.80
2.3	699	39	0.98	0.71	0.75

The anisotropic compression of the unit cell dimensions (and volume) can be explained by analysing the uptake of methanol molecules within the pores of Sc_2BDC_3 on increasing pressure. On initially applying pressure to 0.3 GPa, the guest methanol molecules occupy two distinct sites. Site-1 (Figures 1 & 2b) is occupied by a fully ordered methanol molecule (though disordered about a 2-fold axis) and lies just above a pair of BDC'' ligands. Pairs of site-1 methanol molecules sit on either side of the BDC'' ligands with the minimum distance between site-1 molecules measuring 2.492 Å, interacting along the *c*-axis direction. Site 2 is only half occupied at 0.3 GPa with the site-2 methanol sitting in a general position between BDC' ligands (Figures 1 & 2a). In a similar fashion to site-1, pairs of site-2 molecules sit on either side of the channels formed between BDC' ligands, with the minimum distance between site-2 molecules measuring 2.316 Å, interacting along the *b*-axis direction.

Overall, at 0.3 GPa one fully ordered site-1, and two partially ordered site-2 molecules occupy the 1D pores which run along the *a*-axis, interacting in a pair-wise fashion along the *b* and *c*-axis directions. This stacking of methanol molecules along the *a*-axis (principal pore direction) results in the expansion of the *a*-axis on increasing pressure to 0.3 GPa. The short distance between pairs of methanol molecules would seem to indicate that guest-guest interactions are the driving force for the packing of methanol molecules inside the pores and the subsequent increase

in the *a*-axis. This is further supported by the fact that the shortest distance between site-1 and site-2 molecules and the framework at 0.3 GPa is 3.136 and 3.383 Å respectively; over 0.6 Å longer than the shortest methanol-methanol distance. Even further evidence is the greater compressibility of the *b* and *c*-axes, which further promotes guest-guest interactions between methanol molecules, with the minimum methanol-methanol distance measuring 2.467 and 3.056 Å at 2.3 GPa for pairs of site-1 and site-2 molecules respectively, just slightly shorter than those observed at 0.3 GPa. This means that the pores are becoming longer and thinner in order to accommodate the pressure increase and the pressure-induced filling of the channel.

Inclusion of methanol molecules results in no change of symmetry. Sc_2BDC_3 however is known to undergo a transition from *Fddd* to *C*2/*c* on uptake of CO_2 guest molecules. The transition observed on inclusion of CO_2 is driven by a small but significant twist of the ring in BDC' ligands. No transition is observed on uptake of methane and ethane.[10] In the case of methanol here, hydrophilic methanol molecules are forced into the small hydrophobic pores. Guest-guest interactions dominate and therefore there is little guest-framework interaction and thus no driving force for the space group symmetry to change.

On increasing pressure above 0.3 GPa, the occupancy of site-2 molecules increases, reaching a peak occupancy of 0.8 at 1.1 GPa. Contraction of both the *a*-axis and volume however starts to occur above 0.6 GPa. It would therefore appear that the swelling effect caused by continuous inclusion of methanol molecules stacking along the *a*-axis is overcome above 0.6 GPa. Instead, compression of the *a*-axis, and therefore volume, is preferred. No appreciable increase in methanol density is observed above 1.1 GPa, and therefore direct compression of the framework takes place to 3.0 GPa.

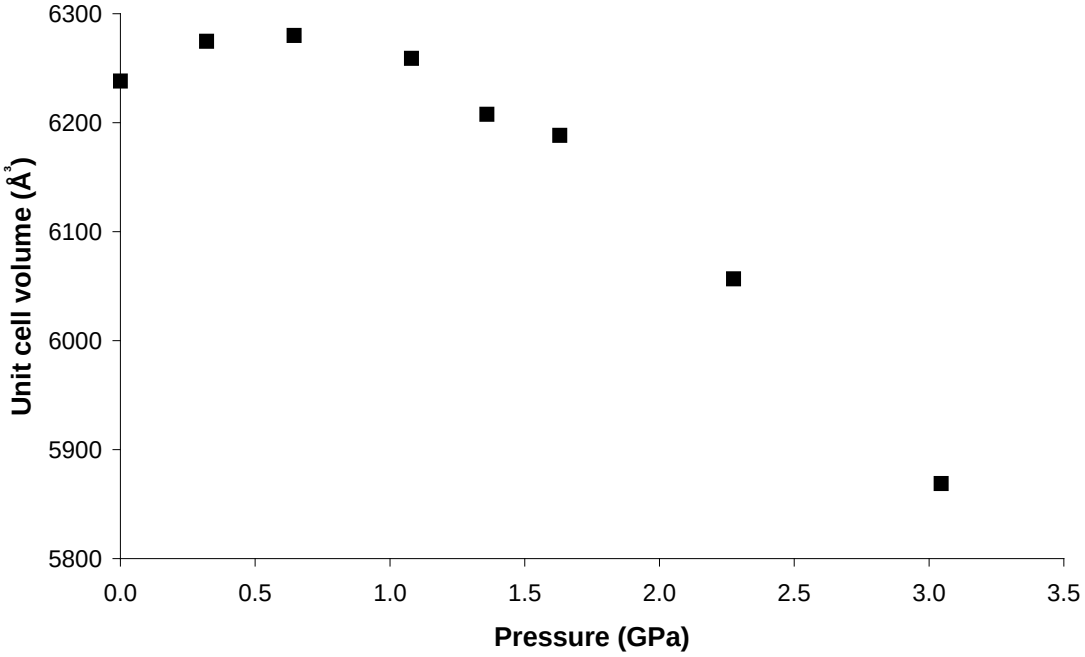

Figure 3. Unit cell volume of Sc_2BDC_3 in methanol as a function of pressure.

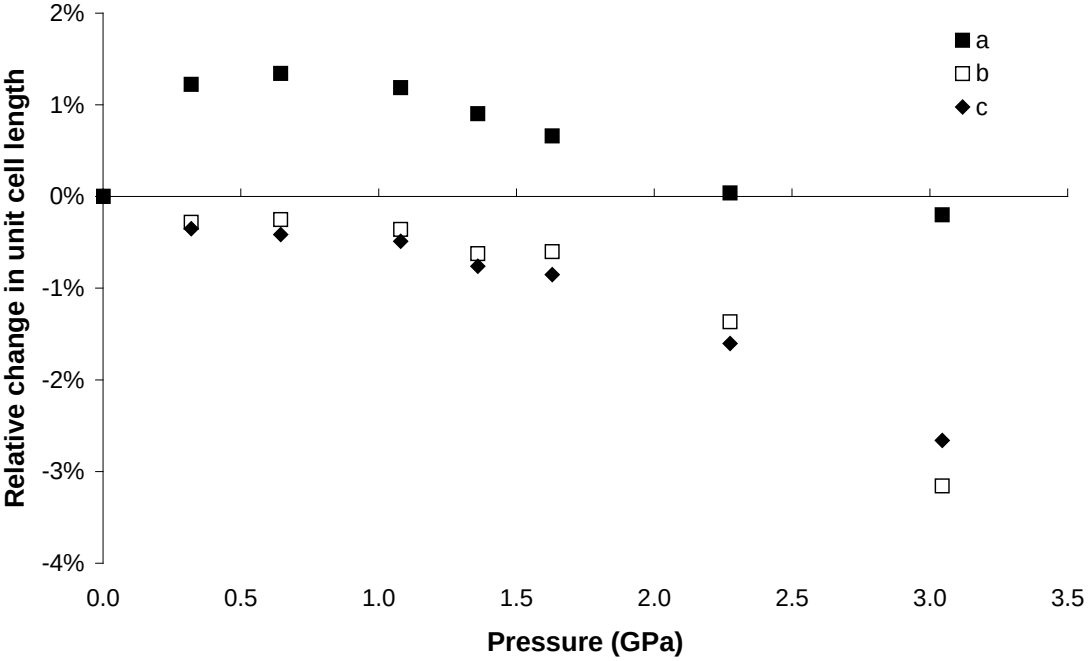

Figure 4. Relative change in unit cell lengths of Sc_2BDC_3 in methanol as a function of pressure.

6.3.2 Methanol Interaction Energies and Adsorption Sites from GCMC Simulations

Molecular simulations were performed in order to assess the strength of guest-framework and guest-guest interactions with increasing methanol loading. Energy histograms were obtained for the 0.0 GPa Sc_2BDC_3 structure as well as for six Sc_2BDC_3 configurations determined at the various pressure points of the methanol compression experiment (Table 1). The interaction energies determined for the six high pressure structures display a similar pattern, with slight differences in the distributions resulting from changes in the framework configuration. A significant difference however, can be observed between the patterns observed for the ambient and high-pressure structures (Figure 5), which shows histograms for the methanol-framework and methanol-methanol interaction.

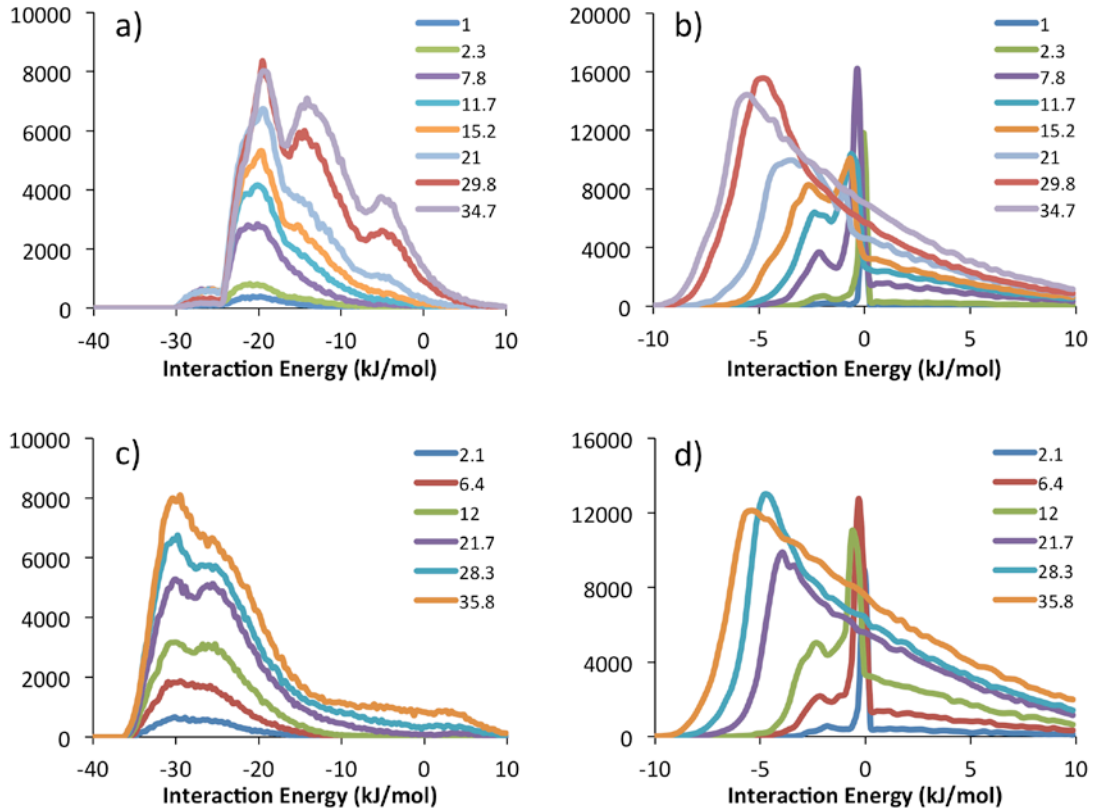

Figure 5. Interaction energy histograms at different loadings in molecules / unit cell: guest-framework a) and guest-guest interactions b) determined for the Sc_2BDC_3 0.0 GPa structure, and guest-framework c) and guest-guest interactions d) determined for the Sc_2BDC_3 0.6 GPa structure.

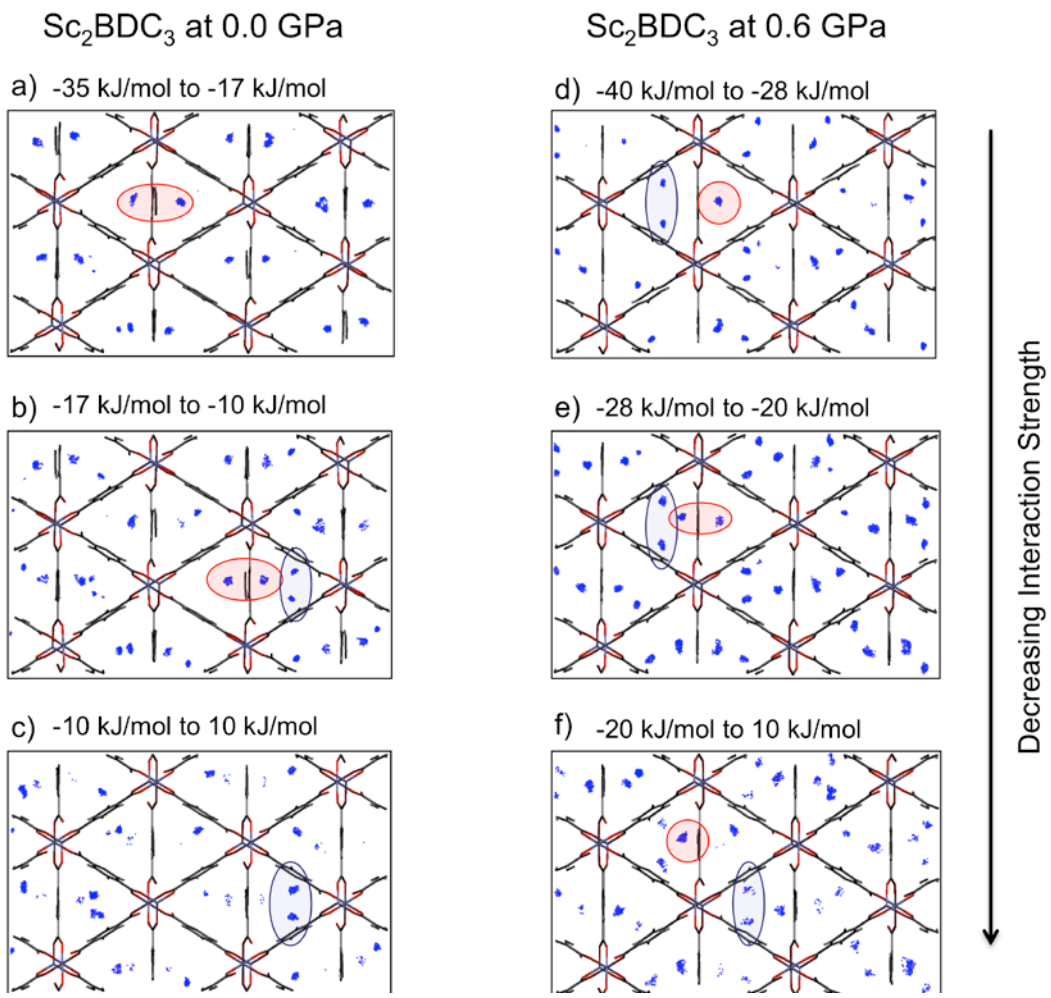

Figure 6. Density distribution plots for the adsorption of methanol in 0.0 GPa Sc_2BDC_3 a) to c), and in 0.6 GPa Sc_2BDC_3 d) to f). Each plot shows the locations of molecules adsorbed within a particular interaction energy range corresponding to the peaks in the energy histograms of Figure 5. Each dot represents the position of the centre of mass of a molecule during the GCMC simulation. Red and blue highlighted regions were used to denote adsorption at Site 1 and Site 2 respectively.

These results highlight the effect of the structural changes in the Sc_2BDC_3 framework on the adsorption of methanol molecules. In the 0.0 GPa structure, molecules are first adsorbed at Site 1. Adsorption is facilitated by an increase in methanol-methanol interactions with loading. On increasing pressure, the framework undergoes slight changes in configuration resulting in significantly stronger methanol-framework interactions at both Site 1 and Site 2, and leading to a filling of both adsorption sites.

The guest-guest interactions modelled for the two Sc_2BDC_3 configurations appear to be similar in both magnitude and their response to loading. As pressure

increases, methanol molecules pack close to one another inside the pores, and the interactions between them become stronger. The adsorbate-framework histograms on the other hand differ in the number of peaks as well as well as interaction strength. For the 0.0 GPa Sc_2BDC_3, the strongest methanol-framework interactions are approximately -30 kJ/mol, however only a small number of molecules occupy the highest energy sites between -25 kJ/mol and -30 kJ/mol. There are three main energy peaks, centred at -20 kJ/mol, -14 kJ/mol and -5 kJ/mol respectively. As shown in Figure 5 a) the lowest energy peak corresponds to molecules being adsorbed at Site 1, while the highest energy peak represents adsorption mainly at Site 2. Between -17 kJ/mol and -10 kJ/mol methanol molecules appear to be adsorbed at both, Site 1 and 2. In the case of the 0.6 GPa structure, the entire distribution has shifted towards stronger (i.e. more negative) interaction reaching energies as low as -36 kJ/mol, and indicating that methanol molecules interact much more strongly with the framework than in the 0.0 GPa configuration. The methanol-framework energy histogram in Figure 5 c) has only two broad peaks, centred close together at -30 kJ/mol and -25 kJ/mol respectively. As a result, methanol molecules are adsorbed at both, Site 1 and 2 with similar interaction energies, as shown in Figure 6 d), e) and f).

6.3.3 Compression of Sc_2BDC_3 using Fluorinert

Loading a crystal of Sc_2BDC_3 in Fluorinert FC-77 to 0.1 GPa resulted in a decrease in unit cell volume of 16 $Å^3$. This is in contrast to the 41.4 $Å^3$ *increase* in unit cell volume observed when loaded with methanol at 0.3 GPa. This variation in behaviour can be explained by the difference in hydrostatic medium. Fluorinert (a large perfluorinated molecule) is too large to penetrate the pore volume of Sc_2BDC_3, therefore direct compression of the framework occurs. On increasing the pressure further to 0.4 GPa, there was a crystalline-to-amorphous phase transition, which was accompanied by an optical change in the crystal from colourless to opaque (Figure 7a). The Raman spectra collected within the fingerprint region of the spectra (100 to 1300 cm^{-1}) were almost identical (Figure 8), which indicates that the local structure of Sc_2BDC_3 in the amorphous phase is retained. The sample was recovered to ambient pressure and the crystal returned from opaque to colourless (Figure 7b). Single-crystal X-ray diffraction data collected on the recovered crystal confirmed

that the amorphization was fully reversible, with the structure reverting back to the original crystalline phase. The fact that the transition is reversible further supports our assumption that the framework remains essentially intact during the transition. The phenomenon of pressure-induced amorphization has been known for several years, with amorphous ice being the most well-known example.[28] Reversible pressure-induced amorphization has been observed previously in zeolites which have the LTA structure type[29] and inorganic materials such as $CsAuI_3$[29] and $Ge_2Sb_2Te_5$[30]. More recently, the reversible pressure-induced amorphization of the zeolitic imidazole framework ZIF-4 ($[Zn(Im)_2]$, Im = imidazolate) was observed between 0.35-0.98 GPa for the evacuated sample, or 1.49-4.54 GPa for the solvent-containing sample.[31] The compressibility behaviour observed here in Sc_2BDC_3 is therefore very similar to that observed in ZIF-4, with the crystalline-amorphous phase transition observed upon direct compression of the bare framework at low pressures (*ca.* < 1 GPa; similar to the evacuated sample of ZIF-4), while inclusion of solvent molecules upon compression with methanol stabilises the crystalline phase to much higher pressures. Not all MOFs exhibit reversible crystalline-amorphous transitions. In ZIF-8 and MOF-5, amorphization is irreversible, and occurs at much lower pressures.[32] In MOF-5, amorphization occurs on grinding the sample at 3.5 MPa. Nevertheless, as with the reversible crystalline-amorphous transitions observed in ZIF-4 and Sc_2BDC_3, the pressure at which the onset of amorphization occurs in MOF-5 can be delayed by guest inclusion, with MOF-5 becoming amorphous above 3.2 GPa upon hydrostatic compression with DEF[33] (see Chapter 2). More recently, in a high-pressure study of the flexible framework NH_2-MIL-53-(In), guest inclusion also occurs and pressure-induced amorphization does not take place until >20 GPa.[34]

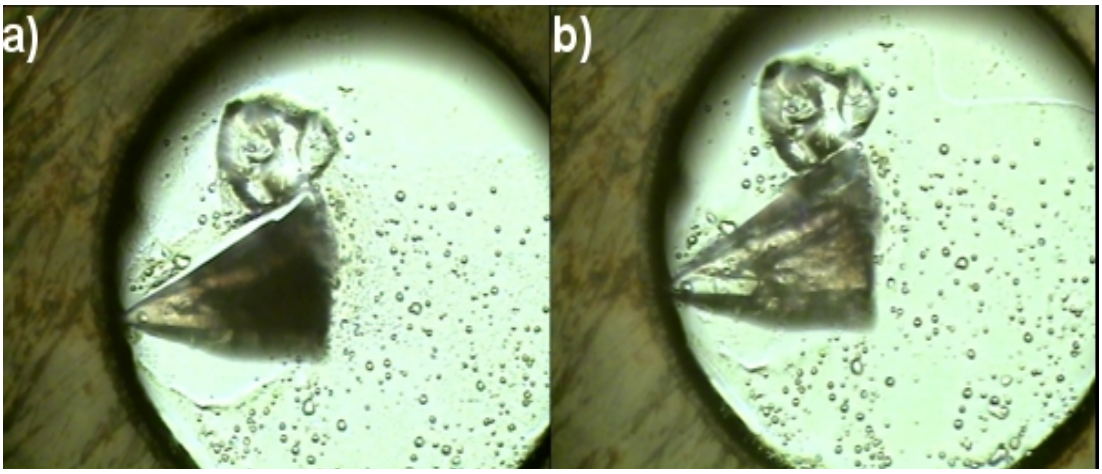

Figure 7. Optical image of Sc_2BDC_2 loaded in Fluorinert FC-77 at a) 0.40 GPa and b) 0.10 GPa.

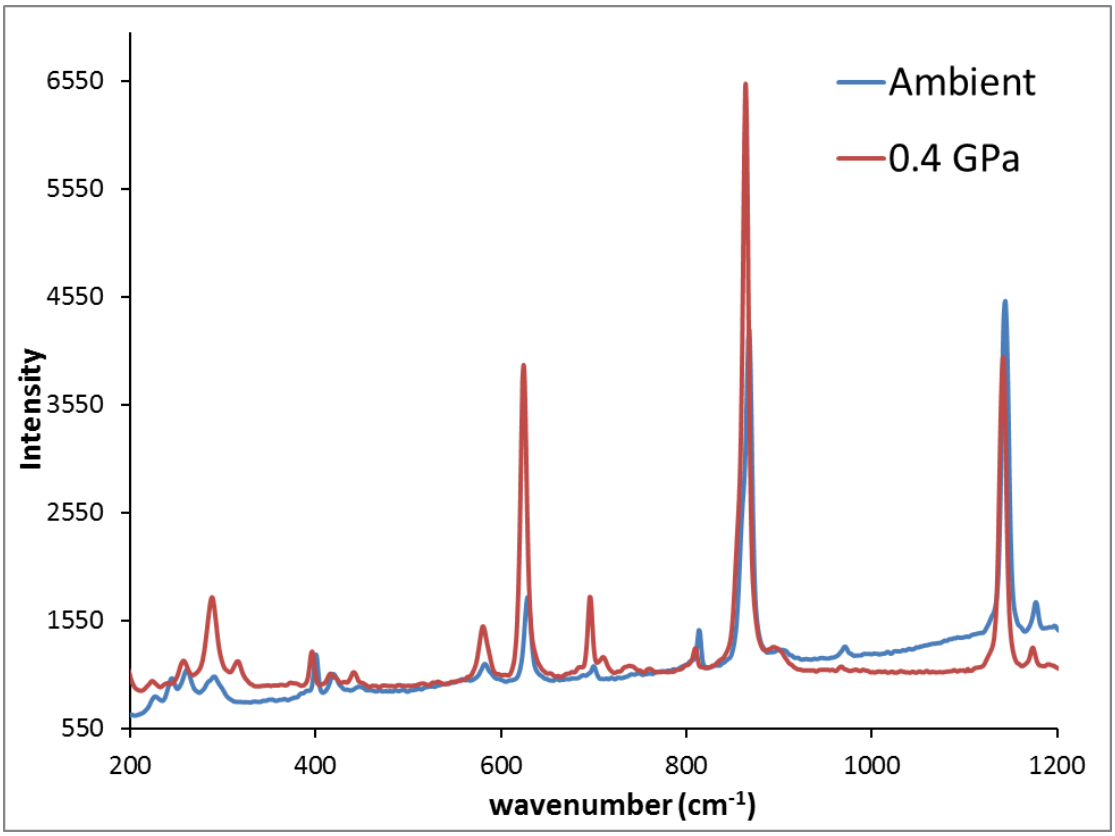

Figure 8. Raman spectra of crystalline Sc_2BDC_3 at ambient pressure (blue), and the amorphous phase of Sc_2BDC_3 at 0.4 GPa (red).

6.3.4 Compression of $Sc_2(NO_2\text{-}BDC)_3$ using Methanol

At ambient pressure and temperature, $Sc_2(NO_2\text{-}BDC)_3$ crystallises in the monoclinic space group *C*2/*c*; *a* = 8.6786(3) Å, *b* = 34.4286(13) Å, *c* = 11.0628(4) Å, *β* = 110.482(2)° and *V* = 3096.4(2) Å^3. Topologically, the framework is very similar to the native Sc_2BDC_3 structure composed of the same 1D channels (Figure 9). The NO_2 group however is disordered over two positions by an inversion centre (BDC') and by a two-fold rotation axis (BDC''). This results in the orthorhombic *Fddd* symmetry being broken and as a result, a smaller aperture is formed between pairs of BDC' and BDC'' ligands.

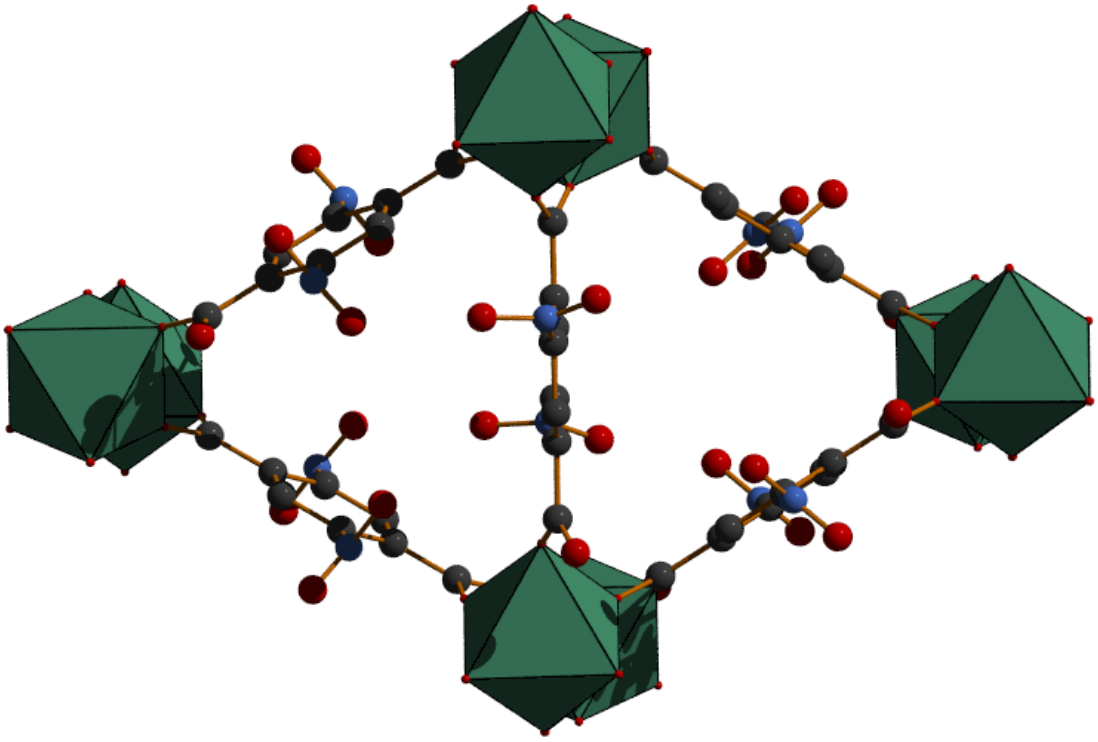

Figure 9. Triangular pores formed in $Sc_2(NO_2\text{-}BDC)$ viewed along the *a*-axis. Colour scheme: O, red; C, grey; N, blue and ScO_6 octahedra, green.

On initially loading a crystal of $Sc_2(NO_2\text{-}BDC)_3$ into a DAC to 0.21 GPa using methanol as the hydrostatic media, the unit cell volume decreased by 32.69 Å^3 (0.52 %, Figure 10). With increasing pressure further to 0.9 GPa, the volume continued to decrease, however above 0.9 GPa, a quite drastic decrease in volume is observed which continues to 3.3 GPa. Unfortunately, unlike the native Sc_2BDC_3 sample, the high-pressure data is not of high enough quality to be able to extract atomic structural information on the pore contents, nor model the uptake of solvent

via the *SQUEEZE* algorithm. Nevertheless, the evidence for methanol inclusion as a function of pressure can be inferred based on the anisotropic compression of the unit cell dimensions. On increasing pressure to 0.2 GPa, and then further to 0.9 GPa, the *a*-axis increases (by 0.11%), while the *b* and *c*-axes both decrease by 0.13 and 0.28% respectively (Figure 11). This behaviour is identical to the native Sc_2BDC_3, where the axis along which the porous channels of the framework run (which is also the ≈ 8 Å *a*-axis), increases in length. The increase in length of the *a*-axis in $Sc_2(NO_2\text{-}BDC)_3$, however is much less drastic and reflects the lower uptake and reduced 'swelling' of the pores. This is unsurprising considering the lower uptake of CO_2 observed in previous studies caused by the bulky NO_2 side groups, with the overall effect of pressure causing a volume reduction to 0.9 GPa, rather than expansion which is observed in Sc_2BDC_3 to 0.6 GPa.

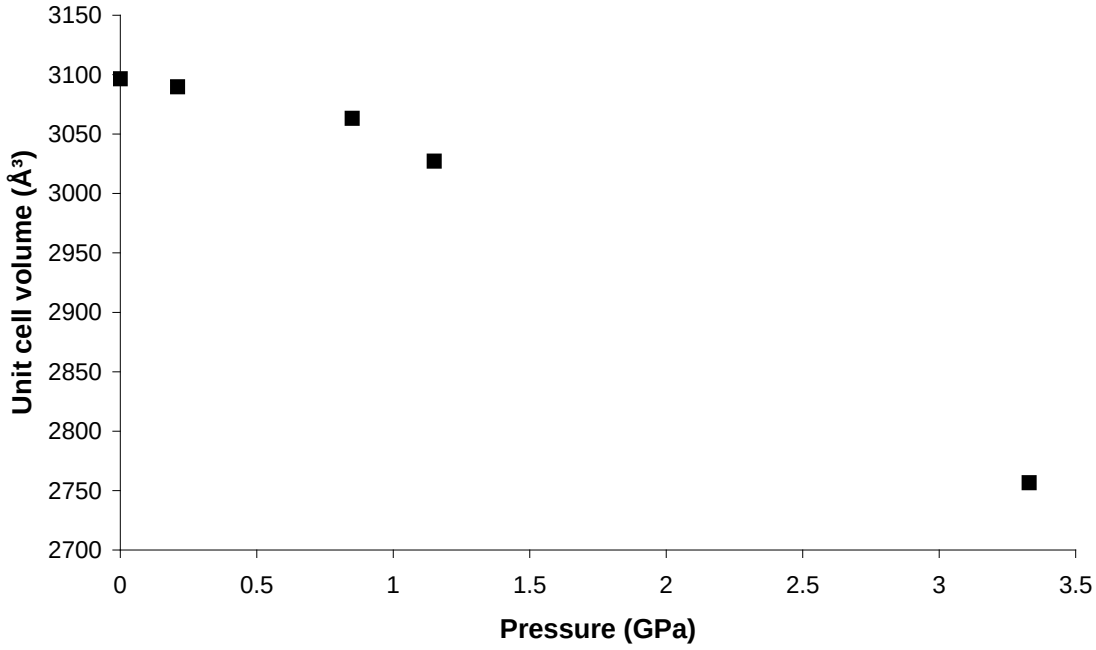

Figure 10. Unit cell compression of $Sc_2(NO_2\text{-}BDC)_3$ in methanol as a function of pressure. Two regions of compressibility are observed with the transition pressure of 0.9 GPa.

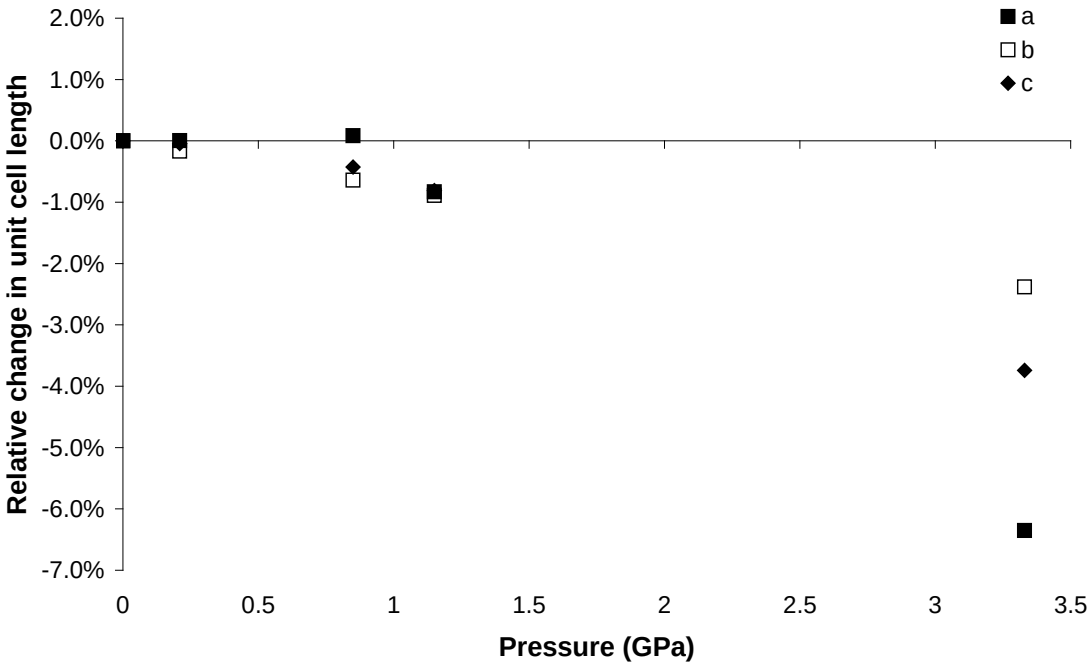

Figure 11. Relative change in unit cell length of $Sc_2(NO_2\text{-}BDC)_3$ in methanol as a function of pressure.

Above 0.9 GPa, the *a*-axis (and volume) contracts more dramatically. This behaviour is typical of porous MOFs where two phases of different compressibility take place. In Cu-btc, this transitional behaviour was attributed to pore hyperfilling by the hydrostatic liquid followed by a sudden emptying of the pores at higher pressures, resulting in a material which becomes more compressible at higher pressures.[35] We, however cannot conclude that this occurs in $Sc_2(NO_2\text{-}BDC)_3$, as similar behaviour is observed in Sc_2BDC_3, where the methanol content actually reached saturation by 1.1 GPa, and remains in the pores until at least 2.3 GPa, despite clearly showing two regions of quite different compressibility. Uptake of methanol molecules above 2.3 GPa in $Sc_2(NO_2\text{-}BDC)_3$ has been impossible to measure to date, and further work would be required in order to ascertain whether guest uptake increases, decreases or plateaus at higher pressures.

6.3.5 Compression of $Sc_2(NO_2\text{-}BDC)_3$ *using Fluorinert*

In order to ascertain whether a similar crystalline to amorphous phase transition is observed in $Sc_2(NO_2\text{-}BDC)_3$ at high pressure (as was observed with Sc_2BDC_3), and to de-convolute the effect of pressure and solvent inclusion, a separate high-pressure experiment was carried out on $Sc_2(NO_2\text{-}BDC)_3$ using Fluorinert as non-penetrating

hydrostatic medium. On increasing pressure from ambient to 0.4 GPa, direct compression of the framework occurs, and is reflected in the compressibility of all three axes and the volume (Figures 12 and 13). In particular, direct compression of the *a*-axis takes place, highlighting the anisotropic compression of the (≈ 8 Å) *a*-axis as a useful indicator for guest inclusion in Sc-based MOFs.

On increasing pressure further to 0.8 GPa, a single-crystal to single-crystal phase transition occurs with a resulting crystallographic symmetry change from space group *C*2/*c* to *Fdd*2. The new phase (hereafter referred to as $Sc_2(NO_2\text{-}BDC)_3$-HP), is formed by an approximately 25° tilting of the ScO_6 octahedra and is characterized by a drastic distortion (and collapse) of the 1-D porous channels (Figure 14).

There is not a direct symmetry pathway for the transition from *C*2/*c* to *Fdd*2 therefore it must take place via an intermediate phase. We postulate that the structure may adopt an intermediate *Cc* structure before adopting the *Fdd*2 $Sc_2(NO_2\text{-}BDC)_3$-HP structure, though we see no evidence for this transition state, the symmetry path would appear to be a logical route.

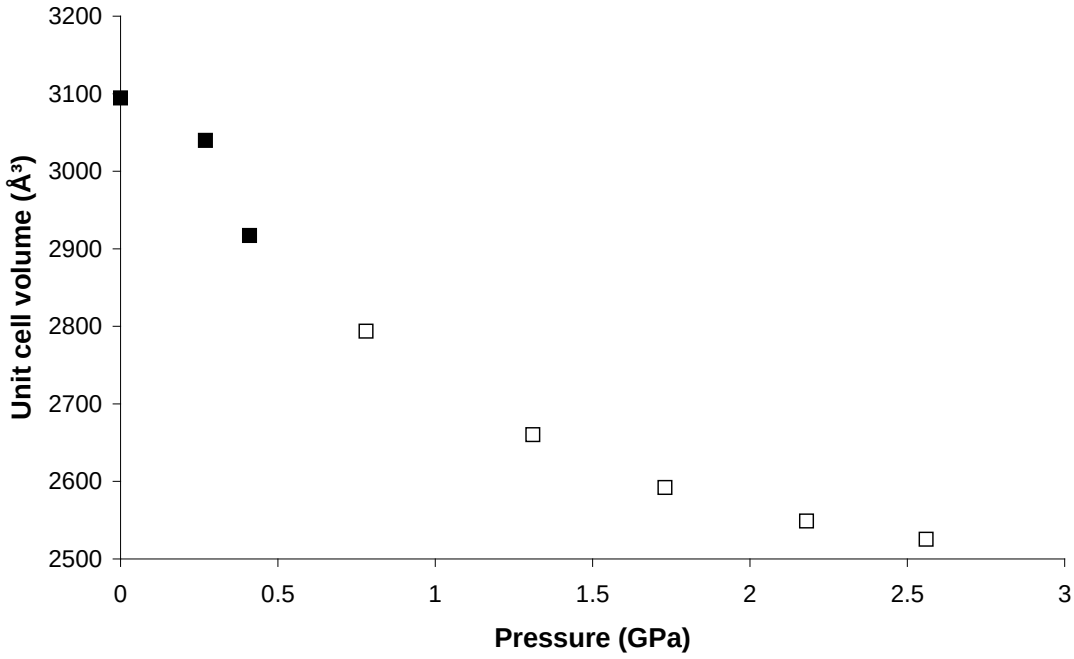

Figure 12. Unit cell volume response as a function of applied pressure for $Sc_2(NO_2\text{-}BDC)_3$ in FC-77. Closed squares, *C*2/*c* structure; open squares, *Fdd*2 structure (with unit cell halved for comparison with monoclinic structure).

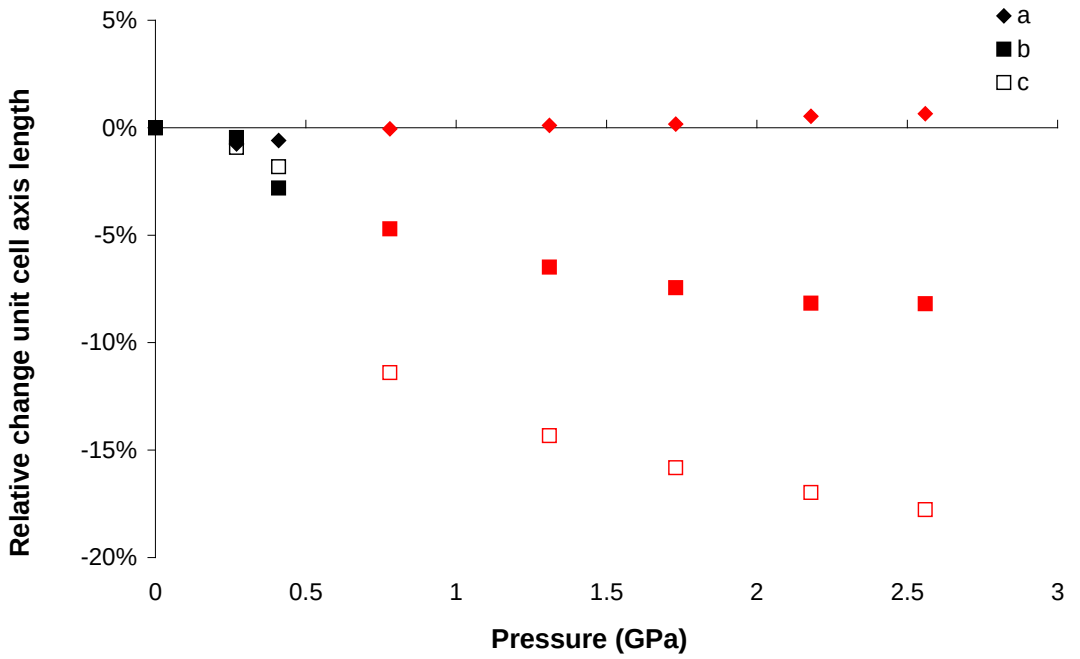

Figure 13. Unit cell axes response to applied pressure for $Sc_2(NO_2\text{-}BDC)_3$ in FC-77. Black data points, *C*2/*c* structure; red data points, *Fdd*2 structure. The percentage changes are based on a comparison of the cell based on the monoclinic setting, i.e. the *a*- and *c*-axes have been reversed and the length of the new orthorhombic *c*-axis (monoclinic *a*-axis) has been halved.

Above 0.8 GPa, the framework showed continued compression with the compressibility decreasing with increasing pressure. Above 2.6 GPa, the sample underwent an irreversible amorphization.

A comparison of the compression curves for $Sc_2(NO_2\text{-}BDC)_3$ in methanol and Fluorinert reveals the contrasting behaviour of $Sc_2(NO_2\text{-}BDC)_3$ with guest inclusion. The gradient of the unit cell compression decreases in Fluorinert as a function of pressure as the sample becomes less compressible with increasing pressure. This behaviour is typical for molecular materials where direct compression takes place. The compressibility in methanol is quite different, as the sample becomes *more compressible* at higher pressures, confirming methanol guest inclusion in $Sc_2(NO_2\text{-}BDC)_3$ on applying pressure.

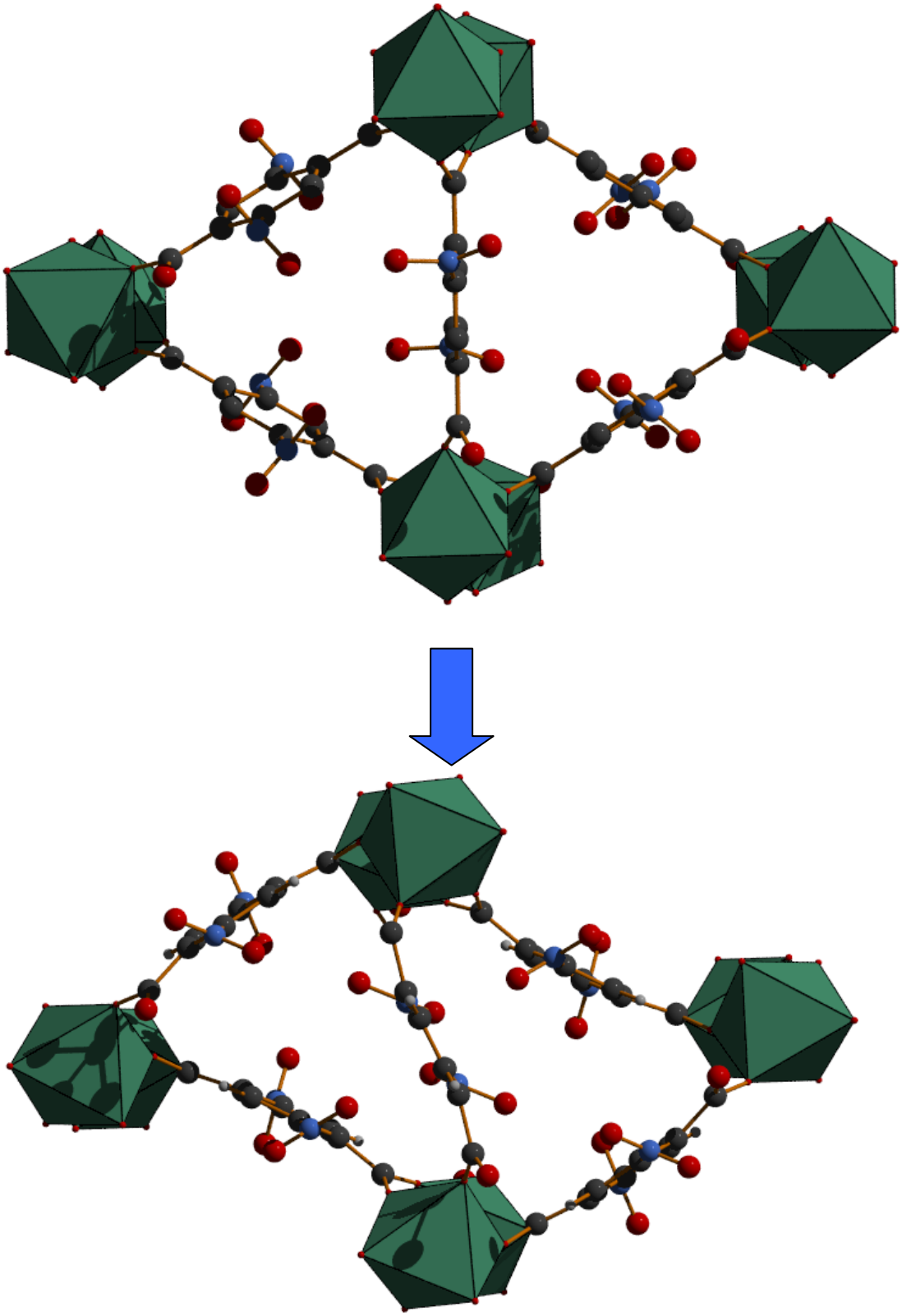

Figure 14. Structural transition of $Sc_2(NO_2\text{-}BDC)_3$. The ScO_6 octahedra tilt by approximately 25° from the ambient pressure topology causing the collapse of the 1D porous network. Colour scheme as for Figure 9.

6.4 Conclusions

In summary, the compressibilities of Sc_2BDC_3 and $Sc_2(NO_2\text{-}BDC)_3$ are highly sensitive to the pressure-transmitting medium used. In methanol, the medium is forced into the pores of Sc_2BDC_3, and can be located in two distinct sites. Upon increasing pressure, the occupancy of the least favourable binding site increases as more methanol molecules are forced into the pores until a maximum uptake is observed at

≈ 1.1 GPa. The uptake of methanol molecules here is unusual, in that no change in the framework takes place, and that the uptake of hydrophilic guest molecules into the hydrophobic pores of Sc_2BDC_3 is driven by guest-guest interactions. GCMC simulations showed that methanol adsorption is facilitated by an increase in methanol-methanol interactions with loading. At ambient pressure, site 1 shows the greatest occupancy with increasing methanol loading. Slight structural changes observed upon pressure increase result in a significant increase in guest-framework interactions and lead to greater adsorption at both sites 1 & 2.

Fluorinert is too large to penetrate the pore volume of Sc_2BDC_3 and so the framework compresses upon loading to 0.1 GPa. Increasing the pressure further to 0.4 GPa results in a crystalline-amorphous phase transition which is fully reversible. Contrary to this behaviour, the crystallinity of Sc_2BDC_3 is retained during methanol-mediated compression up to 3.0 GPa.

The apertures in $Sc_2(NO_2\text{-}BDC)_3$ are smaller than those in Sc_2BDC_3 due to the 50:50 disordered $–NO_2$ groups on the BDC ligands. This alters the way in which the unit cell volume changes in order to accommodate pressure application in methanol. In Sc_2BDC_3, the pressure-induced inclusion of methanol caused a swelling of the unit cell whereas here we see a decrease in unit cell volume for each increase in pressure. Unfortunately, the high-pressure data is not of high enough quality to extract pore content information, however we have inferred methanol uptake in $Sc_2(NO_2\text{-}BDC)_3$ due to the elongation of the ≈ 8 Å *a*-axis which is indicative of guest inclusion.

As with Sc_2BDC_3, Fluorinert is too large to penetrate the pore volume of $Sc_2(NO_2\text{-}BDC)_3$. Increasing pressure to 0.4 GPa yielded a direct compression of the

framework as seen from the decrease in all three axes and volume. The compression of the *a*-axis adds weight to our observation that the anisotropic behaviour of this axis can be a useful indicator for guest inclusion in these materials. Increasing pressure to 0.8 GPa results in a single-crystal to single-crystal phase transition from space group *C*2/*c* to *Fdd*2 with a concomitant collapse of the 1-D porous channels. Between 0.8 and 2.6 GPa, the framework showed continued compression with the compressibility decreasing with increasing pressure. Above 2.6 GPa, the sample underwent an irreversible amorphization.

These behaviors appear to be a consistent feature of MOFs put under extreme pressure, with the compressibility changing by several orders of magnitude depending on whether guest inclusion occurs (or whether any guest molecules are present), the nature of the guest species and how the pressure is applied. The role of guest molecules on the mechanical properties of porous materials is therefore an area ripe for exploration, with high-pressure crystallographic techniques proving incredibly useful for exploring the effect of increased guest inclusion on framework properties. Changing the chemical nature of the framework itself has also been shown to affect the compressibility with $Sc_2(NO_2\text{-}BDC)_3$ in FC-77 remaining crystalline to pressures far above that seen for the non-functionalized Sc_2BDC_3.

6.5 References

1 H.-C. Zhou, J. R. Long and O. M. Yaghi, *Chem. Rev.*, 2012, **112**, 673.

2 E. Coronado and G. Minguez Espallargas, *Chem. Soc. Rev.*, 2013, **42**, 1525; M. D. Allendorf, C. A. Bauer, R. K. Bhakta and R. J. T. Houk, *Chem. Soc. Rev.*, 2009, **38**, 1330.

3 G. Ferey and C. Serre, *Chem. Soc. Rev.*, 2009, **38**, 1380.

4 R. I. Walton, A. S. Munn, N. Guillou and F. Millange, *Chem. Eur. J.*, 2011, **17**, 7069.

5 G. Férey, C. Mellot-Draznieks, C. Serre, F. Millange, J. Dutour, S. Surblé and I. Margiolaki, *Science*, 2005, **309**, 2040.

6 S. A. Moggach, T. D. Bennett and A. K. Cheetham, *Angew. Chem., Int. Ed.*, 2009, **48**, 7087.

7 D. N. Dybtsev, H. Chun and K. Kim, *Angew. Chem., Int. Ed.*, 2004, **43**, 5033.

8 A. J. Graham, D. R. Allan, S. C. McKellar, M. I. H. Mohideen, R. E. Morris and S. A. Moggach, 2013, **submitted**.

9 J. P. S. Mowat, S. R. Miller, J. M. Griffin, V. R. Seymour, S. E. Ashbrook, S. P. Thompson, D. Fairen-Jimenez, A.-M. Banu, T. Düren and P. A. Wright, *Inorg. Chem.*, 2011, **50**, 10844.

10 S. R. Miller, P. A. Wright, T. Devic, C. Serre, G. r. Férey, P. L. Llewellyn, R. Denoyel, L. Gaberova and Y. Filinchuk, *Langmuir*, 2009, **25**, 3618.

11 S. A. Moggach, D. R. Allan, S. Parsons and J. E. Warren, *J. Appl. Crystallogr.*, 2008, **41**, 249.

12 G. J. Piermarini, S. Block, J. D. Barnett and R. A. Forman, *J. Appl. Physics*, 1975, **46**, 2774.

13 Bruker-Nonius, Bruker-AXS, Madison, Wisconsin, USA, 2006.

14 G. M. Sheldrick, *SADABS Version 2008-1*, 2008.

15 P. W. Betteridge, J. R. Carruthers, R. I. Cooper, K. Prout and D. J. Watkin, *J. Appl. Crystallogr.*, 2003, **36**, 1487.

16 A. L. Spek, Utrecht University, Utrecht, The Netherlands, 2004.

17 A. Dawson, D. R. Allan, S. Parsons and M. Ruf, *J. Appl. Crystallogr.*, 2004, **37**, 410.

18 S. Parsons, The University of Edinburgh, Edinburgh, United Kingdom, 2004.

19 A. Technologies, Agilent Technologies, 2011.

20 D. Frenkel and B. Smit, *Understanding Molecular Simulation: From Algorithms to Applications*, Academic Press, San Diego, 1996.

21 J. M. Haile, *Molecular Dynamics Simulation: Elementary Methods*, John Wiley & Sons, New York, 1992.

22 P. P. Ewald, *Annalen der Physik*, 1921, **369**, 253.

23 S. L. Mayo, B. D. Olafson and W. A. Goddard, *J. Phys. Chem.*, 1990, **94**, 8897.

24 A. K. Rappe, C. J. Casewit, K. S. Colwell, W. A. Goddard and W. M. Skiff, *J. Am. Chem. Soc.*, 1992, **114**, 10024.

25 B. Chen, J. J. Potoff and J. I. Siepmann, *J. Phys. Chem. B*, 2001, **105**, 3093.

26 D. Fairen-Jimenez, S. A. Moggach, M. T. Wharmby, P. A. Wright, S. Parsons and T. Düren, *J. Am. Chem. Soc.*, 2011, **133**, 8900.

27 A. Gupta, S. Chempath, M. J. Sanborn, L. A. Clark and R. Q. Snurr, *Mol. Simul.*, 2003, **29**, 29.

28 G. P. Johari and S. J. Jones, *Philos. Mag. B*, 1986, **54**, 311.

29 S. Wang, S. Hirai, M. C. Shapiro, S. C. Riggs, T. H. Geballe, W. L. Mao and I. R. Fisher, *Phys. Rev. B*, 2013, **87**.

30 Z. Sun, J. Zhou, Y. Pan, Z. Song, H.-K. Mao and R. Ahuja, *Proc. Natl. Acad. Sci. U. S. A.*, 2011, **108**, 10410.

31 T. D. Bennett, P. Simoncic, S. A. Moggach, F. Gozzo, P. Macchi, D. A. Keen, J.-C. Tan and A. K. Cheetham, *Chem. Commun.*, 2011, **47**, 7983.

32 Y. H. Hu and L. Zhang, *Phys. Rev. B: Condens. Matter Mater. Phys.*, 2010, **81**, 174103/1; K. W. Chapman, D. F. Sava, G. J. Halder, P. J. Chupas and T. M. Nenoff, *J. Am. Chem. Soc.*, 2011, **133**, 18583.

33 A. J. Graham, D. R. Allan, A. Muszkiewicz, C. A. Morrison and S. A. Moggach, *Angew. Chem., Int. Ed.*, 2011, **50**, 11138.

34 P. Serra-Crespo, E. Stavitski, F. Kapteijn and J. Gascon, *RSC Adv.*, 2012, **2**, 5051.

35 K. W. Chapman, G. J. Halder and P. J. Chupas, *J. Am. Chem. Soc.*, 2008, **130**, 10524.

Chapter 7

Conclusion

7.1 Conclusions

The aim of this project was to examine the effects that high pressures can have on the structure and compressive behaviour of a series of metal-organic framework materials. Previous work has sought to obtain/alter desirable MOF properties such as guest uptake and storage by chemical means. Here, physical manipulation through pressure application has shown large effects on guest inclusion/expulsion and clear trends have been discovered in how MOFs are able to accommodate pressure.

The effect of pressure on the prototypical MOF called MOF-5 was studied experimentally from ambient pressure to 3.2 GPa. Initial compression caused the hydrostatic medium to be 'squeezed' into the pores, in contrast to computational compression which resulted in direct compression of the framework. Further pressure increases yielded a period of guest evacuation and framework volume reduction until the single crystal sample began to degrade and eventually amorphized above 3.2 GPa. This pressure is orders of magnitude higher than was previously reported for direct compression of MOF-5 and shows that medium inclusion delays the onset of amorphisation. Within this compressive range, the bulk modulus of the material changed dramatically with values varying from 242.5 GPa (between 0.14 and 0.71 GPa applied pressure) to 22.3 GPa (between 1.89 and 2.57 GPa applied pressure). This highlights the dynamic nature of the guest-framework interactions and their ability to confer rigidity to the structure. The framework compression was seen to be in part driven by shortening of the Zn-O bonds that link the Zn_4O clusters with the terephthalate linkers.

In the MOF Cu-btc, the application of pressure caused solvent to be squeezed into the pores (like MOF-5) until a phase transition occurred above 3.9 GPa, driven by the sudden compression and expansion of equatorial and axial Cu–O bonds. This transition in compressibility is associated with a pore emptying region and the sudden shortening of the stiffer equatorial Cu-O bonds which are very resilient to any compression up to phase transition pressure.

The first ever high-pressure post-synthetic modification of a MOF has been observed. On application of pressure in methanol of 0.2 GPa to a Cu-based MOF called STAM-1, a ligand exchange reaction takes place resulting in a change in pore size, shape, and hydrophilicity of the resulting pores. This new structure, STAM-

1_{MeOH}, is more resilient to compression and remains crystalline to higher pressure than native STAM-1. We also demonstrated the ability to force hydrophilic isopropyl alcohol molecules into hydrophobic pores using pressure, counteracting the hydrophobic effect.

A high-pressure combined experimental and computational study has been carried out on a type of MOF known as a zeolitic imidazolate frameworks (or ZIF) that adopt the sodalite topology. ZIF-8 has been shown previously to undergo a phase transition between 0.9 and 1.47 GPa, which involves the rotation of methylimidazolate groups which allowed for greater uptake of guest molecules. In pentane:isopentane, inherent framework flexibility was observed for ZIF-8, though no phase transition was observed. This implies that the nature of the penetrating medium has a part to play in driving the phase transition. These results are rationalized with a complementary computational analysis and potential energy screening of conformational flexibility. Unit cell reduction is mediated in part through the rotation of the imidazolate rings and in part by reductions in the length of Zn-N coordination bonds.

Finally, the application of pressure to the MOF Sc_2BDC_3 and the nitro functionalized derivative $Sc_2(NO_2\text{-}BDC)_3$ was also studied. Despite sharing a framework topology, the effect of chemical modification is marked. Compression in methanol caused an initial swelling of the Sc_2BDC_3 framework; as the porous, relatively expansive, network was able accommodate guest molecules. The monofunctionalization caused a reduction in guest accessible space and therefore a reduced capacity for medium uptake. This resulted in direct compression of $Sc_2(NO_2\text{-}BDC)_3$.

Fluorinert, too large to penetrate either framework, caused a single crystal to amorphous phase transition for Sc_2BDC_3 between 0.1 and 0.4 GPa. Raman spectroscopy revealed that the local structure of the framework was retained during this amorphization and the transition was found to be reversible upon return of the sample to ambient pressure. During compression of $Sc_2(NO_2\text{-}BDC)_3$ in the same medium, a reduction in unit cell volume was observed to 0.4 GPa. Increasing pressure to 0.8 GPa resulted in a single-crystal to single-crystal phase transition from space group *C*2/*c* to *Fdd*2 with an associated collapse of the 1-D porous network.

Continued increase in pressure yielded further volume decrease with the compressibility decreasing with increasing pressure. Above 2.6 GPa, the sample underwent an irreversible amorphisation.

The work in this Thesis is the first example of a physical probing of MOFs by high-pressure single crystal X-ray diffraction. As a result, we are able to explain some of the phenomena that we observe at atomic resolution, though due to the limitations of the technique with respect to such large framework materials it is difficult to deconvolute different physical phenomena, namely the effect of thermal motion and low energy phonons, which contribute to unit cell distortions. However, we believe that rationalizing the unit cell volume with respect to guest inclusion and coordination bonding environments is able to, at least in part, explain the behaviour observed. The investigation of coordination bonding environment would be greatly facilitated by the development of low-temperature high-pressure apparatus for single crystal X-ray diffraction experiments and indeed this is being created and evolved at the University of Edinburgh in the group of Prof Simon Parsons.

The general trends of high-pressure behaviour in inorganic compounds as outlined in this Thesis (Chapter 1) have been observed when high pressure has been applied to metal-organic frameworks. Pressure induced ‘super-filling’ of the pores at GPa pressures, medium dependent compression and pressure-induced amorphisation have all been observed and we have rationalized these effects based on the physical (Flourinert driven amorphisation) and chemical (STAM-1 hydrophobic/hydrophilic) nature of the guest molecules as well as the pore structures themselves.

A continuation of this work would be to systematically combine MOFs and hydrostatic media in order to explore the geometrical distortions arising from their unique topologies and chemical attributes. Work has continued in the group of Dr Stephen Moggach on ligand exchange within STAM-1 and understanding the distortions within substituted Sc_2BDC_3.